

Corrosion Behavior of Direct Metal Laser Sintered Ti-6Al-4V for Orthopedic Applications

by
Yangzi Xu

A Dissertation

Submitted to the Faculty

of the

WORCESTER POLYTECHNIC INSTITUTE

in partial fulfillment of the requirements for the

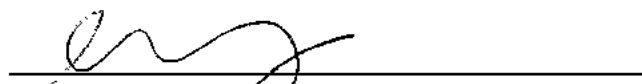
Degree of Doctor of Philosophy

in

Materials Science and Engineering

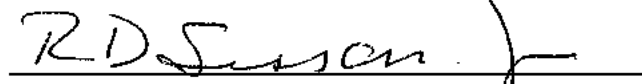
May 2017

APPROVED:



Professor Jianyu Liang, Advisor

Associate Professor in Mechanical Engineering



Professor Richard D. Sisson, Jr., Advisor

George F. Fuller Professor

Director of Manufacturing and Materials Engineering

ABSTRACT

Ti-6Al-4V alloy has been used as biomedical implants for decades because of its superior mechanical properties, good biocompatibility, lack of allergic problems and good corrosion resistance. It is widely used as the tibial components in total knee arthroplasty and hip cup in total hip replacement. However, the mechanical properties of Ti-6Al-4V implant can be deteriorated due to corrosion pits. In the past decades, the rapid developments in additive manufacturing have broadened their applications in biomedical area due to the high geometrical freedom in fabricating patient-friendly implants. However, the high-localized thermal input and fast cooling rate during laser processing usually result in non-equilibrium phase with high residual stress. Therefore, it is necessary to apply proper post-treatments on the as-printed parts to ensure better properties. In this work, various post-treatments (e.g. post-heat treatments, hot isostatic pressing) were applied aim to improve the corrosion behavior of direct metal laser sintered Ti-6Al-4V parts. The effect of post-treatment temperature on the mechanical properties and corrosion behavior were examined experimentally. A discussion on factors influencing corrosion rate was presented, and the corrosion mechanism on the Ti-6Al-4V part in simulated body fluid was proposed. Based on the electrochemical measurement results, enhanced corrosion resistance was observed in the samples after high temperature post-heat treatments and hot isostatic pressing in the $\alpha+\beta$ region of 799°C.

EXECUTIVE SUMMARY

This study was aimed to evaluate the effect of various post-treatments on the corrosion behavior of Ti-6Al-4V parts via direct metal laser sintering, and propose a desirable post-treatment procedure that can obtain a good combination of mechanical properties and corrosion behavior of as-printed parts in the simulated body environment.

Direct metal laser sintering (DMLS) technique was used to fabricate Ti-6Al-4V dumbbell-shaped tensile testing bars, and the dimension was determined based on ASTM standard. The as-printed parts were examined and compared to the commercial Grade 5 alloy in terms of microstructure, phase fraction, porosity and residual stress. It was found out that the as-printed samples mainly composed of acicular α' martensite phase with small amount of nano-scaled β precipitates dispersed in the α' matrix due to fast cooling during laser processing, whereas, the Grade 5 alloy has $\alpha + \beta$ two phase with equiaxed microstructure. The β phase fraction in the as-printed and Grade 5 alloy is 1.6% and 20%, respectively, based on X-ray diffraction refinement results. Furthermore, the laser processing can introduce defects due to lack of fusion or entrapped gas, and leads to porosity, which is absent in the Grade 5 alloy. The fast cooling rate also caused residual tensile stress in the as-printed parts.

Since the as-printed samples have several differences from the Grade 5 alloys, the effects of these factors on the corrosion behavior of DMLS samples were studied. It was found out that the surface roughness value has an exponential effect on the corrosion current density and calculated corrosion rate. A rough surface will lead to higher corrosion rate, and smooth surface can decrease the corrosion rate, but rougher surface will also enhance osteointegration. Therefore, the surface roughness value needs to be adjusted based on specific applications.

The effect of porosity was analyzed using crevice corrosion test: a clean glass slide was attached to the as-polished sample surface and fixed using rubber band, the whole device was immersed in Ringer's solution for long time and maintained at body temperature. After one month immersion, pits were found on the metal surface near the originally existed pores, which is due to the formation of localized O_2 concentration cell near the pore. Therefore, porosity in the as-printed parts can impair the crevice corrosion resistance. In order to reduce porosity, hot isostatic pressing (HIPing) was applied at three different temperatures in the $\alpha + \beta$ region. Based on electrochemical measurement results (polarization test and electrochemical impedance spectroscopy), different degree of improvement in corrosion resistance was observed after

HIPing. A reduction in porosity and corrosion current density can be observed in the HIPed samples, and this is more significant after high temperature HIPing at 799°C.

It was reported by several researches that post-heat treatments could improve mechanical properties, especially increase ductility and fatigue strength. However, the corrosion behavior change during various post-heat treatments has not been fully understood. In this work, three different types of post-heat treatments were applied on the as-printed samples: 1) annealing treatment, 2) solution treatment and aging, and 3) stress relieve treatment. Transformation from α' to α phase, coarsening of the α lath microstructure and developing of β phase can be observed after post-heat treatments, and highest fraction of β phase was observed in the high temperature annealed sample. Enhanced corrosion resistance was found in the annealed, solution treatment and aged and high temperature stress relieved samples. The reasons for improved corrosion resistance after heat treatments are: 1) the passive film developed on the surface has higher resistance; 2) increased β phase fraction and size can reduce the susceptible sites to corrosion of the parts. Furthermore, the as-printed sample only possesses single passive layer, and a double passive layer can be observed after heat-treated at temperature higher than 550°C, though second layer (mainly comprised of Al_2O_3 and V_2O_5) has very low resistance compared to the existed layer (mainly TiO_2).

In sum, it was found that high temperature annealing treatment in the $\alpha+\beta$ region could enhance the corrosion resistance of DMLS Ti-6Al-4V parts. Therefore, HIPing under the annealing temperature (799°C) is a recommended post-treatment for as-printed Ti-6Al-4V to achieve an enhanced corrosion resistance.

ACKNOWLEDGEMENTS

I want to deeply acknowledge my advisor, Professor Richard D. Sisson Jr., for providing me the opportunity to work on this project and his constant guidance and encouragement during my PhD study.

I also want to express my sincere gratitude to Professor Jianyu Liang, Professor Satya Shivkumar, Professor Yan Wang, Professor Brajendra Mishra, Dr. Danielle L. Cote and Meghan Pasquali for their help, encouragement and serving in my thesis committee. Without all their help, I cannot image where I am now.

I would like to give special gratitude to Professor Christopher A. Brown for his patient guidance and letting me use the facilities in the Surface Metrology Laboratory.

I want to thank Dr. Sakthikumar Ambady in the Department of Biomedical Engineering for his assistance in the in vitro tests.

I am grateful to Dr. Boquan Li for his constant assistance on experimental operations and troubleshooting. The generous and elaborate help from Rita Shilansky is greatly acknowledged.

It is a pleasure to thank Quintus Technology, LLC for the help in conducting hot isostatic pressing.

Meanwhile, I want to thank all my friends and colleagues, as well as all the staff and faculty in the Materials Science and Engineering Department and Metal Processing Institute for their help for my life and my PhD work.

Finally, I would like to thank my family members, my parents and my husband Chen Chen for their constant great support and encouragement. Without their care and understanding, I cannot imagine where I am now.

TABLE OF CONTENTS

ABSTRACT.....	1
EXECUTIVE SUMMARY	2
ACKNOWLEDGEMENTS.....	4
CHAPTER 1: INTRODUCTION.....	6
CHAPTER 2: LITERATURE REVIEW	9
CHAPTER 3: PAPER I: INVESTIGATIONS ON FACTORS INFLUENCE THE CORROSION BEHAVIOR OF DIRECT METAL LASER SINTERED Ti-6Al-4V	31
CHAPTER 4: PAPER II: EFFECT OF ANNEALING TREATMENTS ON THE MICROSTRUCTURE, MECHANICAL PROPERTIES AND CORROSION BEHAVIOR OF DIRECT METAL LASER SINTERED Ti-6Al-4V	48
CHAPTER 5: PAPER III: EFFECT OF POST-HEAT TREATMENT PROCESSING ON THE MICROSTRUCTURE AND CORROSION BEHAVIOR OF DIRECT METAL LASER SINTERED Ti-6Al-4V	49
CHAPTER 6: PAPER IV: EFFECTS OF HOT ISOSTATIC PRESSING ON THE MICROSTRUCTURE, MECHANICAL PROPERTIES AND CORROSION BEHAVIOR OF Ti-6Al-4V VIA DIRECT METAL LASER SINTERING	66
CHAPTER 7: RESEARCH CONCLUSIONS	82
CHAPTER 8: RECOMMENDATIONS FOR FUTURE WORK.....	84
CHAPTER 9: PUBLICATIONS, POSTERS AND PRESENTATIONS	85

CHAPTER 1

INTRODUCTION

1.1 Project Needs

The orthopedic industry is growing rapidly [1]. It was reported that 1.2 million hip and knee implant procedures are carried out worldwide every year, based on the research of global orthopedics device industry 2012-2017 [1][2]:

“The global orthopedics device industry reached an estimated \$36.7 billion in 2011 during 2006-2011 is expected to reach an estimated \$46.3 billion by 2017 with a CAGR of 3.9 percent over the next five years.”

It was also reported that apart from the aging of population, trauma and other reasons, more than 20% of the hip replacement surgeries are revision surgeries every year. Revision total hip replacement surgeries are recognized as being both more expensive and associated with greater technical difficulties than primary surgeries[3]. The number and cost of primary and revision total hip arthroplasty in the USA for 2003 and projected number for 2030 are shown in Figure 1(a) and (b), respectively [3].

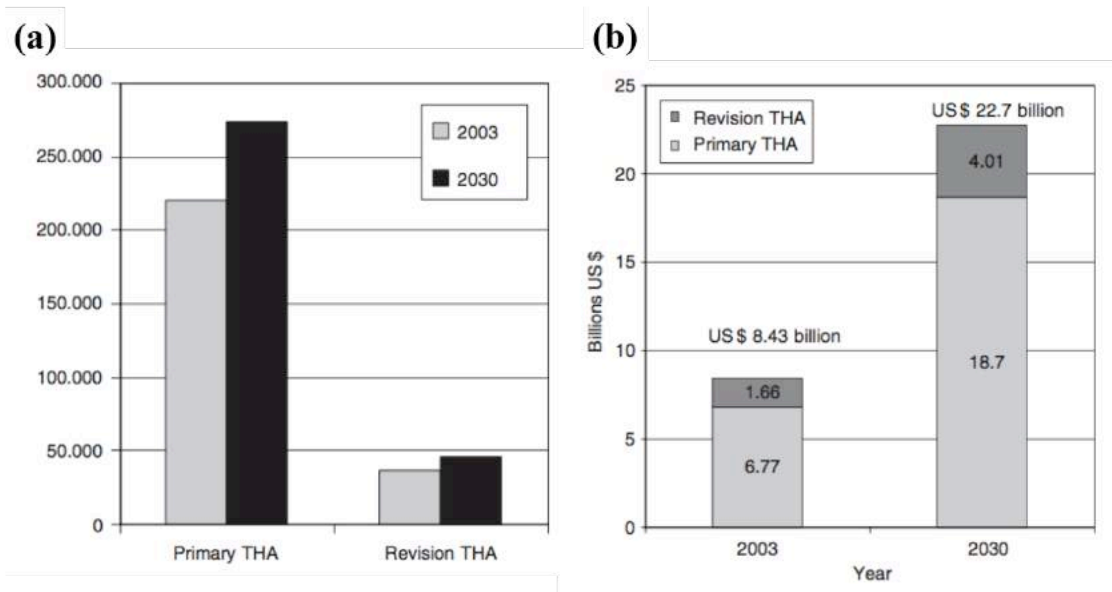


Figure 1: The number (a) and cost (b) of primary and revision total hip arthroplasty in the USA for 2003 and projected values for 2030 [3].

The top reason for failure of hip replacement is aseptic loosening, which is the most common

reason for revisions after lower-extremity total joint arthroplasties [4]. In the total hip replacement, metallic wear particles were detected in the surrounding tissues of the failed parts due to fretting corrosion. The mechanical properties of the acetabula cup (made of Ti-6Al-4V) deteriorated due to the corroded surface covered with pits and caused failure [5]. Therefore, requirement for acetabula cup with enhanced corrosion behavior and highly customization is needed.

Additive manufacturing techniques can fabricate highly customized hip replacement directly from computer-aided design mode to avoid mismatch, and reduce some amount of corrosion of metal parts inside human body. However, the as-fabricated Ti-6Al-4V parts usually have non-equilibrium phase with poor mechanical and corrosion properties. Therefore, various post-treatments need to be applied to the as-fabricated Ti-6Al-4V before further clinical applications.

1.2 Project Goals

The goal of this work is to evaluate the effect of various post-treatments on the mechanical properties and corrosion behavior of as-printed Ti-6Al-4V parts via direct metal laser sintering, and propose a desirable post-treatment procedure that can enhance the corrosion behavior of as-fabricated Ti-6Al-4V in simulated body environment.

Due to the fast cooling rate during direct metal laser sintering, two major problems can be observed in the as-printed Ti-6Al-4V: 1) the formation of non-equilibrium acicular martensite phase (α') and high residual stress which may lead to low ductility, 2) higher porosity (lower density) than the conventional forged samples due to lack of fusion and entrapped gas. Therefore, we are trying to apply various post-heat treatments (solution treatment and aging, annealing treatment and stress relieving treatments) to the as-printed Ti-6Al-4V to achieve the occurrence of transformation phenomenon $\alpha' \rightarrow \alpha + \beta$. Furthermore, the effect of hot isostatic pressing, which can reduce porosity, under various temperatures on the sample performance were also studied. The microstructure and phase development under different heat treatments and hot isostatic pressing were examined and compared to the wrought commercial Ti-6Al-4V specimen. The corresponding corrosion behavior of the parts were studied in simulated body fluid electrochemically, and a recommended post-treatment procedure was proposed for direct metal laser sintered Ti-6Al-4V for orthopedic application.

Reference

- [1] Gordon, Leslie. "Electron-beam melting builds titanium parts." *Machine Design* 22 Mar. 2012: 36. *Science in Context*. Web. 1 May 2016.
- [2] "Research and Markets Adds Report: Global Orthopedics Device Industry 2012-2017: Trends, Profits and Forecast Analysis." *Manufacturing Close-Up* 28 Mar. 2014. *Business Insights: Essentials*. Web. 1 May 2016.
- [3] Barrack, R. L. (1995). Economics of revision total hip arthroplasty. *Clinical orthopaedics and related research*, 319, 209-214.
- [4] Cherian, J. J., Jauregui, J. J., Banerjee, S., Pierce, T., & Mont, M. A. (2015). What Host Factors Affect Aseptic Loosening After THA and TKA?. *Clinical Orthopaedics and Related Research*®, 473(8), 2700-2709.
- [5] Khan, M. A., R. L. Williams, and D. F. Williams. "The corrosion behaviour of Ti-6Al-4V, Ti-6Al-7Nb and Ti-13Nb-13Zr in protein solutions." *Biomaterials*, 20(7) (1999), 631-637.

CHAPTER 2

LITERATURE REVIEW

2.1 Additive Manufacturing

Additive manufacturing (AM) is a technology for fabricating near-net shape parts directly from three-dimensional computer-aided design (CAD) model. In contrast with the traditional subtractive techniques (e.g. machining and milling), the parts are fabricated by an electron or laser beam layer by layer based on the pre-designed CAD model. AM has several significant benefits against traditional manufacturing techniques, such as time efficiency, highly geometric freedom and complexities, and less waste production [1].

Direct metal laser sintering (DMLS) is the trade name of EOS GmbH to indicate the selective laser melting process, which is schematically shown in Figure 2. A focused laser beam fuses the thin layer of powder materials based on the pre-designed model (Figure 2b and 2c). The platform is then lowered and another thin layer of powder is applied (Figure 2d). Once again the material is sintered so as to bond with the previous layer, and results in the final complex part [2].

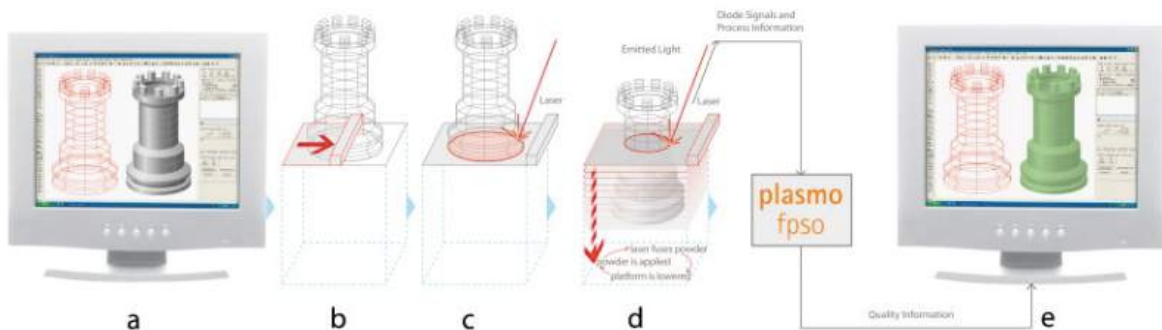


Figure 2: Description of the direct metal laser sintering technique [3].

The quality of the as-fabricated part can be affected by the powder material, exposure temperature, inert gas flow, temperature at the building platform and scanning strategy. Internal porosity, defects and lack of fusion can be caused by poor scanning design [2]. Considerable effort has been put into optimization of the processing variables in DMLS to achieve desirable properties of the final parts. During the high-temperature consolidation process of sintering, loosely mechanical connected powder particles are transformed into metallic bonds of greater strength [4]. Internal porosity and defects are unavoidable during this process. The internal

porosity will deteriorate the fatigue and tensile properties of AM parts. The short interaction time and highly localized thermal input will lead to development of non-equilibrium phase and high residual stress in the as-fabricated parts. Therefore, post-heat treatments are required to reduce the residual stress, and hot isostatic pressing is also widely used in the as-fabricated AM parts to achieve denser parts with lower porosity. More information on the post-treatments is discussed in Section 2.3.4.

This work is focusing on the effects of post-processing on the corrosion behavior of DMLS Ti-6Al-4V parts for orthopedic applications, especially acetabula cup in the hip replacement. The heat treatments of Ti-6Al-4V have been investigated extensively. The starting microstructure is always the mill-annealed parts with equiaxed α grains. However, as is shown in the previous studies, the microstructure of the as-fabricated DMLS Ti-6Al-4V consists of acicular martensite α' phase with high yield stress (about 1GPa), high ultimate tensile strength but a low ductility (less than 10%) [5]. In this work, the different response of DMLS Ti-6Al-4V parts on generally applied titanium heat treatment and hot isostatic pressing is studied. The influence of heat treatment temperature and cooling rate is distinguished.

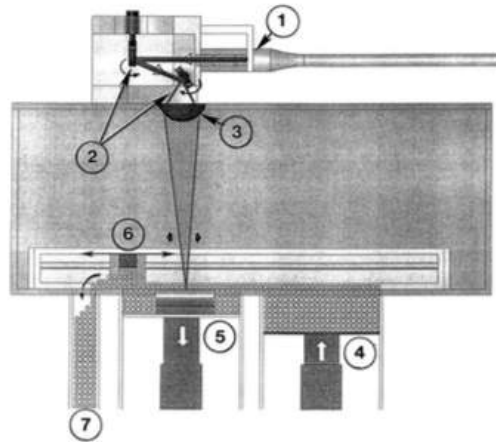


Figure 3: SLM system showing key components. The following numbers correspond to those circled in the figure: (1) laser; (2) Double rotating mirror system; (3) Beam focus lens. The beam is scanned over the layer-building parts; (4) Powder feeder system; (5) Building platform; (6) Recoater and (7) Powder recovery/recycle [8].

2.1.1 Selective Laser Melting and Direct Metal Laser Sintering

Figure 3 illustrates a schematic view of the EOSINT M270 selective laser melting (SLM) or DMLS (the trade name from EOS GmbH to indicate SLM process) [8]. The principle of SLM and DMLS was discussed in Section 1.3.

2.1.2 Electron Beam Melting

Figure 4 illustrates a schematic view of the ARCAM EBM S400 system. This electron beam melting system (EBM) builds parts by scanning from the bottom up with the focused electron beam at nominally 10^3 mm/s to selectively melt specific area based on the CAD model in a vacuum. The powder rake (circle 5 in Figure 4) moves between the two cassettes (circle 4 in Figure 4) to evenly distribute the powder layers over the surface after each building layer is completed [8].

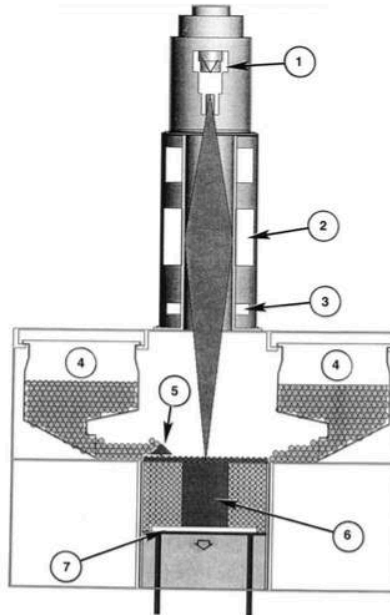


Figure 4: EBM system schematic showing key components: (1) Electron gun assembly; (2) Electron beam focusing lens; (3) Electron beam deflection coils (x-y); (4) Powder cassettes; (5) Powder layer rake; (6) Cylindrical build test specimen; (7) Build layer [8].

The electron gun operates nominally at 60kV to develop an energy density of 10^2 kW/cm² in the focused electron beam [8]. The variations of beam current, scan rate and heating history will influence the microstructure and mechanical properties of the as-fabricated parts.

2.1.3 Comparison between SLM (DMLS) and EBM

The parameters differences between SLM (DMLS) and EBM techniques are summarized in Table 1. The chamber environment of SLM (DMLS) is inert gas flow (Argon or Nitrogen), so the as-sintered parts undergo gas cooling, whereas, the working environment of EBM system is in a vacuum. The difference in cooling rate will influence the microstructure and mechanical properties of the as-fabricated parts. As reported by previous researchers [8], the EBM-built Ti-6Al-4V has acicular α phase with β along the phase boundaries and the SLM-built Ti-6Al-4V possesses acicular α' martensite phase. The EBM process involves more significant melt than the SLM process which including thermal gradients and effective product quenching. The transmission electron microscopy (TEM) bright-field images of EBM-built Ti-6Al-4V indicates acicular α lath, and the SLM-built part consists of acicular α' and α'' lath [8].

Table 1: Comparison between SLM (DMLS) and EBM techniques.

Parameters	SLM (DMLS)	EBM
Energy source	Focused CO ₂ laser beam	Focused electron beam
Chamber environment	Argon/N ₂ gas flow	Vacuum
Energy density	In the order of 10 ² kW/cm ²	In the order of 10 ² kW/cm ²
Layer thickness	Approximate 30 μ m	Approximate 100 μ m
Scanning speed	In the order of 7 \times 10 ³ mm/s	In the order of 10 ³ mm/s

Due to the microstructural difference, SLM-built Ti6Al4V has a Vickers microindentation hardness value of approximately 24% greater than that for the EBM product [8]. The difference in mechanical properties is shown in Figure 5. SLM-built part has a UTS increase of 23% and a corresponding drop of elongation by 78% [8]. Therefore, EBM and SLM can potentially fabricate multiporous products as well as multimicrostructural products (α , β , $\alpha + \beta$, α') to eliminate the “stress-shielding effects”, and the mechanical properties can also be tailored.

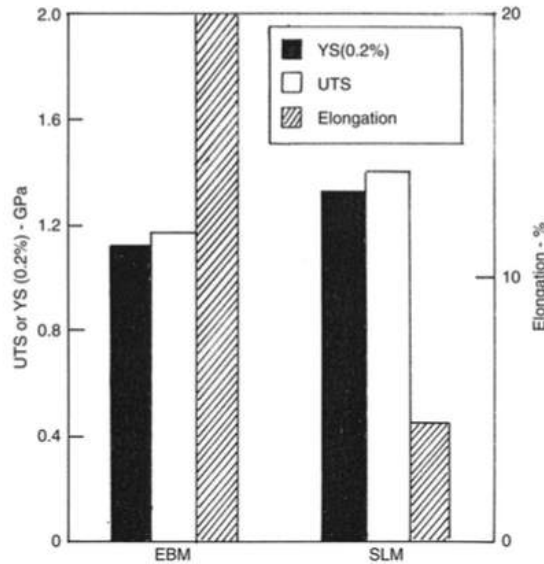


Figure 5: Ultimate tensile strength (UTS), 0.2% offset yield stress (YS) and elongation (%) for EBM vertical cylinder build compared with SLM horizontal cylinder build [8].

2.1.4 Potential Impacts and Post-treatments

Although AM techniques have several advantages and promising applications, some issues may delay their further applications.

- (1) The mechanical property of the pre-alloyed powder particles is very essential in the final parts. A significant feature of both SLM and EBM layer manufacture is the reduction of waste of the unused powder materials since they can be recycled. However, powder recycling may lead to contamination and oxidation issues that will affect the properties of the built part in some extent [8].
- (2) The as-built parts from SLM and EBM possess rough surface, but a highly polished surface is required in some applications (e.g. medical implants). So, there is of course the necessity for precision surface finish on as-built sample for those specific applications.
- (3) The as-built parts (from both SLM and EBM) may have porosity and defects due to improper sintering parameters. The pores and defects can act as crack initiation sites and may cause catastrophic failure in future applications. Therefore, it is necessary to execute proper post-treatments on additively manufactured parts to completely eliminate any residual porosity and ensure better properties.

Hot isostatic pressing (HIP) is a relatively new production process, and the first lab equipment

was developed in the United States and Sweden at the middle of last century [10]. HIPing of powder metallurgy and cast components is often recommended as a means to eliminate any porosity that may initiate premature failure [9]. Figure 6 schematically shows the working chamber of hot isostatic pressing. After sample is loaded into the chamber, air is pumped out of it. Then the system that deliver and argon are connected, and high pressure is created inside the chamber by a compressor. After the certain prescribed values of temperature and pressure are achieved, they are maintained for a certain holding period before unloading [10]. During HIP, the high gas pressure in the press acts uniformly in all the directions, which can ensure that the pressed products have isotropic properties and a density of 100% [10].

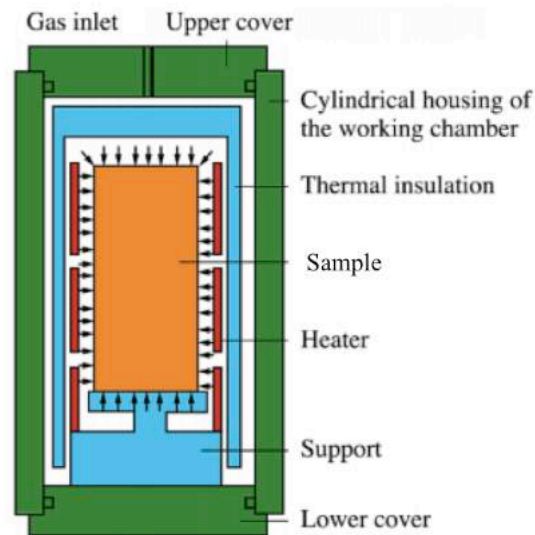


Figure 6: Working chamber of hot isostatic pressing [10].

Based on previous studies [11-13], HIP can slightly coarsen the as-built Ti6Al4V microstructure in SLM and EBM, and increase the density by eliminating internal pores. Due to the improvement in microstructure, the ultimate tensile strength and Young's modulus decrease and elongation increases after HIP. Fatigue strength is more significantly improved.

On the other hand, heat treatments of Ti6Al4V have been studied extensively. Post-heat treatments of as-built Ti6Al4V parts can be used to achieve a variety of desired mechanical properties for particular applications and reduce the thermal stresses that have been built during fabrication [5]. Some researchers were focused on conducting solution treatment and aging (STA) and annealing treatment on the as-built Ti6Al4V parts [5][14]. Improvements on the

equilibrium phase percentage and mechanical properties were reported.

2.2 Titanium alloys for Biomedical Applications

2.2.1 Titanium alloys for Total Joint Replacement

Nature synovial joints (knee, hip or shoulder joints) are composed of articular cartilage, a load-bearing connective tissue covering the bone, synovial fluid and a nutrient fluid [15]. The human joints are prone to degenerative and inflammatory diseases that lead to pain and joint stiffness. It was reported that 90% of the population over the age of 40 suffers from some degree of degenerative of joints [16]. In order to solve this problem, total joint replacement (TJR) arthroplasty was developed and great progress has been achieved over 190 years of orthopedic surgery history [15]. Total hip replacements (THR) and total knee replacements (TKR) have been the principle focus of artificial joint studies.

Compatibility	Mechanical Properties	Manufacturing
<ul style="list-style-type: none"> • Tissue reactions • Change in properties <ul style="list-style-type: none"> ○ Mechanical ○ Physical ○ Chemical • Degradation leads to <ul style="list-style-type: none"> ○ Local deleterious changes ○ Harmful systemic effects 	<ul style="list-style-type: none"> • Elasticity • Yield stress • Ductility • Toughness • Time dependent deformation • Creep • Ultimate strength • Fatigue strength • Hardness • Wear resistance 	<ul style="list-style-type: none"> • Fabrication methods • Consistency and conformity to all requirements • Quality of raw materials • Superior techniques to obtain excellent surface finish or texture • Capability of materials to get safe and efficient sterilization • Cost of products

Figure 7: Implant materials requirements in orthopedic applications [15].

Requirements for implant materials in orthopedic applications are listed in Figure 7. The ‘ideal’ material for TJR should exhibit the following properties [15]:

“A ‘biocompatible’ chemical composition to avoid adverse tissue reactions, an excellent resistance to degradation (corrosion) in the human body environment, acceptable strength to sustain the cyclic loading endured by the joint, a low modulus to minimize bone resorption, and a high-wear resistance to minimize debris generation.”

Stainless steel and Cobalt-alloys were first being considered for TJR because of their high wear and corrosion resistance. However, their high elastic modulus (200-230 GPa) with respect to natural bone (10-40 GPa) will lead to significant stress-shielding and bone apoptosis [15]. The

preferred alternative alloys for TJR are titanium and its alloys, especially Ti6Al4V ELI (extra-low interstitial), due to their low elastic modulus, good corrosion resistance and biocompatibility. Since 1980s, new titanium alloy compositions have been developed in response to concerns relating V to potential cytotoxicity and relative high elastic modulus of Ti6Al4V ELI [15]. The first generation titanium orthopedic alloys include Ti-6Al-7Nb and Ti-5Al-2.5Fe that have similar properties to Ti6Al4V to avoid the potential cytotoxicity of vanadium. Further, biocompatibility enhancement and lower elastic modulus can be achieved through the development of second generation titanium orthopedic alloys including Ti-12Mo-6Zr-2Fe ‘TMZF’, Ti-15Mo-5Zr-3Al, Ti-15Mo-3Nb-3O, Ti-15Zr-4Nb-2Ta-0.2Pd and Ti-15Sn-4Nb-2Ta-0.2Pd alloys as well as the ‘completely biocompatible’ Ti-13Nb-13Zr alloy. The third generation of titanium alloys achieved the minimum elastic modulus in Ti-Nb-Ta-Zr based alloys or ‘TNZT’. The advantages, disadvantages and primary utilizations of some orthopedic alloys are summarized in Table 3.

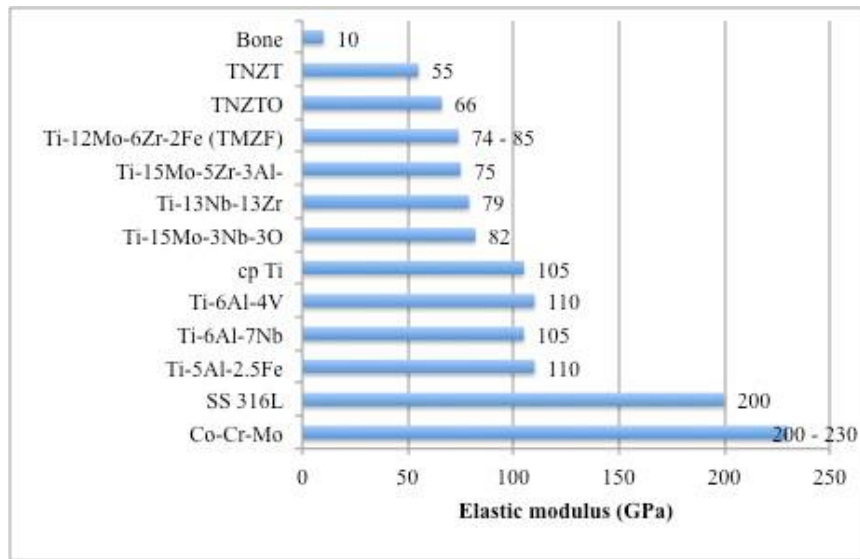


Figure 8: Elastic modulus values of orthopedic alloys compare to bone [15].

Among various titanium alloying elements, it is believed that V, Ni and Co are toxic elements, whereas Ti, Stainless steel, CoCrMo alloys, Ta, Zr, Nb and Pt composed the class of ‘resistant metallic biomaterials’ [15]. The comparison of elastic modulus values of orthopedic alloys to natural bone is shown in Figure 8 [15]. The minimum elastic modulus can be achieved in the synthesized Ti-Nb-Zr-Ta ‘TNZT’ alloys which also reduce potential adverse tissue reaction

through the utilization of biocompatible Nb, Ta and Zr.

Nonetheless, Ti-6Al-4V is still the current ‘standard material’ for TJR. Enhanced biocompatibility and reduced elastic modulus in titanium alloys have been achieved by the development of new near- β titanium alloys (metastable β or martensite $\alpha'+\beta$). Thoroughly study is need on the wear resistance and wears mechanism of those new titanium alloys before they can finally be applied clinically in TJR.

2.2.2 Titanium alloys for Dental Application

Dental implants are usually made from commercially pure titanium or titanium alloys. Commercially pure titanium (cp-Ti) has various degrees of purity (graded from 1 to 4) [17]. Most dental implants are made from grade 4 cp-Ti as it has higher strength than the other grades. Titanium alloys have greater yield strength and fatigue strength than cp-Ti, and they are also used in dental applications. An excellent biocompatibility is also required. A photograph of cp-Ti implant is shown is Figure 9.

Cp-Ti and Ti-6Al-4V are the main materials in the dental field as well as in the surgical field. Recently, Ti-40Zr, Ti-5Al-13Ta and Ti-43.1 at. %Zr-10.2 at. %Al-3.6 at. %V have been proposed [18]. In terms of the processing of dental implants, the casting process is dominant in achieving high strength and elongation. In dental precision casting, alumina based and magnesia based mold are mainly used, and the later one was reported to be more suitable for dental implant casting [18].

Table 2: Titanium alloys for dental applications and their mechanical properties [18].

Alloy	Process	Tensile strength (MPa)	Yield strength (MPa)	Elongation (%)	Vickers hardness
Ti-20Cr-0.2Si	Casting	874	669	6	318
Ti-25Pd-5Cr	Casting	880	659	5	261
Ti-13Cu-4.5Ni	Casting	703	-	2.1	-
Ti-6Al-4V	Casting	976	847	5.1	-
Ti-6Al-4V	Super plastic forming	954	729	10	346
Ti-6Al-7Nb	Casting	933	817	7.1	-
Ti-Ni	Casting	470	-	8	190

Table 3: Some characteristics of orthopedic metallic implant materials (adapted from [15]).

Orthopedic alloys	Alloy designations	Advantages	Disadvantages	Primary utilizations
Stainless steel	SS316 L	<ul style="list-style-type: none"> • Cost, availability • Processing 	<ul style="list-style-type: none"> • High modulus • Long term behavior 	Temporary devices (fracture plates, screws, hip nails)
Co-alloys	Co-Cr-Mo	<ul style="list-style-type: none"> • Wear resistance • Corrosion resistance • Fatigue strength 	<ul style="list-style-type: none"> • High modulus • Poor biocompatibility 	Dentistry castings; Prostheses stems; Load-bearing components in TJR
Titanium and its alloys	cp Ti; Ti-6Al-4V ELI	<ul style="list-style-type: none"> • Corrosion resistance • Low elastic modulus • Biocompatibility • Fatigue strength 	<ul style="list-style-type: none"> • Poor wear resistance • Low shear strength 	Used in THRs with modular (CoCrMo or ceramic) femoral heads; Long-term permanent devices (nails, pacemakers)
1 st generation Ti alloys	Ti-6Al-7Nb; Ti-5Al-2.5Fe	<ul style="list-style-type: none"> • Non-toxicity (vanadium free) 	<ul style="list-style-type: none"> • Poor biocompatible 	Designed to be used in THRs with modular (CoCrMo or ceramic) femoral heads
2 nd generation Ti alloys	Ti-12Mo-6Zr-2Fe (TMZF); Ti-15Mo-5Zr-3Al; Ti-15Mo-3Nb-3O; Ti-15Zr-4Nb-2Ta-0.2Pd; Ti-15Sn-4Nb-2Ta-0.2Pd; Ti-13Nb-13Zr	<ul style="list-style-type: none"> • Lower elastic modulus than Ti6Al4V • More biocompatible 	Still under clinical tests	Designed to be used in THRs with modular (CoCrMo or ceramic) femoral heads
3 rd generation Ti alloys	Ti-Nb-Ta-Zr (TNZT)	<ul style="list-style-type: none"> • Minimum elastic modulus 	Still under clinical tests	Designed to be used in THRs with modular (CoCrMo or ceramic) femoral heads

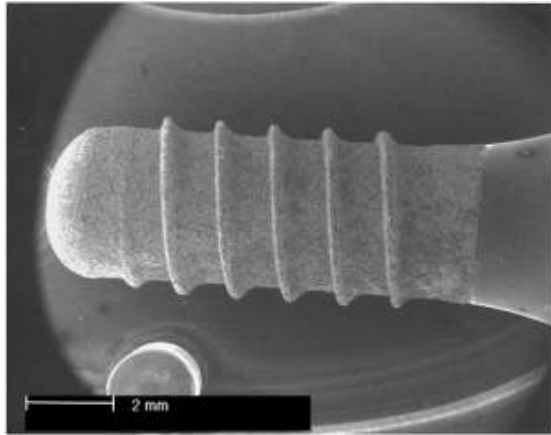


Figure 9: Photography of a cp-Ti implant [19].

2.3 Corrosion of Titanium Alloys for Orthopedic Applications

2.3.1 Corrosion Behavior Overview of Titanium Alloys

Titanium and its alloys are found to offer superior corrosion resistance in several media. The corrosion resistance of titanium alloys is found to vary with the alloy composition, environment and microstructure [19]. Dull et al.'s study indicated that the corrosion current density in Ti-6Al-4V alloy increases with the α to β ratio due to the formation of a galvanic cell between the two phases. The galvanic cell can be formed between the two phases because α phase contains more Al (α -stabilizer) and β phase is enriched of V (β -stabilizer). Also, it was reported that the Widmanstatten structure obtained on β solution treatment is less corrosion resistant due to compositional variations within the structure [19]. In sum, cpTi that has low impurities and no alloying elements possesses higher corrosion resistance than titanium alloys. In comparison to ($\alpha+\beta$) alloys, β titanium alloys generally exhibit superior corrosion resistance [19]. In term of Ti-6Al-4V, microstructure with acicular α phase has better corrosion resistance than $\alpha+\beta$ equiaxed microstructure, because the presence of α' martensite with all alloying elements present in it contributes to the formation of a more stable passive film than α and β phases [20].

2.3.2 Corrosion of Titanium Alloys in Human Body

Titanium and titanium alloys have been extensively used in orthopedic applications owing to their good biocompatibility, appropriate mechanical properties and excellent corrosion resistance. Ti-6Al-4V alloy was originally developed for aerospace applications and is the first

titanium alloy used as a biomaterial [20]. Under various environments it spontaneously forms passive oxides (mainly TiO_2), which plays an important role in determining the biocompatibility and corrosion resistance [21]. The passive film on titanium implants is mainly composed of TiO_2 , existing in a rutile-type tetragonal structure. The presence of this thermodynamically stable and adherent oxide contributes to high corrosion resistance. In Ti-6Al-4V, the V_2O_5 and Al_2O_3 in the passive film can easily dissolve and result in the lower film corrosion resistance [20].

It was reported that the microstructure of Ti-6Al-4V (either α plates or $\alpha+\beta$ equiaxed microstructure) can affect the thickness and quality of the passive film [20]. More porous and passive film can be formed on the surface of the two-phase ($\alpha+\beta$) Ti-6Al-4V than that in the acicular α phase [20]. Furthermore, the surface finish of orthopedic parts is another important design feature, because rough surface is more osteoconductive than smooth surface by promoting cell growth [22]. However, high friction coefficient and poor wear resistance is a problem for titanium alloys, and rough surface has higher corrosion rate than smooth surface in body fluid. In fact, Ti-6Al-4V alloys used for orthopedic applications are highly polished or being applied with porous coating.

In simulated body fluid environment (SBF), OH^- groups are absorbed by Ti ions in the oxide layer of titanium alloy implant. The isoelectric point of rutile is pH 5-6. At physiological pH (e.g., 7.4), TiO_2 gives up H^+ ions forming negatively charged Ti-O^- groups. The negative sites attract Ca_2^+ ions from the solution and to form a slightly charged calcium titanate layer, which subsequently attracts PO_4^{3-} ions which resulting in the formation of an unstable carbonated calcium phosphate (CaP) [23].

2.3.3 Characterization methods of Corrosion Behavior

Three-electrode electrochemical cell is usually used to determine the electrochemical and corrosion properties of the working electrode material. In an electrochemical cell, a reference electrode: saturated calomel electrode (SCE) or Ag/AgCl, a counter electrode, a working electrode (usually the tested material) and an electrolyte. The electrochemical cell is schematically shown in Figure 10.

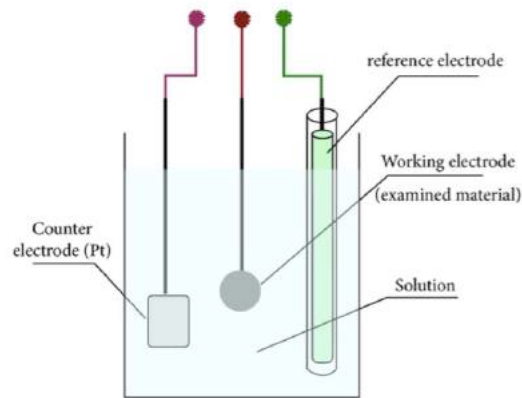


Figure 10: Schematic diagram of the electrochemical cell consists of reference electrode (Ag/AgCl), counter electrode (Pt wire), working electrode (examined material) and electrolyte.

The open circuit potential measurement is measuring the variation of isolated corrosion potential (E_{corr}) as a function of time in various environments. After immersion of the working electrode into the electrolyte, a rise in potential in the positive direction indicates the formation of a passive film, and a steady potential indicates that the film remains intact and protective. Generally, a drop of potential in the negative direction indicates breaks in the film, dissolution or no film formation [24]. The behavior of Ti-6Al-4V is that the potential moves towards the positive side means the formation of a protective oxide layer on the sample surface.

Cyclic polarization measurement is usually used by applying a forward scan from negative to more active (more cathodic) at a constant scan rate. The scan direction is reversed until the potential reached a certain value. The current density values are detected during this process. Tafel extrapolation is used to determine the corrosion current potential (E_{corr}) and corrosion current density (i_{corr}). Furthermore, the pitting potential (E_p in Figure 11) can be determined from cyclic polarization test. The pitting and crevice corrosion resistance of any coating/material, in general, can be evaluated based on the formation of a loop. Based on the area of loops, the ranking of the coating/material can be determined. Loop with higher area means poorer resistance to pitting and crevice, whereas, no loop means no susceptible to pitting and crevice corrosion [24]. A schematic diagram of cyclic polarization curve is shown in Figure 11 with Tafel extrapolation [25].

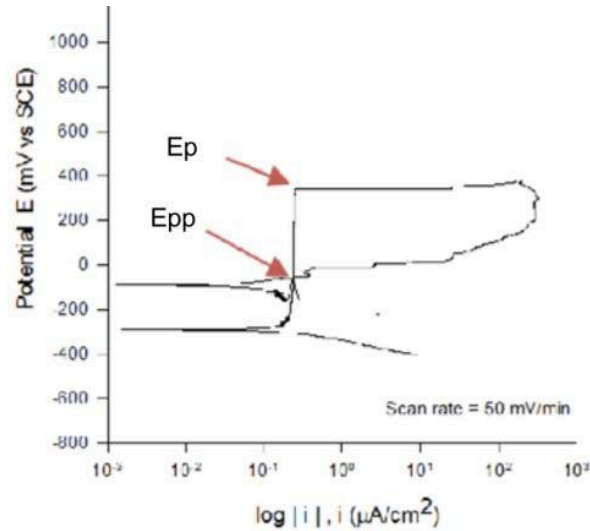


Figure 11: Schematic diagram of cyclic polarization curve [25].

Electrochemical impedance spectroscopy (EIS) is a non-destructive way to evaluate the electrochemical behavior evolution of the metallic material – electrolyte interface with time [25]. Fitting of the experimental results into the appropriate model is essential in revealing the correct electrochemical properties of the materials. Depends on the equivalent circuit that is fit with the experimental results, the conclusion can vary.

2.4 Alloy Selection – Ti-6Al-4V

2.4.1 Basic Knowledge of Titanium and Ti-6Al-4V

Titanium was discovered in 1790 but not purified until 1900s, but it has accumulated the experience of 50 years of modern industrial application to support its use. Most of the applications are in military aircraft [26]. Titanium and titanium alloys have two principal advantages: (1) high strength/weight ratio (the density of titanium is only about 60% of that of steel, and its tensile strength can be comparable to the lower-strength martensite stainless steel), and (2) outstanding corrosion resistance. Those two benefits enable the use of titanium alloys in various structural applications mainly in aerospace industry, marine environment and biomedical applications [27].

Titanium has two polymorphs: α which refers to the hexagonal-closed pack (HCP) structure, and β which is body center cubic (BCC) structure. The BCC structure of titanium is found only at high temperature, unless titanium is alloyed with other elements to maintain the BCC structure at low temperature [26]. Figure 12 shows the effect of some alloying elements on some selected

properties [26]. Depending on the influence on the phase transformation temperature, alloying elements are divided into α stabilizer which and β stabilizer. The α stabilizers (like Al, O) produce little change on the phase transformation temperature or cause it to increase, and they are simple metal or interstitial elements. The addition of β stabilizers, which are usually transition metals, can decrease the phase transformation temperature [27]. The unalloyed titanium and alloys with α stabilizers refer to α alloys (for example Ti-5Al-2.5Sn) with satisfactory strength, toughness, creep resistance and weldability, and the absence of a ductile-to-brittle transformation renders them good low temperature properties. The β alloys generally contain large amount of β stabilizers which render very good formability, but they are unsuitable for low temperature applications. In between of those, titanium alloys contain both α and β stabilizers and have a mixture of α and β phases refer to $\alpha+\beta$ alloys. They generally exhibit good fabricability as well as high room temperature strength, and moderate elevated-temperature strength. The mechanical properties of $\alpha+\beta$ titanium alloys can be controlled by heat treatments [27].

Al is a commonly used α stabilizer, and the Ti-Al binary phase diagram is shown in Figure 13 [28]. There are two important intermetallic compounds: Ti_3Al and $TiAl$ in the phase diagram, which can act as the age-hardening particles in the alloys [28]. In Figure 13, the two-phase $\alpha+\beta$ region is both narrow and high in temperature, the $\beta/(\alpha+\beta)$ and $(\alpha+\beta)/\alpha$ transus temperature is 1010 and 970 °C at 6 wt% Al, respectively [28]. The introduction of some amount of vanadium (β stabilizer) at constant aluminum concentration produces a rapid decrease of the $(\alpha+\beta)/\alpha$ transus temperature, and mildly decrease of $\beta/(\alpha+\beta)$ transus as shown in Figure 14 [28]. For Ti6Al4V (6 wt% Al and 4 wt% V), one of the most widely used $\alpha+\beta$ titanium alloys especially in aerospace and medical applications, the $\beta/(\alpha+\beta)$ transus temperature is about 995 °C [29].

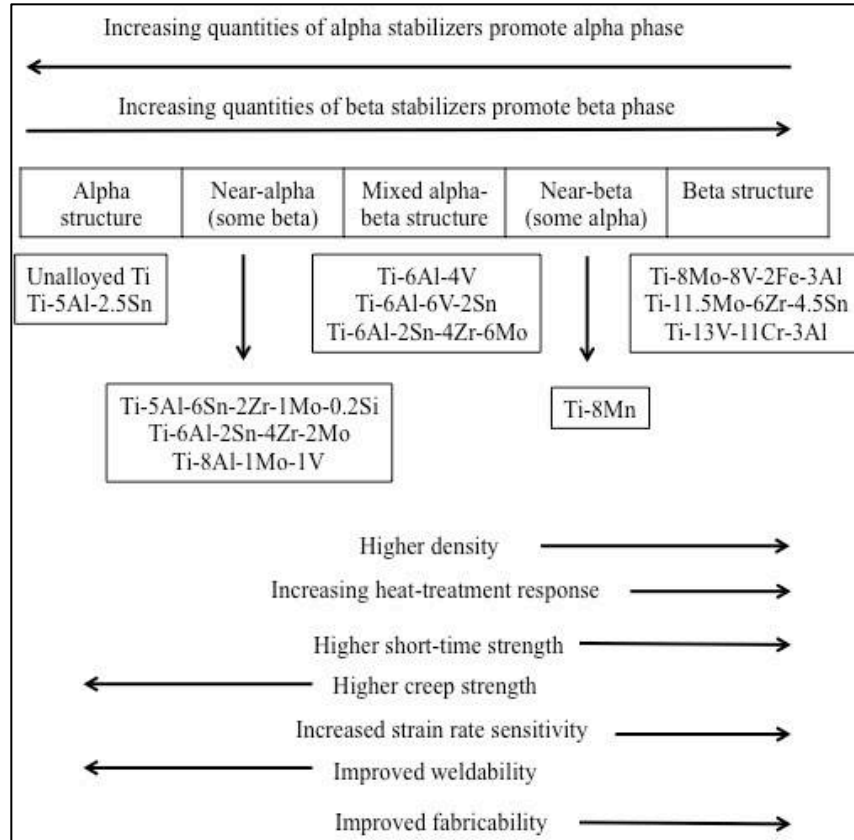


Figure 12: The effect of alloying elements on the selected properties of titanium alloys [26].

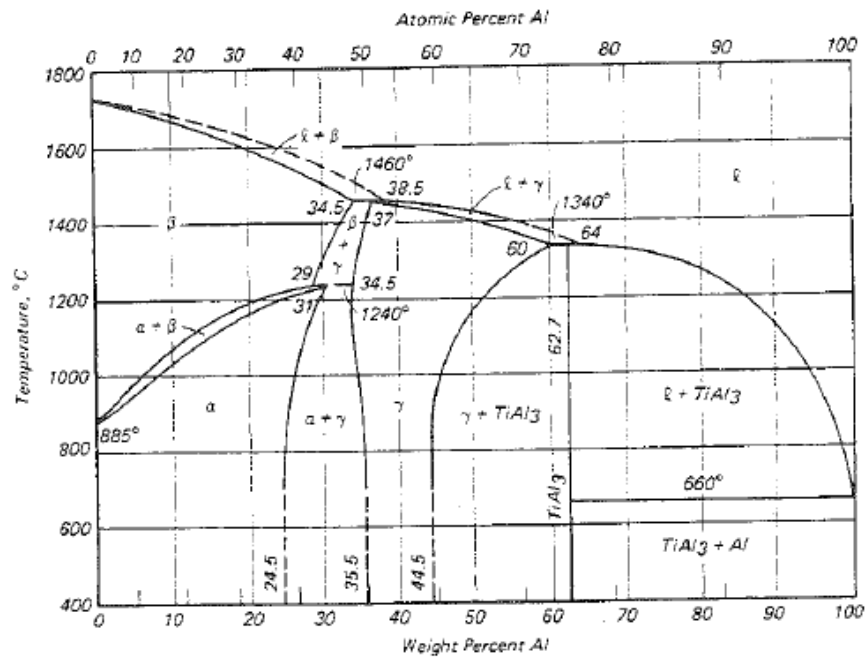


Figure 13: Equilibrium phase diagram of Ti-Al binary system [28].

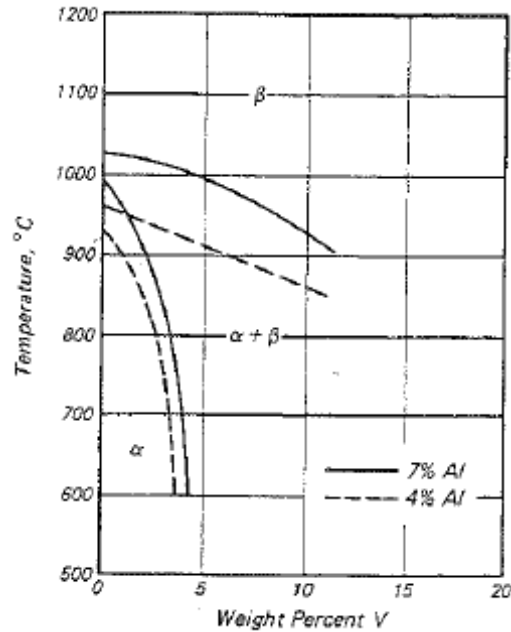


Figure 14: “Vertical” sections of the Ti-Al-V versus temperature at 4 and 7 wt% Al [29].

Ti-6Al-4V is an ($\alpha+\beta$) alloy with high strength to density ratio. The grade 5 Ti-6Al-4V alloy has an ultimate tensile strength of 950MPa, a yield strength of 880MPa, an elongation of 14% and the density is 4.43 g/cm³ [26]. The Vickers microindentation and Rockwell C hardness of grade 5 Ti-6Al-4V is 349 and 36, respectively. It also has excellent corrosion resistance by formation of a passive oxide layer (mainly TiO₂) with presence of moisture. The excellent biocompatibility of Ti-6Al-4V enables it to direct contact with tissue or bone. Ti-6Al-4V alloy has poor shear strength and wear resistance [26].

In this study, gas atomized Ti-6Al-4V pre-alloyed powder was used and its chemical composition is shown in Table 4.

Table 4: Chemical composition of gas atomized Ti-6Al-4V pre-alloyed powder.

Element	C	Al	N	O	V	Fe	H	Other	Ti
wt. %	0.10	6.75	0.05	0.02	4.50	0.40	0.015	0.40	Balance

2.4.2 Traditional Manufacturing of Ti-6Al-4V

Traditional manufacturing processes associated with titanium alloys include (1) casting, (2) wrought (forging/milling from ingots), (3) powder metallurgy (P/M). Wrought products account for 70% of the titanium and titanium alloy market [8]. Wrought titanium alloys undergo several

melt cycles in order to remove impurities such as hydrogen and other volatiles in order to produce a high purity ingot that is forged or milled into the final product. The cast titanium alloys require post-treatment including heat treatment and/or hot isostatic pressing (HIP) to eliminate porosity introduced during casting process [8].

Wrought Ti-6Al-4V alloy can be thermomechanically treated (cold/hot working and heat treatment) into a final shape, thus enabling tailoring of desired mechanical properties. Cast Ti-6Al-4V alloy has better crack propagation and creep resistance properties compared to wrought products [8]. Figure 15 shows the comparison of ultimate tensile strength, yield strength and elongation for two kinds microstructure of wrought products (α plates and $\alpha+\beta$) with cast Ti-6Al-4V in the HIPed conditions. It indicates that wrought materials generally exhibit superior mechanical properties as processed.

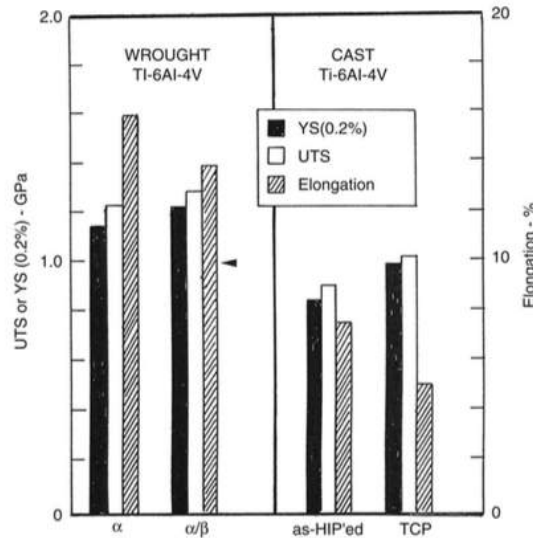


Figure 15: Ultimate tensile strength, yield strength and elongation of wrought products (α plates and $\alpha+\beta$) compared with as-HIPed cast and cast TCP treated Ti-6Al-4V [8].

2.4.3 Heat Treatment of Ti-6Al-4V

Based on ASM handbook, titanium and titanium alloys are heat treated in order to [30]:

- (1) Produce an optimum combination of ductility, machinability and dimensional stability via annealing.
- (2) Increase strength via solution treating and aging.
- (3) Reduce residual stresses developed during fabrication via stress relieving.

Annealing treatment of Ti-6Al-4V alloy is recommended is the temperature range of 705-790°C for 1-4 hours and followed by air or furnace cooling. It is always applied to increase fracture toughness, ductility at room temperature, dimension and thermal stability and creep resistance. As mentioned above, solution treatment and aging is able to increase strength of titanium alloys. By varying temperature, time and cooling rate, a wide range of strength level can be obtained in $\alpha+\beta$ or β alloys. A recommended solution treatment condition for Ti-6Al-4V alloy is list in Table 5. The solution treatment is usually applied below but close to β transus temperature, and the aging temperature can be low with longer time or high with shorter time.

Table 5: Recommended solution treatment and aging procedure for Ti-6Al-4V [30].

Alloy	Solution treatment			Aging		
	Temperature (°C)	Time (h)	Cooling	Temperature (°C)	Time (h)	Cooling*
Ti-6Al-4V	955-970	1	Water	480-595	4-8	air-cooling
	955-970	1	Water	705-760	2-4	air-cooling

The undesirable residual stresses in Ti-6Al-4V alloy that result from non-uniform temperature in hot forging, deformation from cold forming and even laser sintering can be reduce in some amount through stress relieving treatment. Titanium and titanium alloys can be stress relieved without affecting strength or ductility [30]. According to ASM handbook, a recommended solution treatment condition for Ti-6Al-4V alloy is under 480-650°C for 1-4 hours. The rate of cooling from the stress-relieving temperature is not critical, but the uniformity of cooling is very critical.

Reference

- [1] Cabrini, M., Lorenzi, S., Pastore, T., Pellegrini, S., Pavese, M., Fino, P., ... & Manfredi, D. (2016). Corrosion resistance of direct metal laser sintering AlSiMg alloy. *Surface and Interface Analysis*.
- [2] Grünberger, T., & Domröse, R. (2015). Direct Metal Laser Sintering. *Laser Technik Journal*, 12(1), 45-48.
- [3] EOS GmbH Electro Optical Systems (2012): EOS system data sheet M 280.
- [4] Mierzejewska, Ż. A. (2015). Process optimization variables for direct metal laser sintering. *Advances in Materials Science*, 15(4), 38-51.
- [5] Vrancken, B., Thijs, L., Kruth, J. P., & Van Humbeeck, J. (2012). Heat treatment of Ti6Al4V produced by selective laser melting: microstructure and mechanical properties. *Journal of Alloys and Compounds*, 541, 177-185.
- [6] Kruth, J. P. (1991). Material in-process manufacturing by rapid prototyping techniques. *CIRP Annals-Manufacturing Technology*, 40(2), 603-614.
- [7] Wang, K. (1996). The use of titanium for medical applications in the USA. *Materials Science and Engineering: A*, 213(1), 134-137.
- [8] Murr, L. E., Quinones, S. A., Gaytan, S. M., Lopez, M. I., Rodela, A., Martinez, E. Y., ... & Wicker, R. B. (2009). Microstructure and mechanical behavior of Ti-6Al-4V produced by rapid-layer manufacturing, for biomedical applications. *Journal of the mechanical behavior of biomedical materials*, 2(1), 20-32.
- [9] Al-Bermani, S. S., Blackmore, M. L., Zhang, W., & Todd, I. (2010). The origin of microstructural diversity, texture, and mechanical properties in electron beam melted Ti-6Al-4V. *Metallurgical and materials transactions A*, 41(13), 3422-3434.
- [10] Conway, J. J., & Rizzo, F. J. (1998). Hot isostatic pressing of metal powders. *ASM Handbook*, 7, 605-620.
- [11] Das, S., Wohler, M., Beaman, J. J., & Bourell, D. L. (1998). Producing metal parts with selective laser sintering/hot isostatic pressing. *JoM*, 50(12), 17-20.
- [12] Al-Bermani, S. S., Blackmore, M. L., Zhang, W., & Todd, I. (2010). The origin of microstructural diversity, texture, and mechanical properties in electron beam melted Ti-6Al-4V. *Metallurgical and materials transactions A*, 41(13), 3422-3434.
- [13] Facchini, L., Magalini, E., Robotti, P., & Molinari, A. (2009). Microstructure and mechanical properties of Ti-6Al-4V produced by electron beam melting of pre-alloyed powders. *Rapid Prototyping Journal*, 15(3), 171-178.

- [14] Vilaro, T., Colin, C., & Bartout, J. D. (2011). As-fabricated and heat-treated microstructures of the Ti-6Al-4V alloy processed by selective laser melting. *Metallurgical and Materials Transactions A*, 42(10), 3190-3199.
- [15] Long, M., & Rack, H. J. (1998). Titanium alloys in total joint replacement—a materials science perspective. *Biomaterials*, 19(18), 1621-1639.
- [16] Lowman, E. W. (1955). Osteoarthritis. *Journal of the American Medical Association*, 157(6), 487-488.
- [17] Le Guéhennec, L., Soueidan, A., Layrolle, P., & Amouriq, Y. (2007). Surface treatments of titanium dental implants for rapid osseointegration. *Dental materials*, 23(7), 844-854.
- [18] Niinomi, M. (2003). Recent research and development in titanium alloys for biomedical applications and healthcare goods. *Science and technology of advanced Materials*, 4(5), 445.
- [19] Geetha, M., et al. "Influence of microstructure and alloying elements on corrosion behavior of Ti-13Nb-13Zr alloy." *Corros. Sci.*, 46(4) (2004), 877-892.
- [20] Cvijović-Alagić, I., Cvijović, Z., Mitrović, S., Panić, V., & Rakin, M. (2011). Wear and corrosion behaviour of Ti-13Nb-13Zr and Ti-6Al-4V alloys in simulated physiological solution. *Corrosion Science*, 53(2), 796-808.
- [21] Shukla, A. K., Balasubramaniam, R., & Bhargava, S. (2005). Properties of passive film formed on CP titanium, Ti-6Al-4V and Ti-13.4 Al-29Nb alloys in simulated human body conditions. *Intermetallics*, 13(6), 631-637.
- [22] Traini, T., Mangano, C., Sammons, R. L., Mangano, F., Macchi, A., & Piattelli, A. (2008). Direct laser metal sintering as a new approach to fabrication of an isoelastic functionally graded material for manufacture of porous titanium dental implants. *Dental materials*, 24(11), 1525-1533.
- [23] Shah, F. A., Trobos, M., Thomsen, P., & Palmquist, A. (2016). Commercially pure titanium (cp-Ti) versus titanium alloy (Ti6Al4V) materials as bone anchored implants—is one truly better than the other?—review. *Materials Science and Engineering: C*.
- [24] Gurrappa, I. (2003). Characterization of titanium alloy Ti-6Al-4V for chemical, marine and industrial applications. *Materials Characterization*, 51(2), 131-139.
- [25] Massaro, C., Rotolo, P., De Riccardis, F., Milella, E., Napoli, A., Wieland, M., ... & Brunette, D. M. (2002). Comparative investigation of the surface properties of commercial titanium dental implants. Part I: chemical composition. *Journal of Materials Science: Materials in Medicine*, 13(6), 535-548.
- [26] Donachie, M. J. (2000). *Titanium: a technical guide*. ASM international.

- [27] Collings, E. W. (1984). The physical metallurgy of titanium alloys. *American Society for Metals*, 1984, 261.
- [28] Welsch, G., Boyer, R., & Collings, E. W. (Eds.). (1993). Materials properties handbook: titanium alloys. *ASM international*.
- [29] Ding, R., Guo, Z. X., & Wilson, A. (2002). Microstructural evolution of a Ti–6Al–4V alloy during thermomechanical processing. *Materials Science and Engineering: A*, 327(2), 233-245.
- [30] ASM International. Handbook Committee. ASM Handbook: Heat Treating. Vol. 4. Asm Intl, 1991.

CHAPTER 3

PAPER I: INVESTIGATIONS ON FACTORS INFLUENCE THE CORROSION BEHAVIOR OF DIRECT METAL LASER SINTERED Ti-6Al-4V

Yangzi Xu, Jianyu Liang, Richard D. Sisson, Jr.

Submitted to: *Journal of Biomedical Materials Research Part A* (Manuscript form)

Highlights:

1. Several factors in the laser-processed parts can affect their corrosion behavior: microstructure, surface roughness and surface pores. The as-printed parts have higher corrosion rate than the reference alloy under smooth surface, but heat-treated sample has improve corrosion resistance. The existence of surface pores can decrease the crevice corrosion resistance of laser-processed parts.
2. The three-dimensional surface roughness (S_a) shows positive correlation on the calculated corrosion rate: a rough surface finish possesses higher corrosion rate than smooth surface finish.

Investigations on Factors Influence the Corrosion Behavior of Direct Metal Laser Sintered Ti-6Al-4V

Yangzi Xu^{1*}, Jianyu Liang¹, Richard D. Sisson, Jr¹

¹Department of Materials Science and Engineering, Worcester Polytechnic Institute, 100 Institute Road, Worcester, MA 01609, USA

Abstract

In this study, the effects of microstructure, surface roughness and surface porosity on the corrosion behavior of direct metal laser sintered (DMLS) Ti-6Al-4V were experimentally investigated. The three-electrode method was used to conduct electrochemical measurements of the specimens in Ringer's solution at 37°C. The acicular microstructure in the DMLS Ti-6Al-4V samples give rise to a better corrosion resistance than the Grade 5 alloy with an equiaxed microstructure. Electrochemical results indicate that microstructure and surface roughness has a positive correlation with the corrosion behavior of the samples. Pits and cracks can be observed near the edge of original surface pores in the as-printed sample after 1 month immersion in simulated body fluid. The data indicate that acicular microstructure with less surface pore and lower surface roughness contributes to better corrosion resistance.

Key Words

Ti-6Al-4V; direct metal laser sintering; microstructure; surface roughness; surface pores

* Corresponding author at: Worcester Polytechnic Institute, Department of Materials Science and Engineering.
Tel: +1 508 831 8333

E-mail address: yxu@wpi.edu (Y. Xu.)

1. Introduction

Additive manufacturing is a process to create parts by the addition of materials layer by layer.¹ Direct Metal Laser Sintering (DMLS) is an additive manufacturing process that can direct build three-dimensional (3D) metallic components from metal powders in accordance with a sliced 3D computer aided design (CAD) model.² Due to the advantage of rapid prototyping techniques to create highly complex freeform objects, they are good candidates to be used in biomedical applications for customized implants. Titanium and its alloys have been fully commercialized in orthopedic and dental implants due to their high strength-to-weight ratio, good mechanical properties, corrosion resistance, chemical inertness and biocompatible.³ Pure titanium and Ti-6Al-4V alloy are widely used in total knee replacement, hip replacement and dental implants. Although titanium alloys have good corrosion behavior from the protective oxide film (mainly TiO₂), these alloys can be attacked by pitting and crevice corrosion. Localized breakdown of protective film leads to formation of pits.⁴ These pits can grow and propagate into macroscopic crack and leads to catastrophic failure. Atwood et al. reported a case of corrosion-induced fracture of hip implant on the stem neck caused by localized corrosion pits.⁵ They observed three regions on the retrieved implant surface: (1) a large pit initiated by crevice corrosion; (2) a region indicating catastrophic failure and (3) tearing.⁵ Therefore, improving the pitting corrosion resistance of an implant material is helpful in extending the lifetime.

Since the high thermal input and quick cooling rate in DMLS will generate Ti-6Al-4V with acicular microstructure and residual porosity, therefore, significant amount of efforts have been put on the optimization of the mechanical properties of as-printed Ti-6Al-4V samples by applying various post-treatment, including heat treatment and hot isostatic pressing.^{6,7} It has been reported that post-annealing treatment can improve the ductility and reduce Young's modulus to reach the acceptable values for biomedical materials, because high modulus of implants may cause the "stress shielding" effect.⁸ Microstructure of the specimens may change during post-treatments, which can affect the corrosion behavior. Furthermore, the surface morphology of orthopedic implants is also an important design feature, because rough surface is more osteoconductive than smooth surface by promoting cell growth.³ For the purpose to improve the pitting and crevice corrosion resistance of additively manufactured Ti-6Al-4V alloy in body environment, the factors that influence the corrosion behavior need to be investigated. This work experimentally examined the effect of microstructure, surface roughness and surface pores on the

corrosion resistance of direct metal laser sintered Ti-6Al-4V in simulated body fluid. The corrosion behavior of Grade 5 hot forged and mill annealed Ti-6Al-4V sample was also analyzed for comparison. Crevice corrosion tests were performed in Ringer's solution and the post-surface morphologies were examined microscopically.

2. Materials and Methods

2.1 Materials and sample preparation

The Ti-6Al-4V specimens were fabricated by EOS e-Manufacturing Solutions (Krailing, Germany) using direct metal laser sintering (DMLS) method. Samples were printed at a scanning speed of 1250 mm/s, a laser power of 340W, a hatch spacing of 120 μ m and a layer thickness of 60 μ m under an alternative scanning strategy. Samples were cut into cubes and degreased in acetone before heat-treated in a vacuum furnace at 799 $^{\circ}$ C for 4 hours followed by air-cooling. The commercial Grade 5 Ti-6Al-4V specimens were obtained from a commercial supplier. Sample preparation for metallography was carried out by grinding to 1200 series SiC sand paper, and followed by final finish on a ChemoMet polishing mat using colloidal silica suspension to achieve a mirror finish. Kroll's reagent (2 ml HF, 5 ml HNO₃ and 100 ml H₂O) was used to reveal the microstructure. Other two kinds of surface finishes were applied besides the mirror finish: (1) rough finish by grinding to 1200 series SiC sand paper, and (2) medium finish by polishing to 0.03 μ m alumina water paste on MicroCloths mat. All the samples were degreased in acetone by ultrasonic cleaning before further measurements.

2.2 Characterization techniques

Surface morphology analysis was performed using an Olympus confocal laser microscopy OLS LEXT 4100 with 100x objective. The examined area was 130 \times 130 μ m. The MountainsMap[®] Premium 7.1 software was used to analyze the generated three-dimensional images. Six independent measurements were conducted on each sample, and the average three-dimensional surface roughness (S_a) was calculated, it can be mathematically expressed using Equation (1):

$$S_a = \int \int_a |Z(x,y)| dx dy \quad (1)$$

in which the integration of height is over the area of measurement represents by a . The developed interfacial area ratio (S_{dr}) values were also measured from the software, which

expresses the percentage of the interfacial surface area relative to the area of the projected plane as shown in Equation (2):⁹

$$Sdr = \frac{(Texture\ Surface\ Area - Cross\ Sectional\ Area)}{Cross\ Sectional\ Area} \times 100\% \quad (2)$$

in which the “texture surface area” refers to the total area of all triangles comprised the texture at the defined resolution, and “cross sectional area” is the area of the projected plane.⁹ Metallography analysis was conducted on a JEOL JSM-7000F scanning electron microscopy (SEM). A PANanalytical Empyrean 2 X-ray diffractometer (XRD) with Cu-K_α radiation at 45 keV and 40 mA was used for phase identification. The average lath thickness and surface porosity of as-printed and heat-treated samples were analyzed using ImageJ software.

2.3 Crevice corrosion tests

The mirror finished as-printed and heat-treated Ti-6Al-4V samples were weighted and assembled with a glass slide for crevice corrosion behavior evaluation. As schematically shown in Figure 1, the investigated sample was attached to an ultrasonic cleaned glass slide, and fixed with rubber band. The whole device was assembled in Ringer’s solution to ensure electrolyte filled in the crevice area. The crevice corrosion device was then immersed in the electrolyte for 1, 1.5 and 2 months at 37°C. After immersion, the samples were dried and weighted, then ultrasonic cleaned in acetone before further surface morphology analysis.

The percent weight change of immersed sample was calculated using Equation (3):

$$Percent\ weight\ change = \frac{(weight\ after\ immersion - initial\ weight)}{initial\ weight} \times 100\% \quad (3)$$

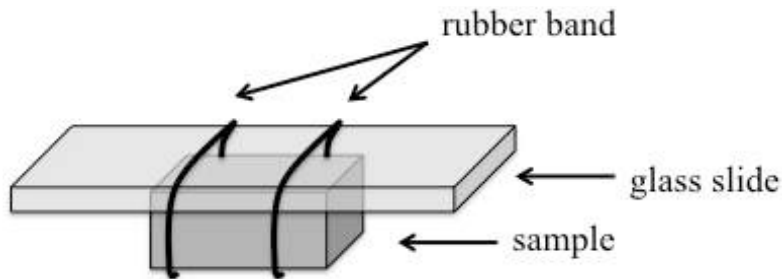


Figure 1: Schematic diagram shows the assembly method of the investigated sample for crevice corrosion test. Well-prepared sample surface was attached to an ultrasonic cleaned glass slide,

and fixed with rubber bands. The whole device was immersed in Ringer's solution and was maintained at 37°C.

2.4 Electrochemical measurements

The electrochemical measurements were conducted in a three-electrode cell with Ag/AgCl (3M NaCl) as the reference electrode, a Platinum wire (surface area: 3.6 cm²) as the counter electrode and the mounted Ti-6Al-4V sample (with one surface exposed to the electrolyte) as the working electrode. All electrode potentials are referred to the reference Ag/AgCl electrode. The electrolyte was naturally aerated Ringer's solution (6.5 g/l NaCl, 0.14 g/l KCl, 0.12g/l CaCl₂, 0.2g/l NaCO₃ and 0.4g/l glucose) with a pH of 6.5 in a 100ml cell. The three-electrode cell was maintained at 37°C during the measurements. A potentiostat (Bio-Logic, Inc.) was used to measure the open circuit potential after immersion of the working electrode until the potential reached a plateau value, and then generated cyclic polarization curves. A forward scan started from -1000 mV and moves anodically at a constant scan rate of 1 mV/s to higher potential. The scan direction was reversed until the potential reached 3000 mV. Bio-Logic® software was used to analyze the electrochemical parameters. The resulting corrosion current density values were normalized using Equation (4):

$$\text{Corrosion current density } (\mu\text{A}/\text{cm}^2) = \frac{\text{corrosion current } (\mu\text{A})}{\text{texture surface area } (\text{cm}^2)} \quad (4)$$

in which the corrosion current was extrapolated from the polarization results using Tafel plot, and texture surface area value was calculated from Equation (2) by the known Sdr. Corrosion rate represents the rate of weight loss per unit area was calculated using Equation (5):¹⁰

$$\text{Corrosion rate } (\text{mpy}) = \frac{0.13 \times I_{\text{corr}} \times EW}{\rho} \quad (5)$$

in which I_{corr} refers to the corrosion current density in $\mu\text{A}/\text{cm}^2$; EW is the equivalent weight of the investigated sample,¹¹ and ρ is the density of the investigated sample in g/cm^3 . Density of the Grade 5 Ti-6Al-4V alloys is $4.43 \text{ g}/\text{cm}^3$.⁸ Conversions to equivalent metric corrosion rate are listed in Equation (6):¹⁰

$$1 \text{ mpy} = 0.0254 \text{ mm/yr} = 25.4 \text{ }\mu\text{m/yr} \quad (6)$$

Considering the existence of pores in the DMLS samples, the equivalent density of the as-printed and heat-treated samples were calculated using Equation (7):

$$\text{Equivalent density} = \text{bulk density} \times (100\% - \text{surface porosity}) \quad (7)$$

in which the bulk density of Ti-6Al-4V alloys is 4.43 g/cm^3 , and surface porosity was measured via image analysis.

3. Results and Discussion

3.1 Microstructure and phase analysis

The scanning electron microscopy (SEM) images of the as-printed, heat-treated and Grade 5 Ti-6Al-4V are shown in Figure 2 (a), (c) and (d), respectively. Predominantly acicular α' acicular martensite microstructure can be observed in the as-printed sample, which is mainly due to the rapid cooling during DMLS. Fine β precipitates dispersed throughout the α' matrix can be seen at high magnification as shown in Figure 2 (b). Similar observation was reported by de Damborenea et al. in the as-printed Ti-6Al-4V, which was caused by rapid quench induced martensitic transformation in the β -phase.¹² After post-annealing treatment at 799°C for 4 hr, α' phase decomposed into $\alpha + \beta$ with coarsened α lath. The average lath thickness in the as-printed and heat-treated sample is $327 \pm 53 \text{ nm}$ and $935 \pm 104 \text{ nm}$, respectively. This observation is consistent with the finite elements simulation results reported by Katarov et al., where higher holding time at ($\alpha + \beta$) region will lead to coarser α lamellae thickness.¹³ The porosity value decreased from 0.29% in as-printed sample to 0.074% after annealing treatment, because some lack of fusion regions can be re-sintered during annealing treatment. Figure 2(d) shows the microstructure of equiaxed $\alpha + \beta$ phase in the reference Grade 5 Ti-6Al-4V alloy. The X-ray diffraction patterns of the as-printed, heat-treated and reference Ti-6Al-4V alloy are shown in Figure 3. Rapid cooling rate during DMLS leads to α' acicular martensite in the as-printed sample. After ($\alpha + \beta$) annealing, β phase can be observed. It is clear that the reference Grade 5 sample with hot forged and mill annealed allows sufficient recrystallization and growth comprises of even higher amount of β phase.¹⁴

Table 1: Three-dimensional surface roughness S_a values (with standard deviation) and hybrid parameters Sdr of the as-printed, heat-treated and reference samples under different surface finishes.

Sample	S_a (nm)	Sdr (%)
as-printed (rough)	91 (4.4)	6.49
as-printed (medium)	52.7 (8.8)	0.29
as-printed (smooth)	4.7 (0.8)	0.0154
heat-treated (rough)	89.9 (9.5)	8.29
heat-treated (medium)	55.2 (13.3)	0.24
heat-treated (smooth)	6.4 (1.7)	0.0185
reference (rough)	82.6 (7.1)	6.19
reference (medium)	42.8 (5.6)	0.316
reference (smooth)	5 (0.9)	0.033

3.2 Surface morphologies

Different surface finishes were applied on the as-printed, heat-treated and reference Ti-6Al-4V samples to evaluate the effects on corrosion resistance. The topography images obtained from confocal microscopy for as-printed sample are shown in Figure 4. The rough finished surface is comprised of pores and unidirectional scratches [Figure 4(a)], and depth of the scratches was approximately $0.3\mu\text{m}$ according to the palette. The medium finish is able to produce a smoother surface but obviously remains some scratches and surface defects [Figure 4(b)]. It was commonly accepted that additive manufactured parts, including both laser and electron beam as energy input, possess structural defects caused by several reasons: entrapped gas, insufficient energy input, defects from the pre-alloyed powder particles, poor designed scanning pattern.^{6,7} The highlighted blue dots with depth of approximately $0.5\mu\text{m}$ in Figure 4(b) are evidence of the defects. The smooth finished surface shown in Figure 4(c) reveals the acicular microstructure due to the light etching effect of silica suspension. The topography image of a typical surface pore is shown in Figure 4(d).

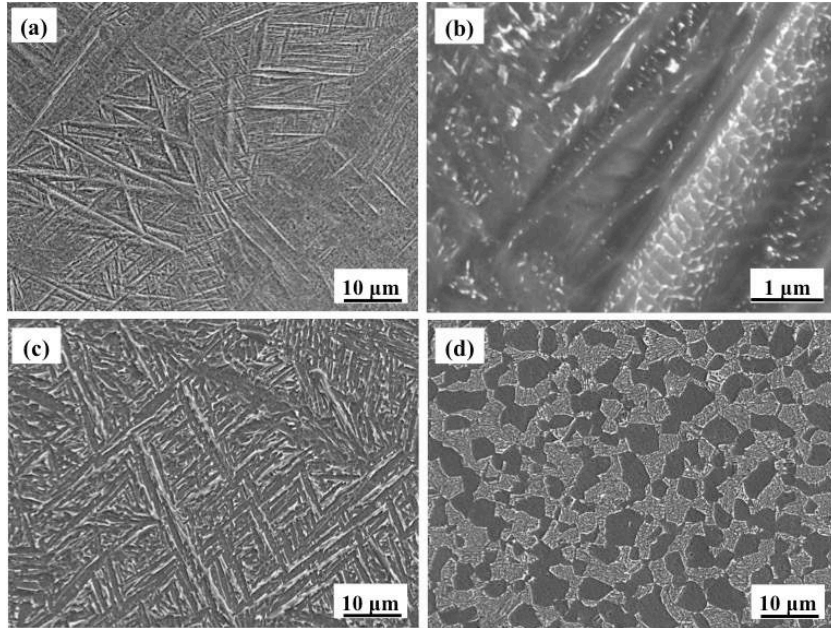


Figure 2: SEM images of (a) as-printed sample with fully acicular martensitic microstructure comprised mainly of α' needles, (b) high magnification of as-print sample shows nano-scaled β precipitates dispersed throughout the matrix, (c) heat-treated sample with coarsened microstructure and (d) the Grade 5 reference Ti-6Al-4V alloy with equiaxed microstructure.

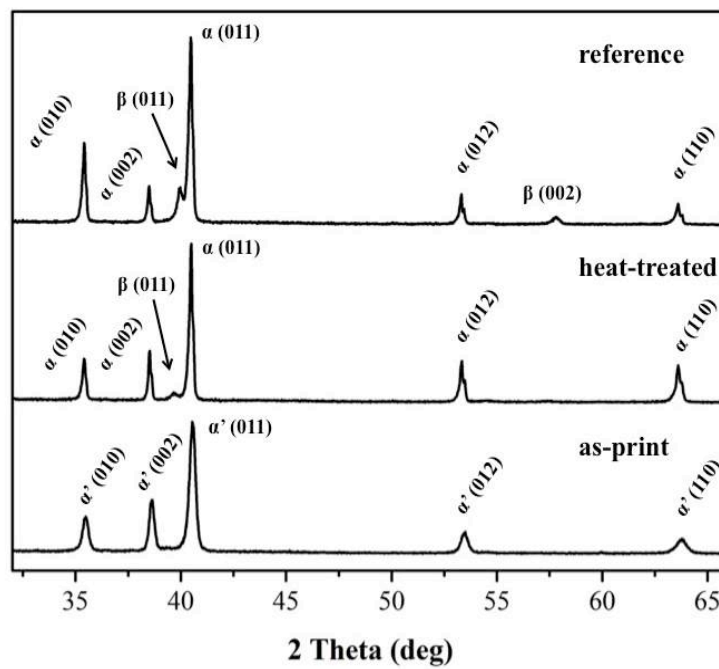


Figure 3: X-ray diffraction patterns of the as-printed, heat-treated and the reference (Grade 5) Ti-6Al-4V alloys.

The three-dimensional surface roughness (S_a values) of as-printed, heat-treated and reference samples with different surface finishes are listed in Table 1. The S_a values increase in the order: smooth finish < medium finish < rough finish for all of the investigated samples. In accordance with the topography morphology images in Figure 4, the rough finished samples with scratches have the highest surface roughness with the S_a values in the range of 82 to 91nm, and the smooth finish can achieve a surface with lower S_a values (in the range of 5 to 6.4 nm) than medium finished sample (S_a in the range of 42 to 56nm). The hybrid parameter Sdr (the developed interfacial area ratio) results are listed in Table 1. Generally, surface with a higher S_a value may possess higher Sdr indicates a more intricate surface texture. The results indicate reference Ti-6Al-4V sample always have a lower Sdr compared to the DMLS samples under same surface finish, because surface defects will contribute to higher texture surface area in the DMLS samples.

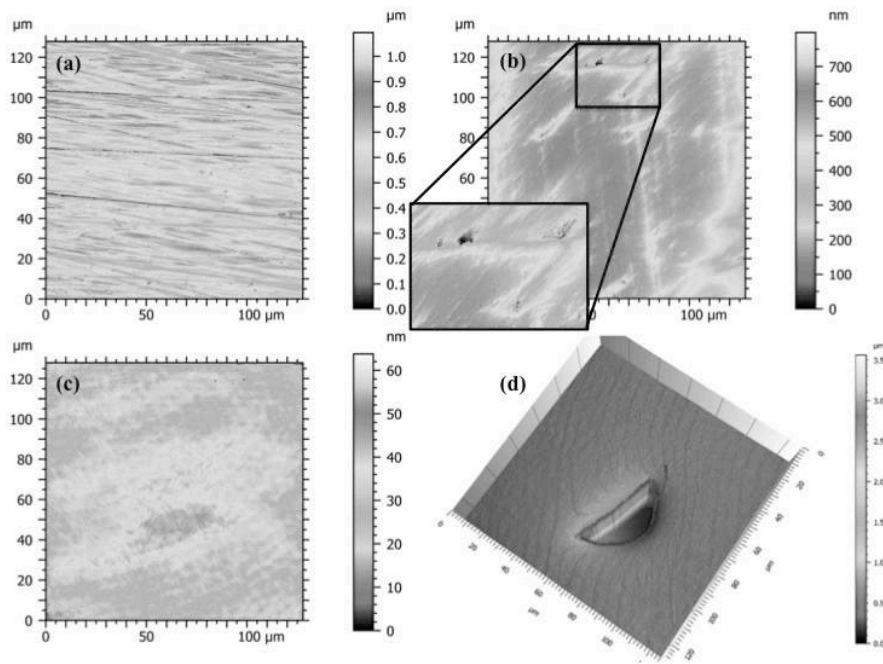


Figure 4: Topography images obtained from confocal microscopy (x100) of the as-print DMLS Ti-6Al-4V specimens with various surface finishes: (a) rough surface, (b) medium finished surface, and (c) smooth surface. The morphology and dimension of a surface pore is shown in (d). Palette on the right hand side indicates scale for the corresponding topography image.

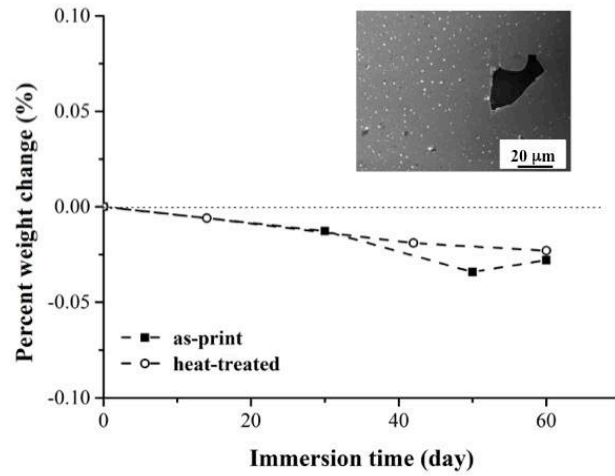
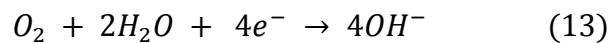
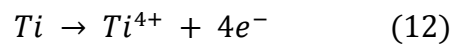


Figure 5: The variation of percent weight change during immersion time for the as-printed and heat-treated samples with smooth surface. The inset is a SEM image of as-printed sample after 2 month immersion with a surface pore and random salt deposition.

3.3 Crevice corrosion tests

The percent weight change of smooth finished as-printed and heat-treated samples after immersion in Ringer's solution for various time periods are shown in Figure 5. Both samples experienced weight loss, which indicates corrosion reaction took place during immersion, and the as-printed sample had a higher amount of weight loss than the heat-treated samples. The as-printed sample had a weight gain after immersion for 50 days, which is likely caused by salt deposition as shown in the inset in Figure 5 or reduced corrosion during this period of immersion time. Generally, in a coupled crevice corrosion set, the more anodic metal will be corroded and have significant weight loss.¹⁵ In the uncoupled set, both cathode and anode are on the same material and they may be close to each other.¹⁵ In the crevice cell, the existing surface pores filled with higher amount of stagnant electrolyte could be the oxygen rich area, and the crevice near the pores can be the oxygen-depleted area. Therefore, the anodic reaction shown in Equation (12) may happen on the surface near the pores, and the electrons transformed to the pores where the cathodic reaction shown in Equation (13) takes place:



This process could lead to a weight loss of the material, especially the formation of pits near the original surface pores. The SEM images in Figure 6 reveal the surface morphology of the mirror finished as-printed sample after 1 month immersion. The pores marked as P1 and P2 were the processing defects caused by DMLS, and the highlighted region in Figure 6(b) indicates the developed pits and cracks on the surface near the origin pores due to crevice corrosion, while the surface away from the pores were remain intact. It was reported that localized pits could form when the protective film breaks down, once that occurs, the growth of the pits can be very fast and develop into cracks.⁴ As shown in Figure 6(b), cracks formed on the edge and propagate into the bulk materials, and they can leads to release of the attacked species, which is a reason for the detected weight loss. Since the heat-treated sample possesses a lower porosity compared to the as-printed sample, it is less likely to have localized pits developed near the pores. Therefore, the presence of surface pores can deteriorate the pitting corrosion resistance of the alloy.

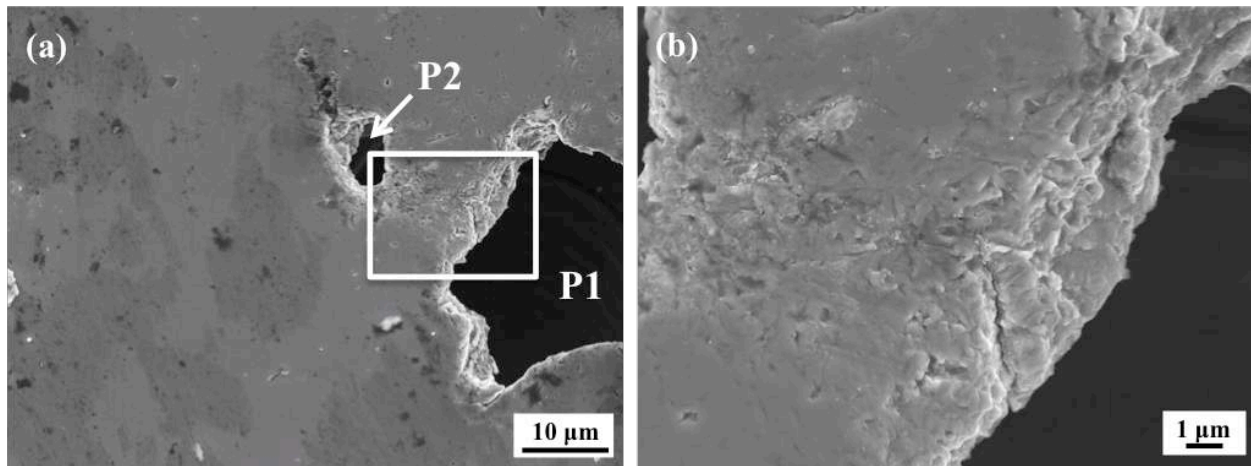


Figure 6: Morphology of smooth finished as-printed sample after immersion in Ringer's solution (37°C) for 1 month. The highlighted regions are shown in (b) indicates the developed pits and cracks.

3.4 Electrochemical results

Figure 7(a) and (b) shows the cyclic polarization plots for the as-printed and heat-treated Ti-6Al-4V samples under rough and smooth surface finish, respectively. The corrosion parameters deduced from these curves are listed in Table 2. The corrosion potential (E_{corr}) is an indicator of the stability of surface condition. Thus less variability of E_{corr} values in a specific sample under different surface finishes indicates a consistent surface processing.⁴ The corrosion current density

(I_{corr}) and calculated corrosion rate represents the amount of weight loss of the investigated materials under a corrosive environment. The resulting I_{corr} and calculated corrosion rate decreased in the order: rough finish > medium finish > smooth finish in all the investigated samples, which means rough finished samples lost more material than the others, and smooth finished ones lost less. The corrosion behavior also can be characterized by the breakdown potential (E_b) which are listed in Table 2. The metal maintains passive until the potential reaches E_b and undergoes corrosion reaction.⁵ In the investigated samples, E_b values decreased in the order: smooth finish > medium finish > rough finish, which indicates rough finished samples may have a greater chance to form pits.

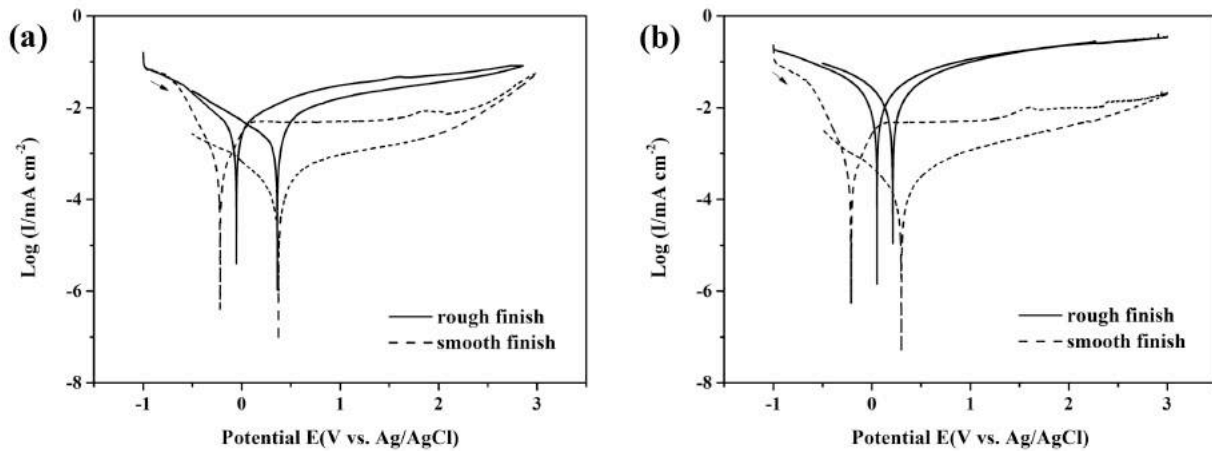


Figure 7: Cyclic polarization plots of the (a) as-printed and (b) heat-treated Ti-6Al-4V samples under rough and smooth surface finish.

The relationships between surface roughness (S_a values) and calculated corrosion rate of the as-printed, heat-treated and reference Ti-6Al-4V samples are plotted in Figure 8. Based on the analysis, the following observations can be made:

(1) Based on the fitting results, surface roughness S_a has a positive correlation with the corrosion rate of all samples under the tested conditions. It was reported by de Damborenea et al. that the existing surface defects via direct metal laser sintering can deteriorate the corrosion behavior and might act as crevice nucleation sites.¹² Moreover, the valley in scratches on the rough finish surface could act as the oxygen-depleted region, which can form localized galvanic couple with the oxygen rich area and impact the corrosion resistance.¹⁵ For the purpose of biomedical implants, a rough surface is usually desired to enhance osteointegration, however, rough surface

could provide more area for corrosion reaction to take place and increase the corrosion rate. Therefore, suitable surface treatments, for instances surface anodizing or coatings, may be applied on the implant materials to ensure osteointegration as well as good corrosion resistance.³

(2) The heat-treated sample possesses the lowest corrosion rate under all the surface finishes. This is mainly due to their difference in the microstructure. The acicular microstructure in the DMLS (as-printed and heat-treated) samples with limited alloying elements partitioning can formed a more uniform and stable protective oxide film than the equiaxed $\alpha+\beta$ microstructure in the reference sample.¹⁶ It was reported that the discontinuous outer oxide layer in the reference sample (mainly comprised of Al_2O_3) could cause localized breakdown of oxide film and reduced corrosion resistance. In the as-printed samples, the fast interaction during DMLS leads to the unstable α' microstructure with surface defects, and the post-heat treatment retains the lath microstructure and reduced defects. Therefore, higher corrosion resistance could be observed in the heat-treated samples.

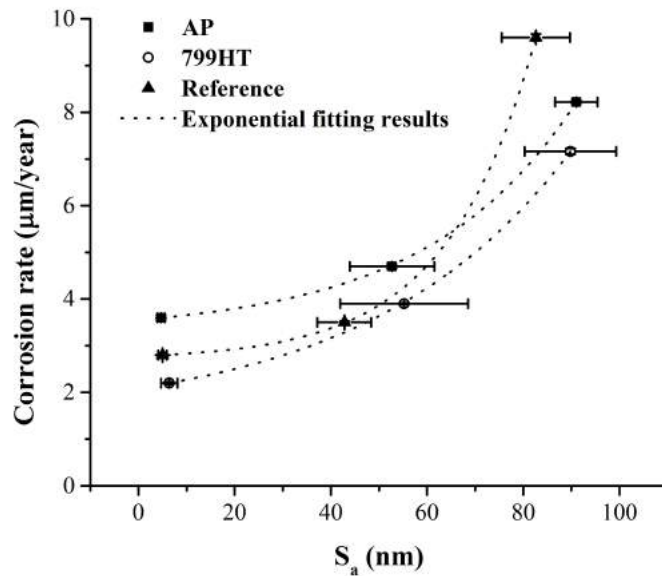


Figure 8: Plots on the effects of surface roughness (S_a) on the corrosion rate in as-printed, heat-treated and the reference Ti-6Al-4V samples.

(3) Interestingly, the as-printed sample has higher corrosion rate than the reference sample under low surface roughness, but lower corrosion rate under high surface roughness. The existence of surface pores in the as-printed sample could be the reason for its high corrosion rate under

smooth finish, because the reference sample is free of surface defects. Whereas, the effect of surface pores may be negligible under rough finish because the surface was covered by scratches as shown in Figure 4(a). Thus, the electrochemical results are consistent with the crevice test phenomenon that surface pores can impact the pitting corrosion resistance.

Table 2: Electrochemical parameters of the investigated samples under different surface finishes

Sample	E_{corr} (mV vs. Ag/AgCl)	I_{corr} ($\mu\text{A}/\text{cm}^2$)	CR ($\mu\text{m}/\text{year}$)	E_b (V vs. Ag/AgCl)
as-printed (rough)	-55.0	0.77	8.22	~ 1.61
as-printed (medium)	-8.7	0.44	4.70	~1.9
as-printed (smooth)	-209.1	0.34	3.63	2.16
heat-treated (rough)	-213.8	0.68	7.16	1.47
heat-treated (medium)	-299.5	0.37	3.89	1.41
heat-treated (smooth)	-147.7	0.21	2.21	2.35
reference (rough)	28.3	0.93	8.29	1.57
reference (medium)	-300.9	0.34	3.03	1.25
reference (smooth)	-80.6	0.27	2.40	1.69

4. Conclusions

The effects of microstructure, surface roughness and surface pores on the corrosion behavior of DMLS (as-printed and heat-treated) and the reference Ti-6Al-4V samples were experimentally investigated. The acicular microstructure in the as-printed and heat-treated samples contributes to lower corrosion rate than the reference sample with $\alpha+\beta$ two-phase structure. The existence of surface pore in the as-printed sample leads to a reduced corrosion resistance under smooth surface finish, and its effect is negligible under rough finish. The electrochemical results indicate that acicular microstructure with less surface pore and lower surface roughness contributes to better corrosion resistance.

Acknowledgment

The assistance from Professor Christopher A. Brown's Surface Metrology Laboratory is gratefully acknowledged.

Reference

1. Parthasarathy, Jayanthi, Binil Starly, and Shivakumar Raman. "A design for the additive manufacture of functionally graded porous structures with tailored mechanical properties for biomedical applications." *Journal of Manufacturing Processes* 13, no. 2 (2011): 160-170.
2. Traini, T., C. Mangano, R. L. Sammons, F. Mangano, A. Macchi, and A. Piattelli. "Direct laser metal sintering as a new approach to fabrication of an isoelastic functionally graded material for manufacture of porous titanium dental implants." *Dental materials* 24, no. 11 (2008): 1525-1533.
3. Niinomi, Mitsuo. "Mechanical properties of biomedical titanium alloys." *Materials Science and Engineering: A* 243, no. 1 (1998): 231-236.
4. Cisse, O., O. Savadogo, M. Wu, and L'H. Yahia. "Effect of surface treatment of NiTi alloy on its corrosion behavior in Hanks' solution." *Journal of biomedical materials research* 61, no. 3 (2002): 339-345.
5. Atwood, Sara A., Eli W. Patten, Kevin J. Bozic, Lisa A. Pruitt, and Michael D. Ries. "Corrosion-induced fracture of a double-modular hip prosthesis." *The Journal of Bone & Joint Surgery* 92, no. 6 (2010): 1522-1525.
6. Vrancken, Bey, Lore Thijs, Jean-Pierre Kruth, and Jan Van Humbeeck. "Heat treatment of Ti6Al4V produced by selective laser melting: microstructure and mechanical properties." *Journal of Alloys and Compounds* 541 (2012): 177-185.
7. Vilaro, Thomas, Christophe Colin, and Jean-Dominique Bartout. "As-fabricated and heat-treated microstructures of the Ti-6Al-4V alloy processed by selective laser melting." *Metallurgical and Materials Transactions A* 42.10 (2011): 3190-3199.
8. Murr, L. E., S. A. Quinones, S. M. Gaytan, M. I. Lopez, A. Rodela, E. Y. Martinez, D. H. Hernandez, E. Martinez, F. Medina, and R. B. Wicker. "Microstructure and mechanical behavior of Ti-6Al-4V produced by rapid-layer manufacturing, for biomedical applications." *Journal of the Mechanical Behavior of Biomedical Materials* 2, no. 1 (2009): 20-32.
9. Brown, Christopher A., William A. Johnsen, and Kevin M. Hult. "Scale-sensitivity, fractal analysis and simulations." *International Journal of Machine Tools and Manufacture* 38.5 (1998): 633-637.

10. Denny, A. Jones. "Principles and prevention of corrosion." Prentice-Hall Inc., Upper Saddle River, NJ (1996): 76-90.
11. ASTM G102-89 (2010). "Standard Practice for Calculation of Corrosion Rates and Related Information from Electrochemical Measurements." (2010).
12. de Damborenea, J. J., M. A. Arenas, Maria Aparecida Larosa, André Luiz Jardini, Cecília Amélia de Carvalho Zavaglia, and A. Conde. "Corrosion of Ti6Al4V pins produced by direct metal laser sintering." *Applied Surface Science* 393 (2017): 340-347.
13. Katarov, I., S. Malinov, and W. Sha. "Finite element modeling of the morphology of β to α phase transformation in Ti-6Al-4V alloy." *Metallurgical and Materials Transactions A* 33.4 (2002): 1027-1040.
14. Lütjering, G. "Influence of processing on microstructure and mechanical properties of (α + β) titanium alloys." *Materials Science and Engineering: A* 243.1 (1998): 32-45.
15. Betts, A.J. and Boulton, L.H., (1993). Crevice corrosion: review of mechanisms, modeling, and mitigation. *British corrosion journal*, 28(4), pp.279-296.
16. Cvijović-Alagić, I., Cvijović, Z., Mitrović, S., Panić, V., & Rakin, M. (2011). Wear and corrosion behaviour of Ti-13Nb-13Zr and Ti-6Al-4V alloys in simulated physiological solution. *Corrosion Science*, 53(2), 796-808.

CHAPTER 4

PAPER II: EFFECT OF ANNEALING TREATMENTS ON THE MICROSTRUCTURE, MECHANICAL PROPERTIES AND CORROSION BEHAVIOR OF DIRECT METAL LASER SINTERED Ti-6Al-4V

Yangzi Xu, Yuan Lu, Kristin L. Sundberg, Jianyu Liang, Richard D. Sisson, Jr.

Accepted by: *Journal of Materials Engineering and Performance*

Highlights:

1. Post-annealing treatments in the $\alpha + \beta$ region can coarse the lath microstructure and reduce internal porosity in the as-printed part. By closing the pores as crack nucleation sites, the elongation of annealed parts have two-fold enhancement.
2. The electrochemical measurements indicate that the as-printed parts with acicular microstructure possess a thicker and more stable oxide film than quiaxed Grade 5 Ti-6Al-4V alloy. The high temperature annealed parts have lower corrosion current density than as-printed parts, and passives up to 2.6 V (vs. Ag/AgCl).

Effect of Annealing Treatments on the Microstructure, Mechanical Properties and Corrosion Behavior of Direct Metal Laser Sintered Ti-6Al-4V

Yangzi Xu, Yuan Lu, Kristin L. Sundberg, Jianyu Liang, and Richard D. Sisson Jr.

(Submitted January 30, 2017; in revised form April 12, 2017)

An experimental investigation on the effects of post-annealing treatments on the microstructure, mechanical properties and corrosion behavior of direct metal laser sintered Ti-6Al-4V alloys has been conducted. The microstructure and phase evolution as affected by annealing treatment temperature were examined through scanning electron microscopy and x-ray diffraction. The tensile properties and Vickers hardness were measured and compared to the commercial Grade 5 Ti-6Al-4V alloy. Corrosion behavior of the parts was analyzed electrochemically in simulated body fluid at 37 °C. It was found out that the as-printed parts mainly composed of non-equilibrium α' phase. Annealing treatment allowed the transformation from α' to α phase and the development of β phase. The tensile test results indicated that post-annealing treatment could improve the ductility and decrease the strength. The as-printed Ti-6Al-4V part exhibits inferior corrosion resistance compared to the commercial alloy, and post-annealing treatment can reduce its susceptibility to corrosion by reducing the two-phase interface area.

Keywords corrosion behavior, direct metal laser sintering, microstructure, tensile test, Ti-6Al-4V

1. Introduction

Additive manufacturing is a process to create parts by the addition of materials layer by layer (Ref 1). Direct metal laser sintering (DMLS) is an additive manufacturing process that can directly build three-dimensional (3D) metallic parts from pre-alloyed powders in accordance with a sliced 3D computer-aided design (CAD) model (Ref 2). This rapid prototyping technique is able to create 3D freeform objects, which makes it especially helpful in biomedical and aerospace applications. The DMLS technique can be used in fabricating titanium and its alloys, which are fully commercialized in orthopedic and dental industry due to their high strength-to-weight ratio, good mechanical properties, corrosion resistance, chemical inertness and biocompatibility (Ref 2). Titanium alloys were first introduced to the orthopedic industry in the 1960s (Ref 3). Since then, pure titanium and Ti-6Al-4V alloy have been widely used in total knee replacement, hip replacement and dental implants (Ref 4). Therefore, a good combination of ductility and fracture toughness is required for titanium alloys because the orthopedic implants, especially hip and knee joints, undergo cyclic loads during daily motion. However, it was found in previous studies that the microstructure of the as-printed Ti-6Al-4V alloy is composed of non-equilibrium martensite phase, which has a negative effect on the tensile and fatigue properties

(Ref 5, 6). Furthermore, defects, including internal pores and unmelt particles, can exist in additively manufactured parts, which also have a considerable influence on the materials properties and may lead to fracture during service (Ref 7).

The microstructural defects can be reduced through optimizing the laser processing conditions, including laser power, scanning speed, building direction, scanning strategy, etc. The effect of processing parameters on the microstructure, porosity and mechanical properties of Ti-6Al-4V alloy fabricated by various laser processing techniques has been investigated by many researchers (Ref 8-11). It was found out that a laser power greater than 90 W and a moderate scanning speed (>0.2 m/s) are needed to get continuous melting, as well as the “layer cross-hatching technique” or zigzag-scanning strategy is essential to achieve higher density and less defects (Ref 8). Although the internal porosity can be reduced to less than 0.1% through altering the processing parameters, the residual porosity is still a remaining issue and the elongation of as-printed parts is still lower than the wrought samples (Ref 8, 11). Therefore, various post-treatments are usually applied on the additively manufactured parts in order to optimize the mechanical properties. Based on ASM heat treatment handbook, annealing treatment in the temperature range of 705 to 790 °C for 3600-14,400 s (1-4 h) is recommended for Ti-6Al-4V alloy for the aim to increase fracture toughness, ductility at room temperature, dimension and thermal stability and creep resistance (Ref 12). Vrancken and coworkers (Ref 5) applied β annealing treatments on the as-printed Ti-6Al-4V parts, and they found an increase of ductility from 7 to 13% and coarsening of the lamellae microstructure. Leuders and coworkers (Ref 13) studied the fatigue properties and crack growth of Ti-6Al-4V alloys fabricated by electron beam melting, and they found out that annealing, in the α region at 800 °C or β region at 1050 °C, and hot isostatic pressing could improve the ductility and fracture toughness by different degrees. They also claimed that post-heat treatment could increase the threshold value for crack growth by a factor of

Yangzi Xu, Yuan Lu, Kristin L. Sundberg, Jianyu Liang, and Richard D. Sisson Jr., Department of Materials Science and Engineering, Worcester Polytechnic Institute, 100 Institute Road, Worcester, MA 01609. Contact e-mail: yxu@wpi.edu.

three, which was due to the reduced tensile residual stress (Ref 13). As far as we know, the microstructure of Ti-6Al-4V alloy is very sensitive to heat treatment temperature, and it can vary within a small temperature range. To the best of the authors' knowledge, the effects of post-annealing treatment temperature (in the range of 705 to 790 °C) on the morphology and tensile properties of Ti-6Al-4V parts fabricated by DMLS have not been well understood.

It was found in many studies that the microstructure of titanium alloys could influence the stability of the oxide layers and therefore affect the corrosion behavior of the parts (Ref 14-16). Since the post-heat treatment of as-printed parts can alter the microstructure, it also influences the impedance of the formed protective oxide layer, which is the key aspect in determining the corrosion behavior. However, only a few investigations concerning the corrosion behavior of additively manufactured Ti-6Al-4V alloy have been conducted, which is important for biomedical applications, and the corrosion behavior under annealing temperature in the range of 705 to 790 °C has not been examined.

Therefore, the aim of this work is to investigate the effects of post-annealing treatments on the microstructure, tensile properties and corrosion behavior of direct metal laser sintered Ti-6Al-4V parts. The post-processing heat treatment parameters are presented in Table 1. These temperatures were selected to encompass the recommended annealing temperatures (Ref 12). These three different annealing temperatures were applied on the as-printed Ti-6Al-4V parts to evaluate the microstructural change and phase evolution. The uniaxial tensile tests were conducted for the mechanical property characterization. The resulting overall fracture surfaces were examined. The corrosion behavior of various heat treatments was measured electrochemically in simulated body fluid, and the effect of annealing temperature was determined.

2. Materials and Methods

2.1 Materials and Sample Preparations

The Ti-6Al-4V pre-alloyed powder particles fabricated by gas atomization were obtained from a commercial supplier and used in this study. The Ti-6Al-4V parts were fabricated by EOS e-Manufacturing Solutions (Krailling, Germany) using direct metal laser sintering (DMLS) technique. Samples were printed at a laser power of 340 W, scanning speed of 1.25 m/s, a hatch spacing (the distance between two adjacent scan vectors) of 1.2×10^{-4} m (120 µm) and a layer thickness of 6×10^{-5} m (60 µm). Layers were scanned using a zigzag-scanning strategy and rotated 90° between each layer. This alternating scanning

Table 1 Post-annealing treatment procedures and sample designations

Sample designation	Temperature, °C	Time, s	Cooling
AP
700HT	700	14,400	Air-cooling
750HT	750	14,400	Air-cooling
799HT	799	14,400	Air-cooling

AP stands for the as-printed Ti-6Al-4V parts

strategy was used to obtain highly dense part. The Ti-6Al-4V parts were printed directly in the shape of tensile testing bars based on ASTM standard as schematically shown in Fig. 1 (the orthogonal coordinate will be further used in this work).

The as-printed samples (designated as AP) were degreased in acetone before annealing treatments in a vacuum furnace under three different temperatures: 700, 750 and 799 °C for 14,400 s (4 h), and followed by air-cooling. The post-annealing treatment procedures and sample designations are listed in Table 1. The AP and annealed samples were cut using an abrasive sectioning machine with SiC blade into cubes with dimension of 0.01 m × 0.01 m × 0.008 m, and mounted by epoxy resin. The mounted specimens were sequentially ground up to 1200-grit silicon carbide paper, followed by final finish with colloidal silica suspension on ChemoMet polishing cloth to achieve a mirror surface. To reveal the microstructure, the polished samples were etched for 30 s using Kroll's reagent (0.002 L HF, 0.005 L HNO₃ and 0.1 L H₂O). Because of the layer-wise building process, the building planes (XZ and YZ planes in Fig. 1) and deposition plane (XY plane in Fig. 1) are considered during metallographic investigation. The hot forged and mill-annealed Ti-6Al-4V (Grade 5) alloy with equiaxed microstructure will be addressed as the reference material in the following discussions.

2.2 Characterization Techniques

A Nikon optical microscope (Nikon Instrument Inc.) was used for examination of the microstructure. A JEOL JSM-7000F scanning electron microscopy (SEM) was used for high magnification characterization of the microstructure. Size distribution of the pre-alloyed powder particles and surface porosity of the bulk samples were analyzed using ImageJ. Crystallography and phase analysis were conducted on a PANanalytical Empyrean 2 x-ray diffractometer (XRD) with Cu-K_α radiation at 45 keV and 40 mA. The XRD measurements were taken over a range of 2θ angle equals 20° to 80° under a step size of 0.05. Phase identifications and Rietveld refinement were carried out using HighScore Plus software (Ref 17, 18). Uniaxial tensile tests were performed on the AP and 799HT samples along X-axis (as indicated in Fig. 1) to determine the stress-strain behavior of the materials. The yield strength and Young's modulus were determined based on ASTM A1011 and ASTM E111, respectively. Four tensile tests were conducted for each condition to determine the mechanical properties. The Vickers hardness measurements were conducted on the as-polished sample surface, and measured with a microhardness tester at a force of 200 gf. The hardness measurements were duplicated for ten measurements on each sample.

2.3 Electrochemical Test

A Cu wire was attached to the back of the tested sample (0.005 m × 0.005 m × 0.008 m) by conductive tape, and the whole part was cold mounted by epoxy resin to expose a flat surface with surface area of 2.5×10^{-5} m² to the electrolyte. The deposition plane (XY plane) was used for each sample during the corrosion tests in this study. Post-curing, the specimens were sequentially ground up to 1200-grit silicon carbide paper, followed by final finish with colloidal silica suspension to achieve mirror surface. The electrochemical measurements were conducted in a three-electrode cell with

Ag/AgCl (3 M NaCl) as the reference electrode, a platinum wire (surface area: $3.6 \times 10^{-4} \text{ m}^2$) as the counter electrode and the polished Ti-6Al-4V sample as the working electrode. All electrode potentials are referred to the reference Ag/AgCl electrode. The volume of the test cell was 0.1 L. Naturally aerated Ringer's solution ($6.5 \times 10^{-3} \text{ kg/L NaCl}$, $1.4 \times 10^{-4} \text{ kg/L KCl}$, $1.2 \times 10^{-4} \text{ kg/L CaCl}_2$, $2 \times 10^{-4} \text{ kg/L NaCO}_3$ and $4 \times 10^{-4} \text{ kg/L glucose}$) was used as the electrolyte and was maintained at 37°C during measurements. A Bio-Logic potentiostat was used to measure the open-circuit potential after immersion of the working electrode into the electrolyte until the potential reached a plateau value and then generated polarization curves. A scan started from -1.0 V

moves anodically at a constant scan rate of 0.001 V/s till $+3.0 \text{ V}$. Bio-Logic® software was used to analyze the electrochemical parameters using Tafel plot. The corrosion measurements were duplicated three times for each sample.

3. Results and Discussion

3.1 Pre-Alloyed Powder Particles

Figure 2(a) depicts the SEM image of the starting pre-alloyed Ti-6Al-4V powder particles. The particles have relatively uniform spherical shape, while some ultrafine particles can be observed.

The ultrafine powder particles with diameter less than $1 \times 10^{-5} \text{ m}$ ($10 \text{ }\mu\text{m}$) can be adhered to larger particles, and they can reduce defects by filling in the gaps between large particles during the sintering process. Figure 2(b) shows the histogram of the particle size distribution and reveals a powder diameter in the range of 1×10^{-5} to $5 \times 10^{-5} \text{ m}$ (10 to $50 \text{ }\mu\text{m}$). The average particle size is $2.7 \times 10^{-5} \pm 6.5 \times 10^{-6} \text{ m}$ ($27 \pm 6.5 \text{ }\mu\text{m}$), and some particles with larger diameter of $3.5 \times 10^{-5} \text{ m}$ (35 microns) also exist. The etched cross section of a medium size Ti-6Al-4V particle shown in Fig. 2(c) reveals a martensitic microstructure. The highlighted area is enlarged in Fig. 2(d), where the bright ultrafine lathes indicate high vanadium concentration regions. Birt et al. (Ref 19) indicated that the hexagonal closed packed (HCP) martensitic lathes and the “feathered” appearance on the edge of lath are likely

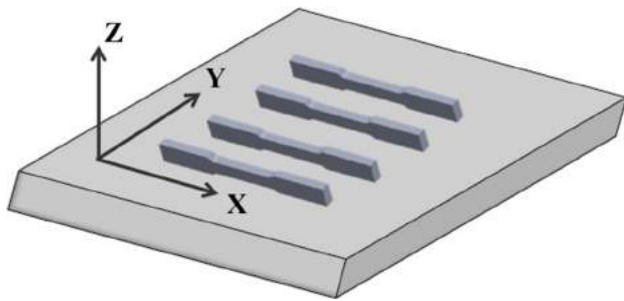


Fig. 1 Schematic diagram of the tensile bars printed using direct metal laser sintering. The orthogonal coordinate system that will be used in this paper are indicated

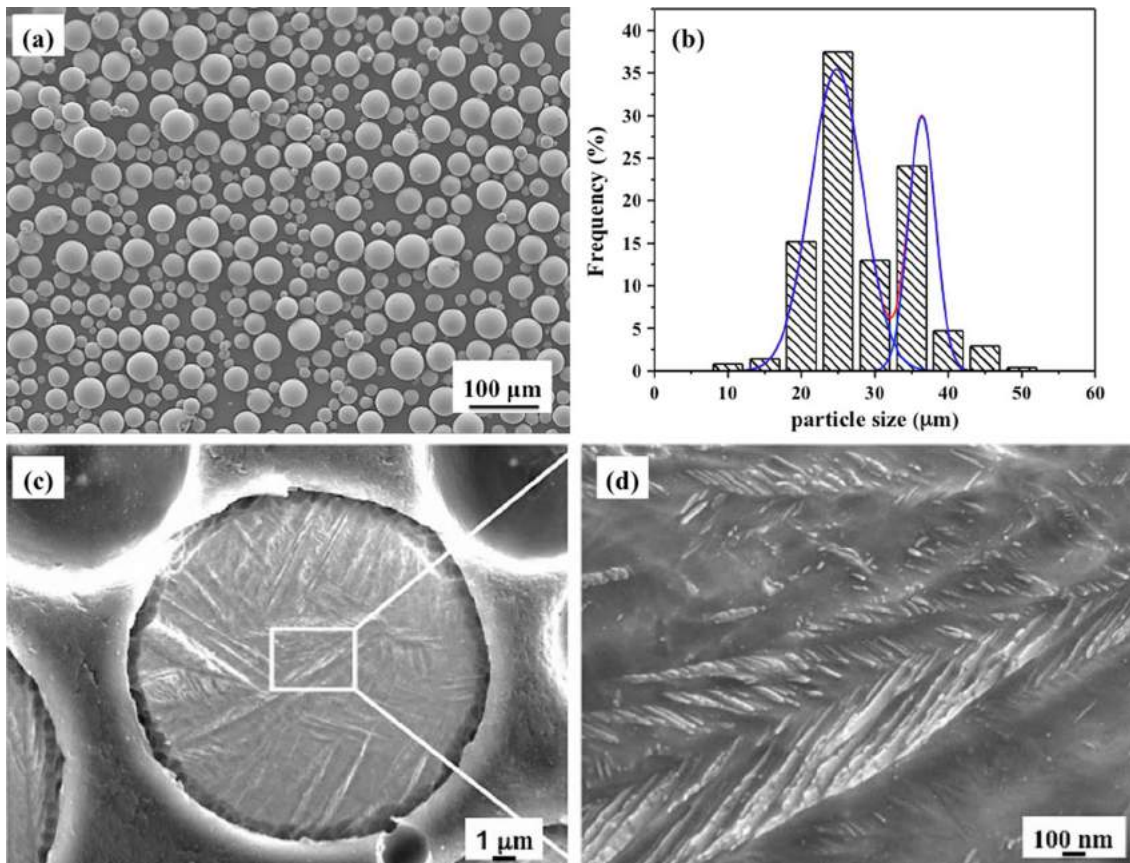


Fig. 2 (a) Morphology of the starting pre-alloyed Ti-6Al-4V powder particles, (b) histogram of the particle size distribution. A bimodal particle size distribution is seen in (a) and (b). (c) Etched cross section of a powder particle, and (d) a fine vanadium-rich lath

formed by diffusion of vanadium out of HCP lattice, this microstructure indicates some level of microsegregation during the atomization of Ti-6Al-4V powder.

3.2 Surface Morphology and Microstructure of As-Printed Ti-6Al-4V Parts

Morphology of the bottom deposition plane (XY plane) in the as-printed part is shown in Fig. 3(a), and the inset schematically shows the studied plane from the tensile bar. The highlighted area is shown in Fig. 3(b) to indicate the remaining scan pattern on the surface. The zigzag scan pattern (pointed out by white arrow) can be clearly seen, and the distance between two adjacent scan vectors is labeled by double-side arrow with dimension of 1.2×10^{-4} m ($120 \mu\text{m}$). Optical image of the top deposition plane (XY plane) of the as-printed part is shown in Fig. 3(c). Different from the morphology shown in Fig. 3(a), the top plane is composed of partially sintered particles and lack of the zigzag sintering pattern. Morphology of the vertical building plane (XZ plane) is shown in Fig. 3(d). Apart from the rough surface caused by partially sintered powder particles, some bright area with scanning lines can be observed.

Due to layer-wise building method and zigzag scanning, the microstructure of deposition and building planes are different. The three-dimensional metallograph of AP is shown in Fig. 4 with the Vickers hardness data of each plane. The deposition plane (XY) has equiaxed grid pattern, which was identified as “chessboard pattern” results from the alternating scanning strategy between layers (Ref 5). The size of the square is comparable to the applied hatch spacing (1.2×10^{-4} m ($120 \mu\text{m}$)). In the micrograph of the building planes (XZ and YZ planes) in Fig. 4, columnar prior β grains with length of a few hundred micrometers delineated by α grain boundaries, which indicates that the thermal gradient exists along the building plane (Ref 20). Vickers hardness of the deposition plane is 451 ± 11 HV, and it is slightly higher than the value of building planes: 431 ± 12 HV for XZ plane and 439 ± 15 HV for YZ plane.

3.3 Microstructure of the Post-Annealed Ti-6Al-4V Parts

The scanning electron microscopy (SEM) images of AP and 799HT at high magnification is shown in Fig. 5(a) and (b), respectively. Different from the commercial Grade 5 alloy, the as-printed part has acicular martensite microstructure. Coars-

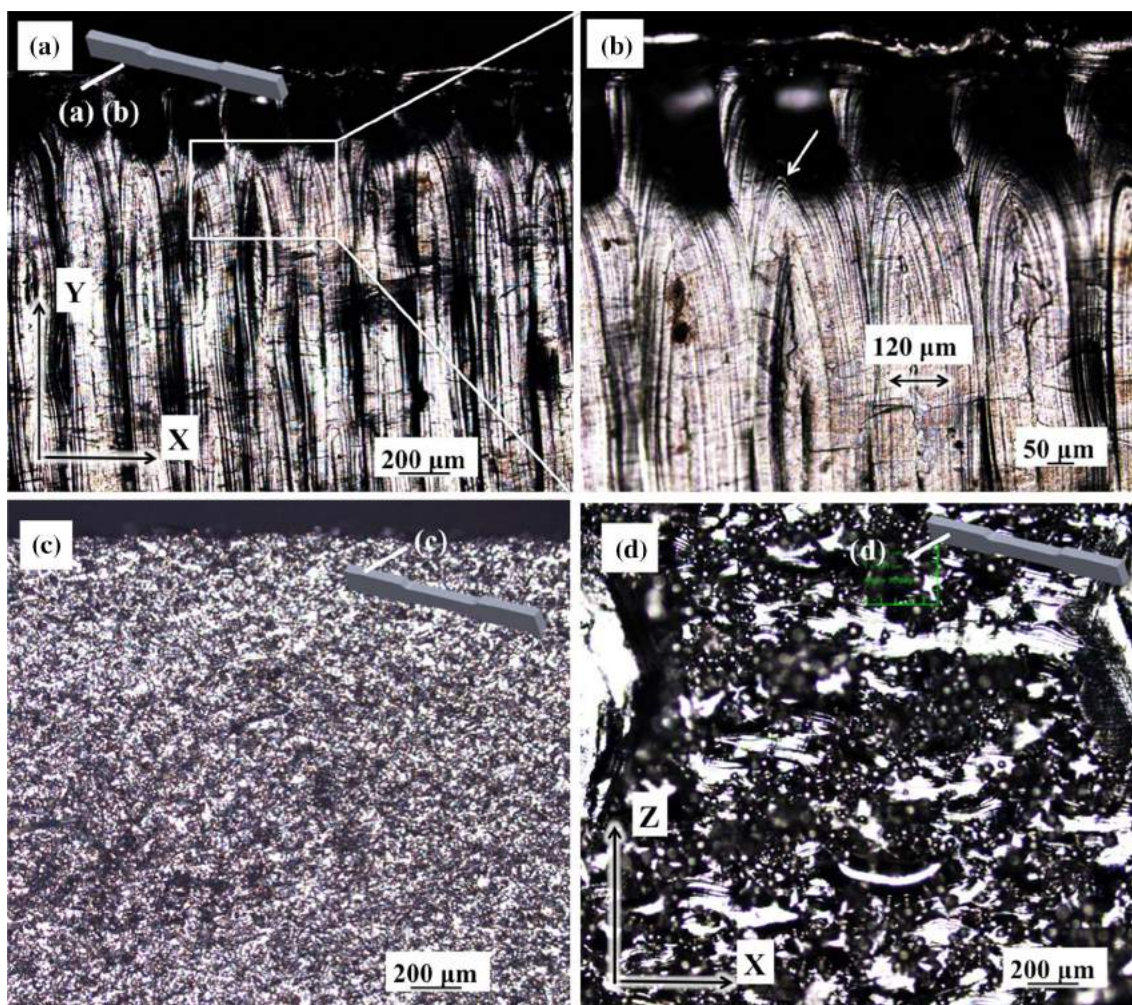


Fig. 3 Confocal microscopy of the different surfaces in the as-printed parts: (a) bottom deposition plane (XY plane) of the tensile bar, (b) highlighted area in (a) showing the corner of zigzag scan pattern (white arrow indicates the changing of scanning direction, and the double-side arrow shows the hatch spacing of approximately $120 \mu\text{m}$), (c) the top deposition plane and (d) building plane (XZ plane) as indicated on the schematic graph of tensile bar

ened microstructure can be observed after post-annealing treatment. Morphology of the surface pores with elongated shape in the 799HT is shown in Fig. 5(c). Based on image analysis, porosity of AP and 799HT parts is 0.29 and 0.074%,

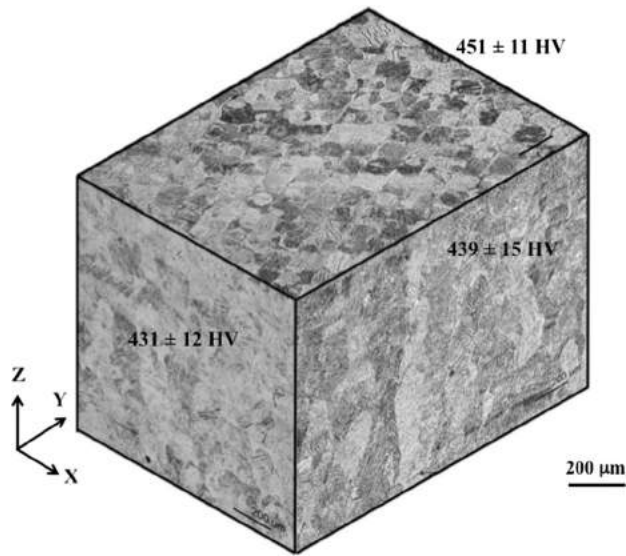


Fig. 4 Three-dimensional metallography of as-printed part with the Vickers hardness results of each plane (the orthogonal coordinate indicates building directions)

respectively. The highlighted area is shown in Fig. 5(d), in which the scanning counters along the edge of elongated pore can be seen, and the microstructure of lower solid layer is revealed.

Apart from the microstructural change in AP parts, another issue of laser processing is the existence of porosity. Commercial Ti-6Al-4V parts are usually treated by hot isostatic pressing to achieve a fully dense material. However, the laser-processed samples usually possess spherical and elongated pores caused by entrapped gas and insufficient sintering, respectively (Ref 11). Post-annealing treatment can decrease the porosity from 0.29 to 0.074%, because some poorly bound particles can be re-sintered during this process. It was claimed by other researchers that porosity has a considerable effect on the mechanical properties, especially tensile and fatigue properties, because the pores can act as crack initiation site and leads to failure (Ref 11, 13). Furthermore, Ti-6Al-4V alloy can experience pitting corrosion under some environments, and the existence of surface pores may deteriorate its pitting corrosion resistance (Ref 7). Although post-annealing treatment can reduce porosity by 75%, the remaining pores still have potential impact on the mechanical properties; therefore, hot isostatic pressing is required to achieve a dense part.

Microstructure of the post-annealed Ti-6Al-4V parts under 700, 750 and 799 °C is shown in Fig. 6(a), (b) and (c), respectively. Coarsened α lath and agglomerated precipitates can be seen under various annealing temperatures. As plotted in Fig. 6(d), the average lath thickness with standard deviation of AP is $3.27 \times 10^{-7} \pm 5.3 \times 10^{-8}$ m (0.327 ± 0.053 μm), which

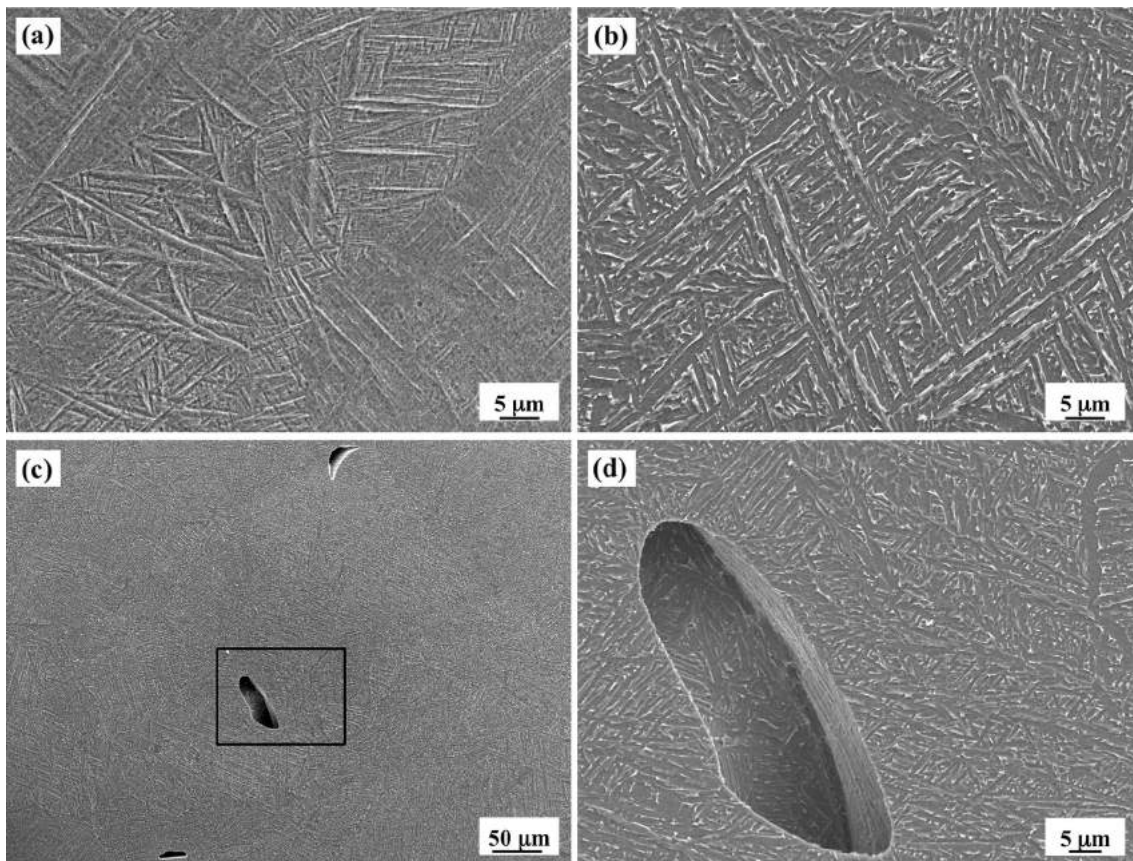


Fig. 5 Scanning electron microscopy images of the deposition plane of (a) as-printed, (b) 799 °C heat-treated Ti-6Al-4V sample, (c) defects with different shapes in the deposition plane of 799 °C heat-treated sample and (d) morphology of the highlighted area in (c)

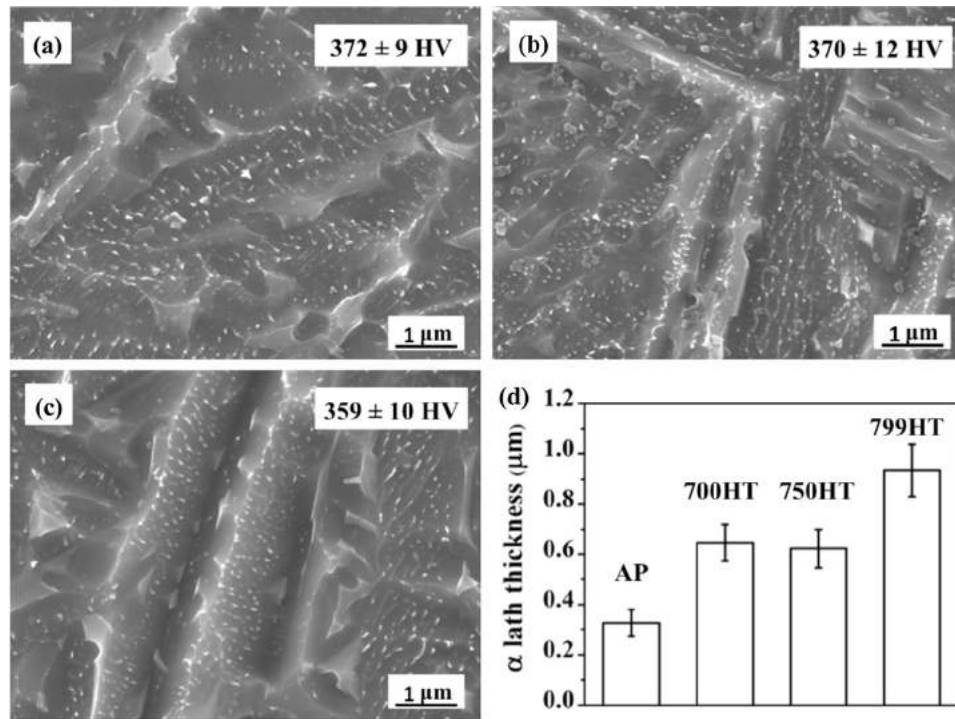


Fig. 6 Microstructure of direct metal laser sintered Ti-6Al-4V parts after annealing at (a) 700 °C, (b) 750 °C and (c) 799 °C. (d) Average lath thickness and standard deviations of the as-printed and post-annealed samples. Vickers hardness results are indicated for each sample on the photomicrograph

increased to $6.47 \times 10^{-7} \pm 7.3 \times 10^{-8}$ m (0.647 ± 0.073 μm) after annealing treatment at 700 °C. At elevated annealing temperature of 799 °C, the average α lath thickness increased significantly to $9.35 \times 10^{-7} \pm 1.04 \times 10^{-7}$ m (0.935 ± 0.104 μm). The Vickers hardness results are also enclosed in the SEM images. Due to the microstructural change, Vickers hardness value has small variation among post-annealed sample, and it decreased from 372 ± 9 HV in 700HT to 359 ± 10 HV in 799HT.

3.4 Phase Analysis and Rietveld Refinement Results

XRD patterns of the AP, 799HT and reference Grade 5 Ti-6Al-4V samples are shown in Fig. 7. The AP sample is composed of Ti- α' HCP phase, which shifts to higher 2θ angles with broadened peaks compared to Ti- α phase (HCP) (Ref 20, 21). Post-annealing treatment allows the development of β phase at 2θ angle equals 39.7° for 799HT. XRD pattern of the reference Grade 5 sample shows higher intensity of the β characteristic peaks, and reduced full width half maximum of both α and β peaks.

The Rietveld refinement results of the investigated samples are summarized in Table 2. The lattice parameters of α' phase are lower than the values of the HCP α titanium ($a = 2.9440 \times 10^{-10}$ m, $c = 4.6780 \times 10^{-10}$ m) due to lattice distortion by the substituted atoms (Ref 22). The aluminum and vanadium atoms with smaller atomic radius are substituted in the HCP α' titanium lattice and lead to smaller lattice parameter of AP sample ($a = 2.9229 \times 10^{-10}$ m, $c = 4.6615 \times 10^{-10}$ m). In the XRD patterns shown in Fig. 7, AP sample has broader α' characteristic peaks than 799HT sample. The full width half maximum (FWHM) of XRD peaks are mainly affected by three factors: (1) instrumental parameters; (2) sample parameters

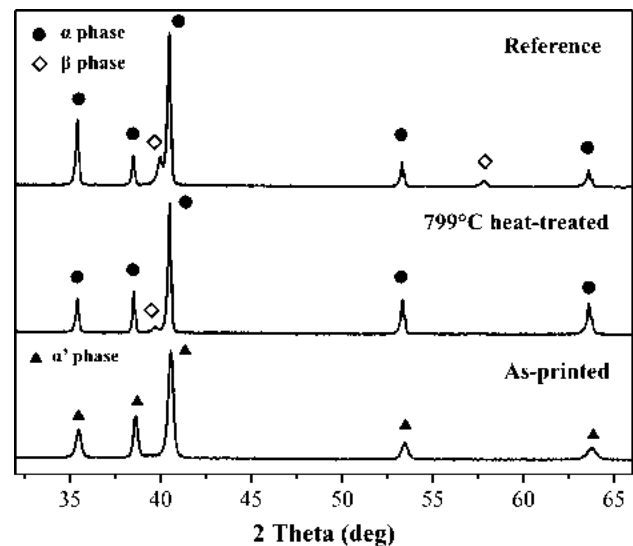


Fig. 7 X-ray diffraction patterns of the as-printed, 799 °C annealed and reference Grade 5 Ti-6Al-4V samples with the phases labeled. The α' phase is only observed in the as-printed samples

such as grain size and microstrain; and (3) crystal structure including crystallinity and defects (Ref 23). Since all the measurements were conducted under same optic configuration, narrowing of characteristic peaks from AP to 799HT sample is likely due to the increased lath thickness (AP: 0.327 ± 0.053 μm ; 799HT: 0.935 ± 0.104 μm) and reduced microstrain. The FWHM of Ti- α' (101) peak for AP sample is 0.307° , and this value decreased to 0.178° for the Ti- α (101) of 799HT sample. The slightly different FWHM value in the reference

Table 2 Rietveld refinement results of the investigated samples

Sample designation	α' , α phase (HCP)				β phase (BCC)		
	a ($\times 10^{-10}$ m)	c ($\times 10^{-10}$ m)	FWHM (110), $^{\circ}$	α phase, %	a ($\times 10^{-10}$ m)	FWHM (101), $^{\circ}$	β phase, %
AP	2.92292 (2)	4.6615 (2)	0.307	97.9	<2.1*
700HT	2.92359 (2)	4.6685 (1)	0.159	93.4	3.2238 (2)	0.2049	6.6
750HT	2.92303 (2)	4.6688 (5)	0.155	91.5	3.2207 (1)	0.2060	8.5
799HT	2.92736 (6)	4.6728 (1)	0.178	90.6	3.2086 (7)	0.2626	9.4
Reference	2.92797 (8)	4.6770 (1)	0.207	80.0	3.19	0.4090	20.0

* Nano-sized β nuclei

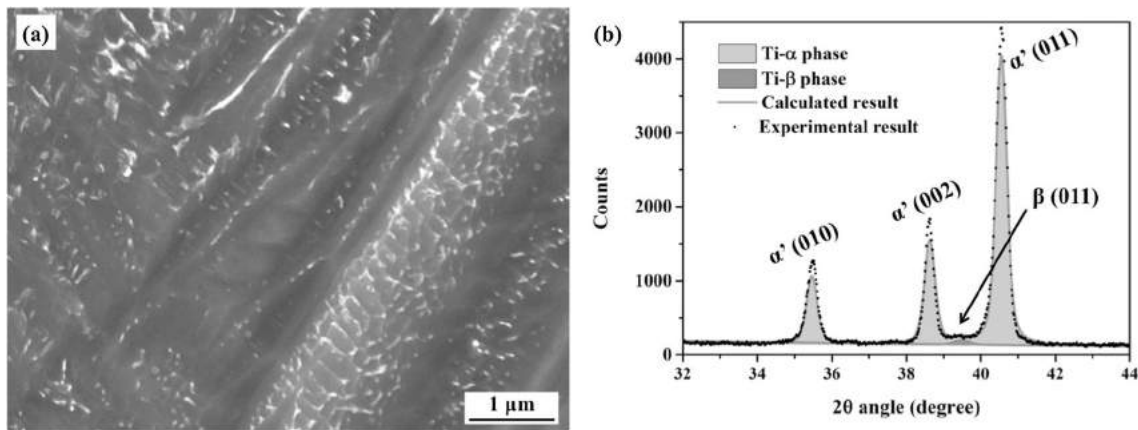


Fig. 8 (a) Magnified view of the acicular microstructure in the as-printed sample shows nano-sized β particles in the α' matrix and (b) refinement result of XRD pattern of as-printed sample indicates small amount of β phase

Table 3 Tensile properties of the investigated samples

Sample designation	σ_{ys} , MPa	UTS, MPa	E, GPa	ϵ_F , %
AP	1056 \pm 20.1	1196 \pm 18.8	105.8 \pm 20.1	7.0 \pm 1.8
799HT	902 \pm 16.2	969 \pm 14.4	94.9 \pm 15.6	11.6 \pm 2.4
Reference	960 \pm 10	1006 \pm 10	120.2 \pm 1.9	18.4 \pm 0.9

The data of reference Grade 5 Ti-6Al-4V are listed for comparison (Ref 5)

Grade 5 sample is due to its equiaxed microstructure. A magnified view of the acicular microstructure in the as-printed sample in Fig. 8(a) shows the dispersion of nano-sized β particles in the α' matrix. With the help of refinement, a broad Ti- β characteristic peak was revealed at 2θ angle equals 39.7° in the as-printed sample (Fig. 8b), which represents the existence of small amount of β phase. The refinement results suggest a β phase with less than 2.1% (Table 2).

3.5 Tensile Properties and Fractography

The tensile test results (yield strength, ultimate tensile strength and elongation) of AP and 799HT samples are summarized in Table 3. Tensile properties of the Grade 5 Ti-6Al-4V alloy are also listed for comparison (Ref 5). The AP samples exhibited the highest yield strength (1056 \pm 20.1 MPa), ultimate tensile strength (1196 \pm 18.8 MPa) and Young's modulus (105.8 \pm 20.1 GPa). Because of the fine martensite microstructure and internal porosity, AP parts possess relatively poor

ductility of 7.0 \pm 1.8%. The 799HT have compensated yield strength (902 \pm 16.2 MPa), ultimate tensile strength (969 \pm 14.4 MPa) and Young's modulus (94.9 \pm 15.6 GPa), but the ductility increased to 11.6 \pm 2.4%. The acicular microstructure and porosity of AP part have considerable influence on its tensile properties. Post-annealing treatment of AP can increase the ductility to nearly twofold with decreased strength and Young's modulus. Based on the ASTM specifications for Ti-6Al-4V alloys used as medical materials, the yield strength and ultimate tensile strength should not suppress 795 and 960 MPa, respectively, and the fracture strain should be greater than 10.0% (Ref 4). Based on the experimental results, the ductility of 799HT can be improved to 11.6 \pm 2.4% which achieves the ASTM limit value for medical materials, but the strength needs to be further reduced. In order to eliminate the stress-shielding effects, the strength and Young's modulus can be controlled by intentionally introducing porosity and lattice structures, which is applicable by using rapid prototyping techniques (Ref 24). Although the ductility of 799HT sample

achieves the ASTM limit value of 10.0%, it is still lower than the reference material of $18.4 \pm 0.9\%$. In AP and 799HT samples, the internal pores can act as crack nucleation site and lead to cleavage fracture around the pores. Therefore, ductility can be further improved by further reducing the internal porosity.

The uniaxial tensile tests were conducted along the X-axis. In Fig. 9(a), the overall post-fracture surface of AP indicates a stair-like and layered morphology. The microscopic voids and dimple structure shown in Fig. 9(b) demonstrate a ductile failure mechanism of the material (Ref 25). Interestingly, a few shell-like craters can be observed within the ductile dimple matrix of AP sample and are shown in Fig. 9(c) and (d). The fractography of 799HT samples is shown in Fig. 10(a) of the YZ plane. It possesses relatively smooth topography compared to the morphology of AP, and the equiaxed dimples feature indicates ductile failure. The highlighted region in Fig. 10(a) is enlarged in Fig. 10(b) indicates a localized pore-induced fracture. In Fig. 10(b), the hollow arrow refers to the overload direction during tensile test, and the short arrows point out the scanning contours during DMLS. The shell-like crater shown in Fig. 9(c) and (d) is absent in the 799HT parts. Since the uniaxial tensile tests were conducted along X-axis in Fig. 1, so the shell-like features are on the building plane and are unlikely caused by layered sintering. Noticed the acicular features in the craters, they may be caused by pulling out the loosely bound powder particles during tensile testing. The dimension of the shell-like craters is comparable to the starting Ti-6Al-4V particle size of around 2.7×10^{-5} m (27 μ m). After post-

annealing treatment, this feature is absent probably because the loosely bound particles were re-sintered by this treatment.

3.6 Corrosion Behavior

Ti-6Al-4V implant materials are being used in biological environment, so a good corrosion and wear resistance are critical to maintain its functionality during service. The open-circuit potential (E_{oc}) as a function of immersion time of AP, 799HT and reference Grade 5 samples are shown in Fig. 11(a). After immersion, the open-circuit potential of all the investigated samples shifted to the noble side after contacting with Ringer's solution, and this behavior suggests the formation of a protective TiO_2 layer (1×10^{-9} to 4×10^{-9} m) on the surface (Ref 21, 26). The thickness of the protective layer increased gradually until the E_{oc} reached a steady state. The E_{oc} of 799HT and reference samples have almost reached steady state after 14,400 s (4 h), but the E_{oc} of AP continuously increased till 25,200 s (7 h). The E_{oc} values listed in Table 4 were recorded after the potential reached steady states. AP and 799HT show a slightly nobler E_{oc} than the reference sample, which is an indication of more stable protective film (Ref 21). Some studies found that the protective film on titanium alloys consists of two layers: the dense inner layer (mainly TiO_2) and porous outer layer (other alloying element oxides) (Ref 13). The corrosion resistance of Ti alloys is mainly contributed by the dense inner layer, which has higher resistance (Ref 26). Therefore, composition and thickness of the formed protective layer on Ti alloy play a crucial role on its corrosion behavior.

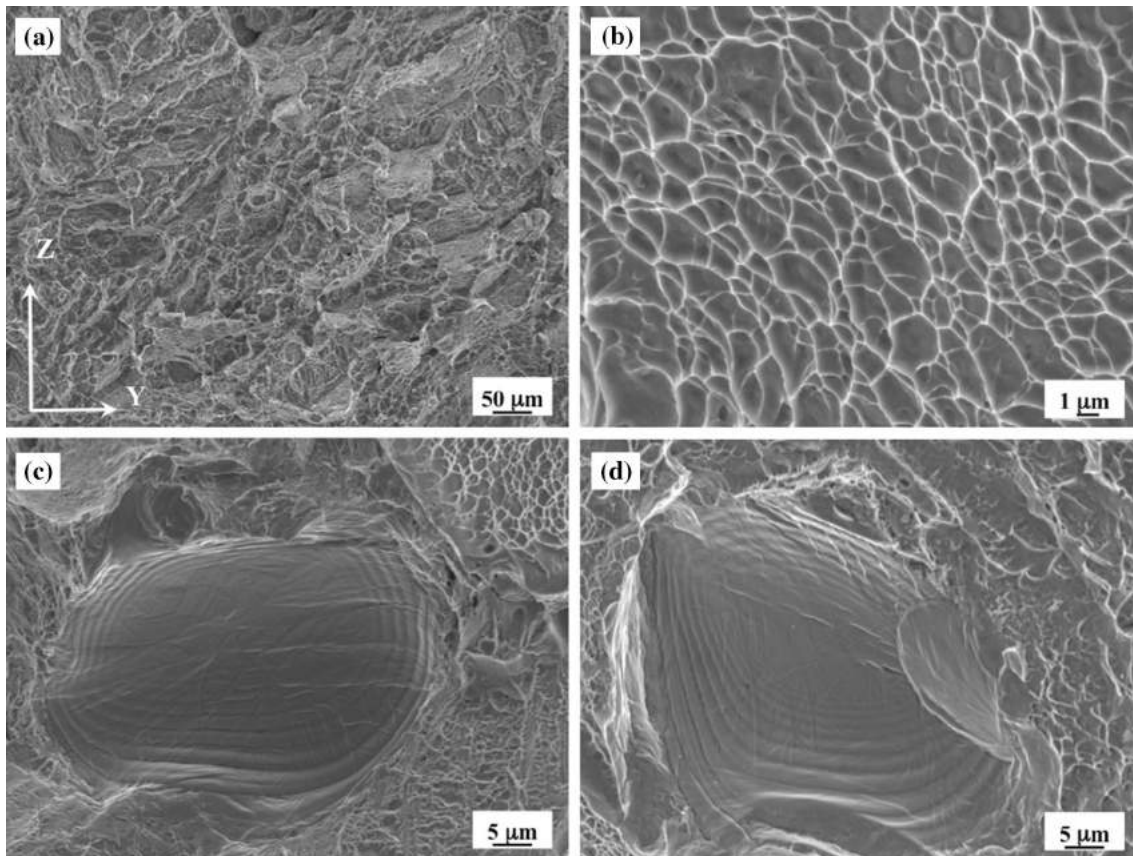


Fig. 9 Fractography of the peripheral area in the as-printed samples (a) at low magnification displaying ductile rupture with some cleavage, (b) magnified view shows the microscopic voids and dimples, (c) and (d) indicate shell-like craters on the fracture surface

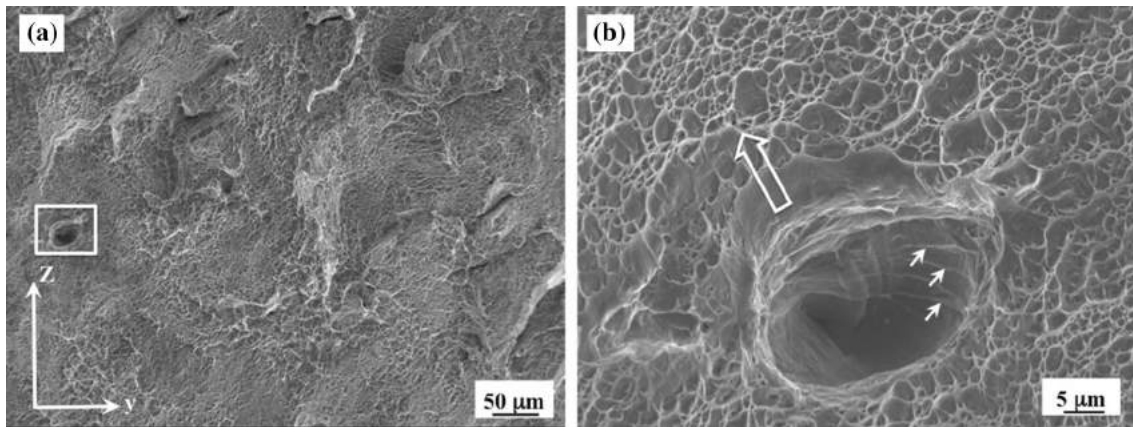


Fig. 10 Fractography of the 799 °C annealed samples, (a) fracture surface displaying ductile rupture, (b) the highlighted region in (a) presenting pore-induced cleavage fracture indicated by the large arrow, the shorter arrows show the deposition layers in the pore

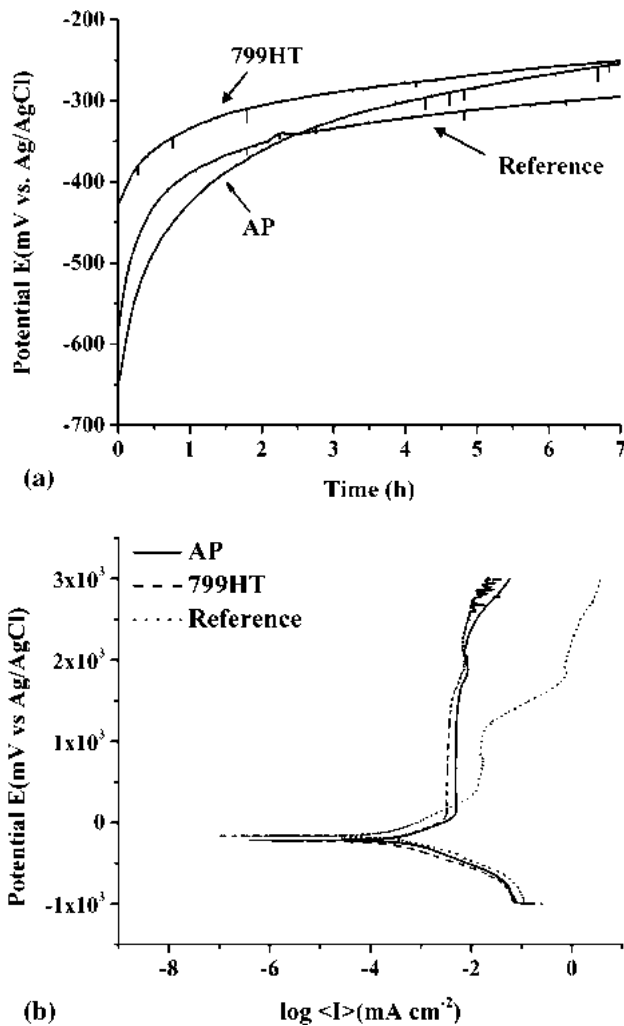


Fig. 11 (a) Open-circuit potential vs. time curves, and (b) polarization curves of the as-printed, 799 °C annealed and the reference Grade 5 Ti-6Al-4V samples measured in Ringer's solution at 37 °C

Figure 11(b) shows the cyclic polarization plot of the AP, 799HT and reference Grade 5 samples in Ringer's solution at 37 °C. All the curves present the same features: (1) the anodic

current density increases with increasing potential and (2) the current density remains constant with further increasing of potential until breakdown of the oxides film. As shown in Fig. 11(b), the protective films of AP and 799HT did not breakdown up to 2.4 V, whereas the reference sample shows a breakdown potential of 1.2 V. This behavior can attribute to the microstructural difference. For materials with passive film, at potential higher than the breakdown potential, there is a higher tendency to form pits. The breakdown potential depends on the stability of the passive film. It was reported that the reference Grade 5 sample with ($\alpha + \beta$) microstructure possesses double-layer oxide films: an inner dense film mainly consists of titanium oxide, and an outer porous film of Al_2O_3 and V_2O_5 based on the analysis from electrochemical impedance results (Ref 14). The porous layer has high tendency of dissolution, and this will generate oxygen vacancies for further corrosion process, while the acicular martensite microstructure with less solute partitioning will have a more stable oxide film. So the reference Grade 5 sample has low breakdown potential and high E_{corr} .

The electrochemical parameters deduced from Tafel plot are shown in Table 4. The experimental results of the reference Grade 5 sample are also listed for comparison. Corrosion potential (E_{corr}) is an indicator of the stability of the surface condition, and corrosion current density (I_{corr}) illustrates the amount of material will be lost during corrosion reaction (Ref 27). It was widely accepted that the relative position of E_{corr} and E_{op} can provide information of a general thermodynamic corrosion tendency of an electrochemical system (Ref 28). If E_{corr} is more positive than E_{op} , the electrochemical system will have a tendency for slow corrosion process (Ref 28). In Table 4, the reference Grade 5 and as-printed sample have E_{corr} values more positive than E_{op} , which means the electrochemical system have the tendency for corrosion process. After post-annealing treatment at 799 °C, the E_{corr} value is close to E_{op} which means the electrochemical system reaches an equilibrium state and indicates less possibility for corrosion process (Ref 28, 29). The E_{corr} values exhibit less variation among the investigated samples, indicating a relatively consistent surface treatment. AP sample has the highest I_{corr} of $0.384 \times 10^{-2} \text{ A m}^{-2}$ than annealed and reference samples, and 799HT possesses smallest I_{corr} of $0.202 \times 10^{-2} \text{ A m}^{-2}$. A higher I_{corr} in AP suggests that it has a higher tendency to corrosion reaction. Based on the aforementioned SEM and phase identification

Table 4 Electrochemical parameters for the investigated samples deduced from open-circuit potential and polarization tests

Sample designation	E_{oc} (V vs. Ag/AgCl)	E_{corr} (V vs. Ag/AgCl)	I_{corr} ($\times 10^{-2}$ A m $^{-2}$)
AP	-0.25	-0.20	0.384
700HT	-0.27	-0.19	0.305
750HT	-0.24	-0.18	0.295
799HT	-0.25	-0.23	0.202
Reference	-0.29	-0.16	0.270

results, the short interaction during DMLS restricts alloying element partitioning in AP samples and formed martensite α' phase. Annealing treatment allowed the transformation from α' to $\alpha + \beta$ precipitates. The β precipitates agglomerated with increasing post-annealing temperature, therefore, reducing the α/β interface areas that are vulnerable sites to corrosion and improved the corrosion behavior (Ref 30).

The electrochemical test results indicate the AP and annealed samples (acicular) possess nobler open-circuit potential than the reference material (equiaxed), which is related to their microstructural difference. It was reported that the oxides formed by alloying elements will appear as discrete clusters embedded in Ti matrix (Ref 14). AP parts experienced very limited alloy element partitioning during laser processing, so it has acicular α' phase with alloying atoms (Al, V) substituted in the HCP lattice. The reference material has equiaxed microstructure with 80.0% α phase and 20.0% β phase. It has Al and V that stabilizes α and β phases, respectively. Therefore, apart from dense TiO₂ layer, a porous layer contains Al₂O₃ and V₂O₅ can be developed on the surface of the reference sample. The high corrosion current density of as-printed sample is due to the metastable α' phase, and the formation of numerous micro-galvanic cells between α' matrix and nano-sized β nuclei, because the α/β interface will be vulnerable to corrosion reaction (Ref 30). High-temperature annealing facilitates the development and cluster of β phase, which reduced the overall α/β interface area, so 799HT sample has an improved corrosion resistance.

4. Conclusions

In conclusion, the effect of post-annealing treatment on phase transformation, mechanical properties and corrosion behavior of DMLS Ti-6Al-4 V samples was examined. High-temperature annealing coarsened the acicular microstructure and reduced internal porosity. It allows the development of β phase up to 9.4% and more isotropic properties of the part. In particular, the following findings are highlighted:

1. Post-annealing treatment is able to re-sinter loosely bound powder particles and reduces internal porosity. By reducing the internal pore as crack nucleation site, the uniaxial tensile properties in annealed parts can be improved. The ductility was improved to nearly twofold with reduced strength.
2. Laser-processed parts with acicular microstructure have more stable oxides film than equiaxed reference Ti-6Al-4V alloy due to less alloying element partitioning,

whereas, the metastable α' phase (caused by fast cooling) in AP makes it kinetically more vulnerable to corrosion reaction. Annealing treatment at elevated temperature reduces α/β interface areas by agglomerating β precipitates and improves the corrosion resistance.

References

1. J. Parthasarathy, B. Starly, and S. Raman, A Design for the Additive Manufacture of Functionally Graded Porous Structures with Tailored Mechanical Properties for Biomedical Applications, *J. Manuf. Process.*, 2011, **13**(2), p 160–170
2. T. Traini, C. Mangano, R.L. Sammons, F. Mangano, A. Macchi, and A. Piattelli, Direct Laser Metal Sintering as a New Approach to Fabrication of an Isoelastic Functionally Graded Material for Manufacture of Porous Titanium Dental Implants, *Dent. Mater.*, 2008, **24**(11), p 1525–1533
3. D.C. Hansen, Metal Corrosion in the Human Body: The Ultimate Bio-Corrosion Scenario, *Electrochem. Soc. Interface*, 2008, **17**(2), p 31
4. M. Niinomi, Mechanical Properties of Biomedical Titanium Alloys, *Mater. Sci. Eng. A*, 1998, **243**(1), p 231–236
5. B. Vrancken, L. Thijs, J.P. Kruth, and J. Van Humbeeck, Heat Treatment of Ti6Al4V Produced by Selective Laser Melting: Microstructure and Mechanical Properties, *J. Alloy. Compd.*, 2012, **541**, p 177–185
6. L. Thijs, F. Verhaeghe, T. Craeghe, J. Van Humbeeck, and J.P. Kruth, A Study of the Microstructural Evolution During Selective Laser Melting of Ti-6Al-4V, *Acta Mater.*, 2010, **58**(9), p 3303–3312
7. J.J. de Damborenea et al., Corrosion of Ti6Al4V Pins Produced by Direct Metal Laser Sintering, *Appl. Surf. Sci.*, 2017, **393**, p 340–347
8. B. Song, S. Dong, B. Zhang, H. Liao, and C. Coddet, Effects of Processing Parameters on Microstructure and Mechanical Property of Selective Laser Melted Ti6Al4V, *Mater. Des.*, 2012, **35**, p 120–125
9. X. Wu, J. Liang, J. Mei, C. Mitchell, P.S. Goodwin, and W. Voice, Microstructures of Laser-Deposited Ti-6Al-4V, *Mater. Des.*, 2004, **25**(2), p 137–144
10. R. Wauthle et al., Effects of Build Orientation and Heat Treatment on the Microstructure and Mechanical Properties of Selective Laser Melted Ti6Al4V Lattice Structures, *Addit. Manuf.*, 2015, **5**, p 77–84
11. H. Galarraga et al., Effects of the Microstructure and Porosity on Properties of Ti-6Al-4V ELI, Alloy Fabricated by Electron Beam Melting (EBM), *Addit. Manuf.*, 2016, **10**, p 47–57
12. A.S.M. Handbook, Heat Treating, vol. 4.” *ASM International, Materials Park, OH*, 1991, p. 860
13. S. Leuders et al., On the Mechanical Behaviour of Titanium Alloy TiAl6V4 Manufactured by Selective Laser Melting: Fatigue Resistance and Crack Growth Performance, *Int. J. Fatigue*, 2013, **48**, p 300–307
14. I. Cvijović-Alagić, Z. Cvijović, S. Mitrović, V. Panić, and M. Rakin, Wear and Corrosion Behaviour of Ti-13Nb-13Zr and Ti-6Al-4V Alloys in Simulated Physiological Solution, *Corros. Sci.*, 2011, **53**(2), p 796–808
15. M. Geetha, U.K. Mudali, A.K. Gogia, R. Asokamani, and B. Raj, Influence of Microstructure and Alloying Elements on Corrosion Behavior of Ti-13Nb-13Zr Alloy, *Corros. Sci.*, 2004, **46**(4), p 877–892
16. A.K. Shukla, R. Balasubramaniam, and S. Bhargava, Properties of Passive Film Formed on CP Titanium, Ti-6Al-4V and Ti-13.4 Al-29Nb Alloys in Simulated Human Body Conditions, *Intermetallics*, 2005, **13**(6), p 631–637
17. H.M. Rietveld, A Profile Refinement Method for Nuclear and Magnetic Structures, *J. Appl. Crystallogr.*, 1969, **2**(2), p 65–71
18. H.M. Rietveld, Line Profiles of Neutron Powder-Diffraction Peaks for Structure Refinement, *Acta Crystallogr. A*, 1967, **22**(1), p 151–152
19. A.M. Birt, V.K. Champagne, R.D. Sisson, and D. Apelian, Microstructural Analysis of Ti-6Al-4V Powder for Cold Gas Dynamic Spray Application, *Adv. Powder Technol.*, 2015, **26**(5), p 1335–1347
20. S. Al-Bermani, S.S. Al-Bermani, M.L. Blackmore, W. Zhang, and I. Todd, The Origin of Microstructural Diversity, Texture, and Mechanical Properties in Electron Beam Melted Ti-6Al-4V, *Metall. Mater. Trans.*, 2010, **41**(13), p 3422–3434

21. L. Zeng and T.R. Bieler, Effects of Working, Heat Treatment, and Aging on Microstructural Evolution and Crystallographic Texture of α , α' , α'' and β Phases in Ti-6Al-4V Wire, *Mater. Sci. Eng. A*, 2005, **392**(1), p 403–414
22. W. Rostoker, Observations on the Lattice Parameters of the Alpha and TiO Phases in the Titanium-Oxygen System. *J. Met. Trans. AIME*, 1952, **4**(9), p 981–982
23. S.S. Babu, E.D. Specht, S.A. David, E. Karapetrova, P. Zschack, M. Peet, and H.K.D.H. Bhadeshia, In-Situ Observations of Lattice Parameter Fluctuations in Austenite and Transformation to Bainite, *Metall. Mater. Trans. A*, 2005, **36**(12), p 3281–3289
24. L.E. Murr, S.A. Quinones, S.M. Gaytan, M.I. Lopez, A. Rodela, E.Y. Martinez, D.H. Hernandez, E. Martinez, F. Medina, and R.B. Wicker, Microstructure and Mechanical Behavior of Ti-6Al-4V Produced by Rapid-Layer Manufacturing, for Biomedical Applications, *J. Mech. Behav. Biomed. Mater.*, 2009, **2**(1), p 20–32
25. H.K. Rafi, T.L. Starr, and B.E. Stucker, A Comparison of the Tensile, Fatigue, and Fracture Behavior of Ti-6Al-4V and 15–5 PH Stainless Steel Parts Made by Selective Laser Melting, *Int. J. Adv. Manuf. Technol.*, 2013, **69**(5–8), p 1299–1309
26. V.A. Alves, R.Q. Reis, I.C.B. Santos, D.G. Souza, T.D.F. Goncalves, M.A. Pereira-da-Silva, A. Rossi, and L.A. Da Silva, In Situ Impedance Spectroscopy Study of the Electrochemical Corrosion of Ti and Ti-6Al-4V in Simulated Body Fluid at 25 C and 37 C, *Corros. Sci.*, 2009, **51**(10), p 2473–2482
27. O. Cisse, O. Savadogo, M. Wu, and L.H. Yahia, Effect of Surface Treatment of NiTi Alloy on Its Corrosion Behavior in Hanks' Solution, *J. Biomed. Mater. Res.*, 2002, **61**(3), p 339–345
28. Skotheim, T.A., ed. *Handbook of Conducting Polymers*. CRC Press, New York, 1997, pp. 894–895
29. D.A. Jones, *Principles and Prevention of Corrosion*, Macmillan, London, 1992, p 143–162
30. C.Y. Yu, L.X. Yang, C.C. Shen, B. Luan, and T.P. Perng, Corrosion Behavior of Thermohydrogen Processed Ti6Al4V, *Scripta Mater.*, 2007, **56**(12), p 1019–1022

CHAPTER 5

PAPER III: EFFECT OF POST-HEAT TREATMENT PROCESSING ON THE MICROSTRUCTURE AND CORROSION BEHAVIOR OF DIRECT METAL LASER SINTERED Ti-6Al-4V

Yangzi Xu, Yuan Lu, Jianyu Liang, Richard D. Sisson, Jr.

Submitted to: *Materials and Corrosion* (Manuscript form)

Highlights:

1. Decomposition of α' phase to α and β phase took place during heat treatments of the direct metal laser sintered Ti-6Al-4V samples, with coarsening of α lath and agglomerate of β precipitates. Different degrees of relieve in residual stress was achieved after post heat treatments.
2. A single passive layer was observed in the as-printed and low temperature stress relieved sample due to limit solute element partitioning. Double passive layer could be developed in 650SR, 950STA and 1050STA with enhanced resistance of the titanium oxide passive layer. Enhanced resistance of the passive oxide layers was observed in the solution treatment and aged and high temperature stress relieved samples.

Effect of Post-Heat Treatment Processing on the Microstructure and Corrosion Behavior of Direct Metal Laser Sintered Ti-6Al-4V

Yangzi Xu^{1*}, Yuan Lu¹, Jianyu Liang¹, Richard D. Sisson¹

¹ Materials Science and Engineering Department, Worcester Polytechnic Institute, 100 Institute Road, Worcester, MA 01609, USA

Abstract

In this paper, the results of an experimental investigation on the effect of solution treatment and age and stress relieve treatments on the corrosion behavior of direct metal laser sintered Ti-6Al-4V are presented. The microstructural change and phase evolution as affected by heat treatment temperature was characterized through scanning electron microscopy and X-ray diffraction. The corrosion behavior was evaluated electrochemically in Ringer's solution at 37°C. It was determined that the non-equilibrium α' phase with small amount of β nuclei formed in the as-printed sample. Enhancement in the resistance of passive oxide layer on the alloy was observed after solution treatment and age as well as high temperature stress relieve treatments. The structure of surface passive layer showed a heat treatment temperature dependency.

Keywords

Ti-6Al-4V; direct metal laser sintering; microstructure; solution treatment and age; stress relieve; corrosion behavior

* Corresponding author at: Worcester Polytechnic Institute, Materials Science and Engineering Department. Tel: +1 508 831 8333

E-mail address: yxu@wpi.edu (Y. Xu)

1. Introduction

Titanium and its alloys have been used as biomedical implants for decades because of their high strength to weight ratio, good biocompatibility, lack of allergic problems and good corrosion resistance.^[1] Ti-6Al-4V alloy possesses good mechanical properties, good heat treatability, and excellent corrosion resistance by forming titanium oxide passive layer of 1-4 nm on the surface.^[2-4] Therefore, it is widely used as the tibial components in total knee arthroplasty and hip cup in total hip replacement.^[5] However, the released metallic particles in the surrounding tissues by fretting corrosion or pitting corrosion may lead to the failure of the implants and revision surgery.^[6]

In the past decades, the rapid developments in additive manufacturing have broadened their applications in biomedical area due to its high geometrical freedom in fabricating customized implants. Direct metal laser sintering (DMLS) is an additive manufacturing technique.^[7] Due to high localized thermal input and fast cooling rate, it was reported that the as-printed materials result in non-equilibrium phase distribution with high residual stresses.^[8] It was reported that porosity and surface defects are also common problems in the as-printed parts,^{[7][8]} and can significantly impact the mechanical performance (especially tensile and fatigue behavior) by acting as crack nucleation sites.^[9] Significant efforts have been put in enhancing the mechanical properties of the additively manufactured part by optimizing the additive manufacturing processes or applying various post-heat treatments. Hollander and co-workers updated that the elongation at fracture can be increased up to two-fold after post-annealing treatment.^[10] Leuders and co-workers reported that the fatigue strength can be enhanced by reducing the micron sized pores through hot isostatic pressing and heat treatments.^[11] They also observed microstructural change after various post-treatments. The microstructure in the sample can affect the quantity of defects and composition of the oxide layer formed on the surface. The oxide layer plays an important role in the corrosion behavior of titanium alloy.^[3] However, to the best of the authors' knowledge, the effect of various post-heat treatments on the corrosion behavior of DMLS Ti-6Al-4V has not been well studied. In this work, solution treatment and age and stress relieve treatments were conducted on the as-printed samples. The effects of heat treatment temperatures on the microstructure and phase evolution were examined by scanning electron microscopy (SEM) and X-ray diffraction (XRD). The corrosion behavior was analyzed through electrochemical impedance spectroscopy and polarization measurements in Ringer's solution at

37°C.

2. Materials and methods

2.1 Materials and sample preparation

The Ti-6Al-4V parts were fabricated by EOS e-Manufacturing Solutions (Krailing, Germany) using direct metal laser sintering (DMLS) technique. Samples were printed at a scanning speed of 1250 mm/s, a laser power of 340 W, a hatch spacing (the distance between two adjacent scan vectors) of 120 μm and a layer thickness of 60 μm . An alternative scanning strategy was applied to ensure high density parts. During printing, the building plane was referred to XY plane, and the building direction was designated as Z direction.

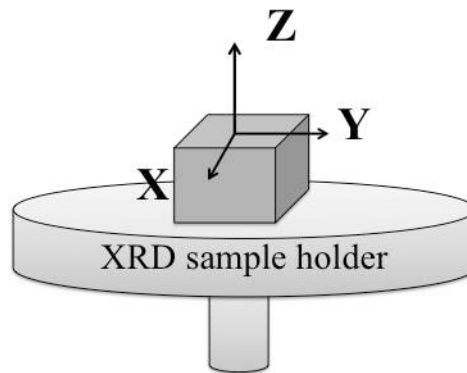


Figure 1: Schematic diagram indicates the sample position during residual stress measurement. The stress values are referred to the X and Y directions located on the sample surface.

The as-printed samples were degreased in acetone before heat treatment and further study. Based on the ASM heat treating handbook, two types of commonly used heat treatments were applied on the as-printed samples: solution treatment and age (designated as STA) and stress relieve treatment (designated as SR) in order to increase strength and reduce residual stress developed during fabrication, respectively.^[12] The heat treatment procedures are listed in Table 1. Solution treatments were conducted in the $\alpha+\beta$ (950°C) and β (1050°C) phase regions for 1 hr, and subsequently aged at 550°C for 4 hr. Stress relieve treatments were applied at three different temperatures in the $\alpha+\beta$ region: 450°C, 550°C and 650°C. The as-printed and heat-treated samples were cut using an abrasive sectioning machine with silicon carbide blade and mounted by epoxy resin. The mounted samples were sequentially ground to 1200 grit silicon carbide paper, followed by final finish with colloidal silica suspension on ChemoMet polishing cloth to

achieve a mirror finish. Microstructures were revealed by etching in the Kroll's reagent (2 ml hydrofluoric acid, 5 ml nitric acid and 100 ml deionized water) for 30 s. The building plane and deposition plane (the plane perpendicular to the building direction) were characterized by metallography due to the layer-wise manufacturing process.

Table 1: Heat treatment conditions of the as-printed samples.

Sample designation	Temperature (°C)	Time (hr)	Cooling method*
950STA	950	1	WQ
	550	4	AC
1050STA	1050	1	WQ
	550	4	AC
450SR	450	4	AC
550SR	550	4	AC
650SR	650	4	AC

* WQ: water quench; AC: air-cooling

2.2 Characterization techniques

The metallographic analysis was conducted on a Nikon optical microscope. A JEOL JSM-7000F scanning electron microscope (SEM) was used to evaluate the microstructure at higher magnification. Phase identifications were conducted on a PANalytical Empyrean 2 X-ray diffractometer with Cu-K α radiation at 45 keV and 40 mA. Rietveld refinement was used to analyze the XRD results.^{[12][14]} Residual stress was measured using $\sin^2\Psi$ method on the X-ray diffractometer,^[15] and the (213) plane peak of α phase at a 2θ of 142° was selected to analyze the results. The sample location is schematically shown in Figure 1. The average lath thickness of as-printed and heat-treated samples were estimated using ImageJ software by selecting 10 duplicate regions.

2.3 Electrochemical measurements

A three-electrode electrochemical cell was used to conduct the electrochemical measurements of as-printed and various heat-treated samples. An Ag/AgCl (3M sodium chloride) and a Platinum wire (surface area: 3.6 cm^2) was used as the reference and auxiliary electrode, respectively. The tested metallic parts were served as working electrode. A Copper wire was attached to the back of the tested sample by conductive tape, then epoxy resin was used to mount the whole device

and exposed a surface area of 0.25 cm². After curing, the working electrode was prepared in the same manner as metallographic samples, and ultrasonically cleaned by acetone. Naturally aerated Ringer's solution (6.5 g/l sodium chloride, 0.14 g/l potassium chloride, 0.2 g/l sodium bicarbonate, 0.12 g/l calcium chloride and 0.4 g/l glucose) was used as the electrolyte and was maintained at 37°C throughout the measurements. Potentiostat (Bio-Logic, Inc.) was used to measure the open circuit potential after immersion the working electrode into the electrolyte. Electrochemical impedance spectra (EIS) were measured at a frequency range of 100 kHz to 10 mHz with the perturbation amplitude of 10 mV after the open circuit potential reached a plateau value. Subsequently, polarization curves were obtained at a scanning rate of 1 mV/s from -1000 mV to +3000 mV. The Bio-Logic software was used to analyze the electrochemical parameters. All reported electrode potentials were referred to the Ag/AgCl reference electrode.

3. Results and discussion

3.1 As-printed samples

The optical micrographs of as-printed sample in planes perpendicular and parallel to the building direction (*Z* axis) are shown in Figure 2(a) and 2(b), respectively. Equiaxed grid pattern can be observed on the deposition plane in Figure 2(a), and this kind of pattern was reported as “chessboard pattern” caused by alternative scanning strategy between layers.^[8] The size of the square is comparable to the hatch spacing of 120 μm applied during DMLS. This alternative scanning strategy was reported to be able to generate more dense part with lower porosity.^[16] In the micrograph of the building plane shown in Figure 2(b), elongated grains with the length of a few hundred micrometers can be observed, which indicates that the heat transfer direction was along the building plane. In Figure 2(b), some short grains with length of 80 μm are comparable to the layer thickness during DMLS, so they are likely caused by the rapid cooling between layers.

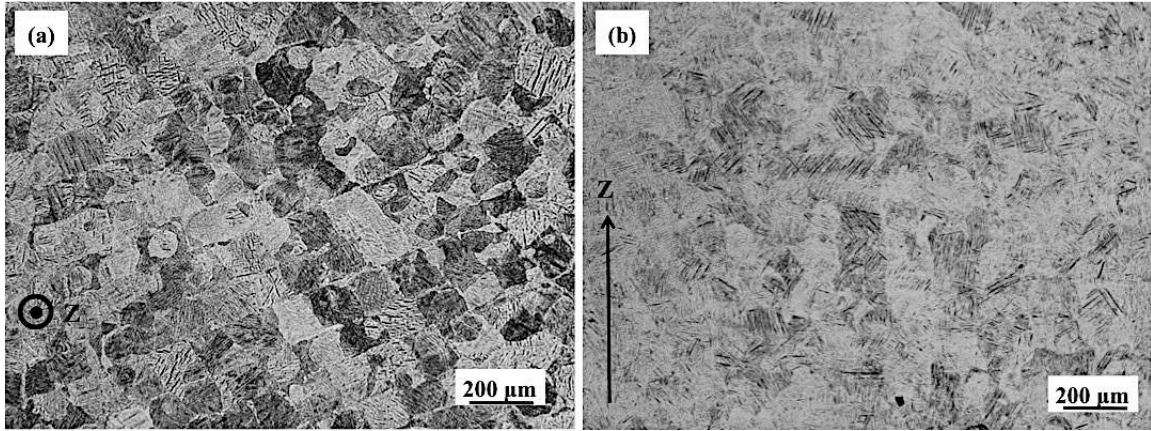


Figure 2: Optical metallographic images of the (a) deposition plane and (b) building plane of the as-printed sample.

The X-ray diffraction pattern of the as-printed sample is shown in Figure 3(a). The characteristic peaks shifted to higher angle and peaks are broadened compared to Ti- α phase, which indicates the existence of the martensite α' phase.^[17] The refinement result of as-printed sample in the 2θ angle range from 37° to 42° shows in Figure 3(b) indicating the existence of β (011) characteristic peak at 39.5° with low intensity. The small amount of β phase is likely caused by the fast cooling during DMLS, which allows the nucleation of nano-sized β particles but limits growth. Therefore, the as-printed sample mainly consists of α' martensite phase with nano-scaled β particles dispersed in the matrix.

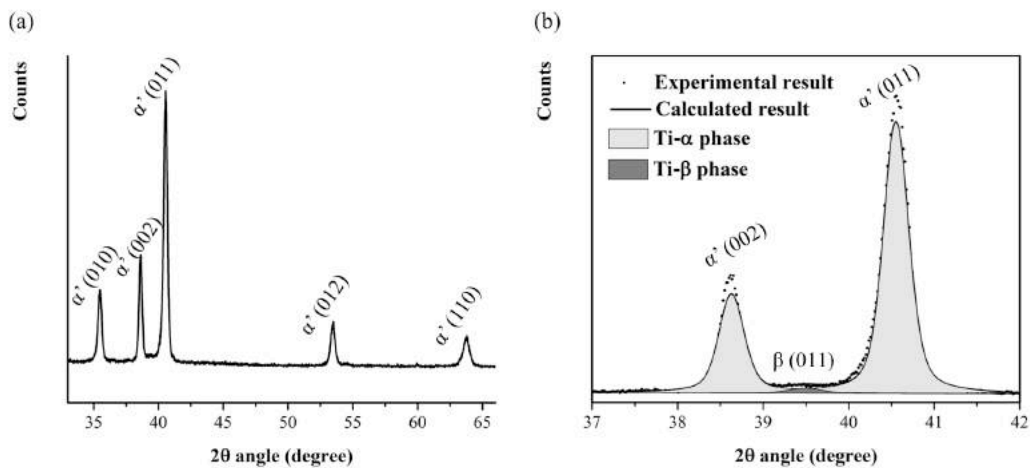


Figure 3: (a) X-ray diffraction pattern of the as-printed sample which mainly consists of α' phase, and (b) the refinement results of (a) in the 2θ angle range from 37° to 42° showing the existence of β (011) characteristic peak at 39.5° .

3.2 Post-heat treatments

The optical images and XRD patterns of the as-printed, 950STA and 1050STA is shown in Figure 4(a), (b) and (c), respectively. The as-printed sample exhibits needle-like α' martensite microstructure. Solution treatment at 950°C (in the $\alpha+\beta$ region) allows the partitioning of alloying elements. When the solution treatment temperature increased to 1050°C (in the β region), β matrix transformed to α phase and retained β phase maintained during cooling process. In both cases, the subsequent aging at 550°C effectively reduced the residual stress and allowed a slightly coarsening of β precipitates. The optical images and XRD patterns of 450SR, 550SR and 650SR are shown in Figure 5(a), (b) and (c), respectively. The microstructure after stress relieve treatments at various temperature remains lath structure. The results indicate that the initial non-equilibrium α' martensite structure experienced alloying elements partitioning, and transformed to a combination of acicular α and clustered β precipitates after stress relieve treatments. From the XRD patterns shown in Figure 5, with increasing of heat treatment temperature, the β (011) characteristic peaks changed to a narrower shape with higher intensity, indicating an increasing in β precipitates size and percentage.

Table 2: Rietveld refinement results deduced from XRD patterns of the investigated samples.

Sample	α' , α phase analysis			β phase analysis		
	a (Å)	c (Å)	FWHM*	phase percentage (%)	a (Å)	phase percentage (%)
as-printed	2.92292(2)	4.6615(2)	0.3066	> 97.9	NA	< 2.1**
950STA	2.92405(2)	4.66750(4)	0.1794	96.2	3.192(1)	3.8
1050STA	2.92417(1)	4.67120(3)	0.1064	93.5	3.1893(8)	6.5
450SR	2.92360(5)	4.6647(1)	0.2593	97.9	3.171(1)	2.1
550SR	2.92661(4)	4.66546(9)	0.2020	96.1	3.173(1)	3.9
650SR	2.92311(3)	4.66723(7)	0.1499	96.1	3.203(1)	3.9

* FWHM (full width half maximum) results are based on the Ti- α peaks at 2θ equals 40.50° with khl of (101).

** Small amount of nano-scaled β phase with broad peak and low intensity.

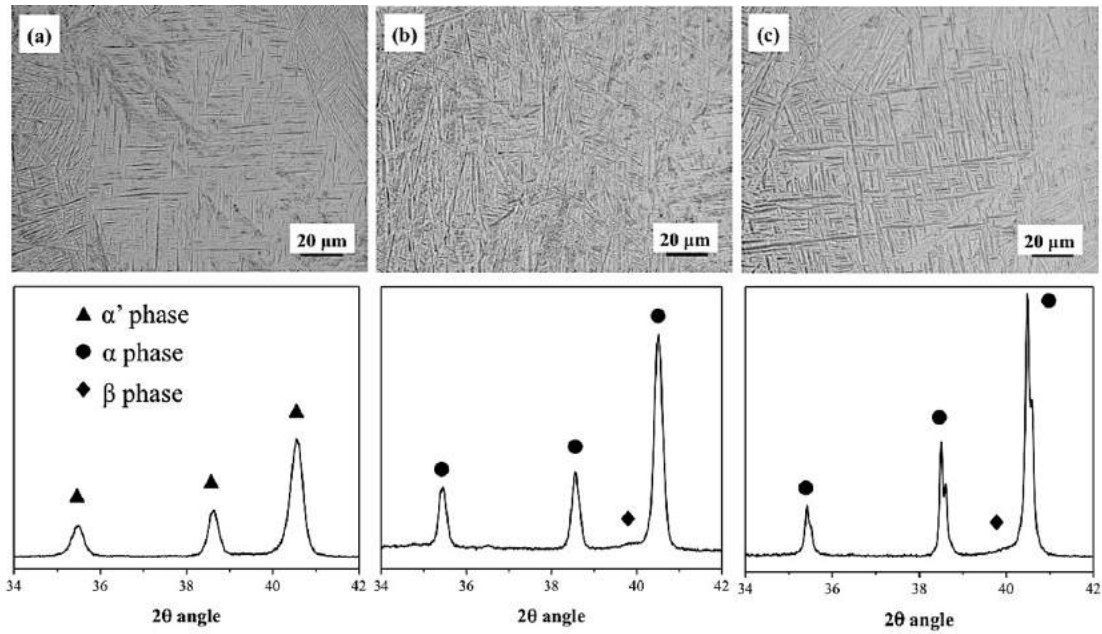


Figure 4: Optical metallographic images and X-ray diffraction patterns of (a) as-printed, (b) 950STA and (c) 1050STA. The diffraction patterns are presented in the 2θ angle range to highlight the different phases.

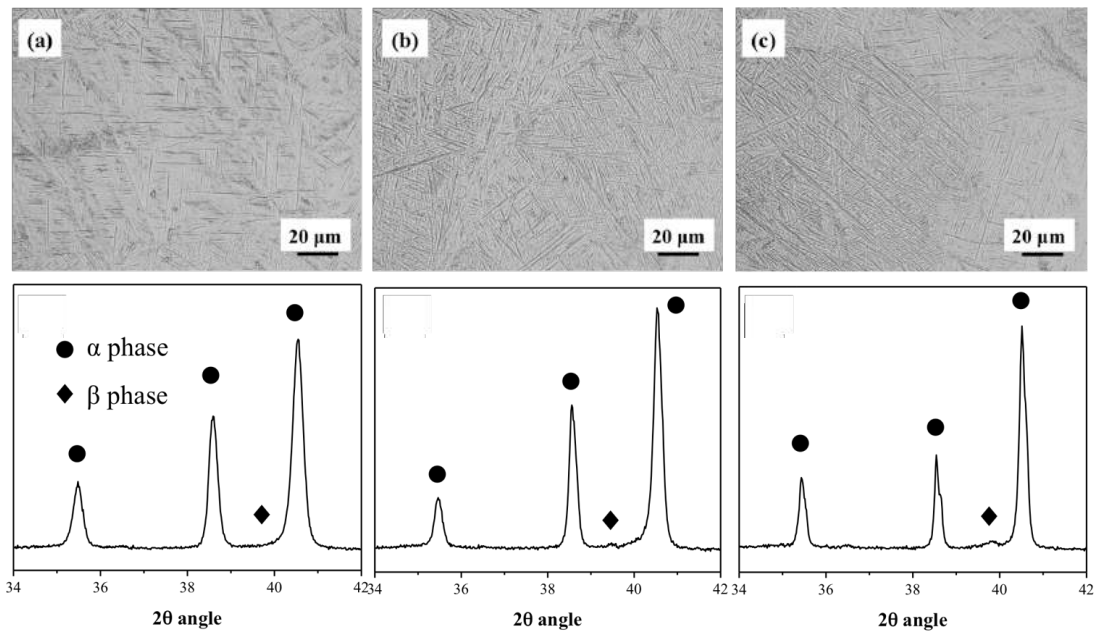


Figure 5: Optical metallographic images and X-ray diffraction patterns of (a) 450SR, (b) 550SR and (c) 650SR. The diffraction patterns are presented in the 2θ angle range to highlight the different phases.

The high magnification SEM images of as-printed and heat-treated samples are shown in Figure 6(a) to (f). In the as-printed sample, the low sintering temperature and fast interaction only resulted in small β nucleation sites with insufficient growth as also indicated by the refinement results shown in Figure 3(b). The microstructure retains the lath morphology after the heat treatments. In Figure 6(b), 950STA has fine β precipitates evenly distributed in the α matrix. In 1050STA sample (Figure 6(c)), the solution treatment temperature was above β transus temperature. During cooling, new α' structure, which is slightly thicker than the as-printed α' martensite because of the difference between DMLS process and traditional water quench, starts to form.^[8] The subsequent aging process at 550°C allows coarsening of the acicular microstructure and the growth of retained β precipitates. The morphology of 450SR, 550SR and 650SR are shown in Figure 6(d), (e) and (f), respectively. The stress relieve treatments of the as-printed sample show minute effect on the microstructural change. The high magnification SEM results indicate agglomeration of vanadium rich precipitates at high temperature stress relieve treatments in 650SR. The average lath thickness values of the investigated samples are plotted in Figure 7. The as-printed sample with fine acicular α' have an average lath thickness of 0.327 μm . The solution treatment and aging can significantly coarsen the microstructure and increase the lath thickness to 0.513 μm (950STA) and 1.093 μm (1050STA). Stress relieve treatments also coarse the lath thickness to around 0.6 μm , while the thickness change among different temperatures are not obvious.

Table 3: Residual stress values (with standard deviations) along different directions of the investigated samples.

Sample	X-direction (MPa)	Y-direction (MPa)
as-printed	+198 (9.78)	-20 (9.78)
950STA	-100 (4.08)	-85 (4.08)
1050STA	-68 (8.98)	-50 (8.98)
450SR	-2 (13.58)	-41 (13.58)
550SR	-18 (12.94)	+18 (12.94)
650SR	-11 (6.81)	-13 (6.81)

3.3 Rietveld refinement and residual stress

The Rietveld refinement results of XRD patterns are listed in Table 2. It is reported that the lattice parameters of high purity Ti - α is $a = 2.9511 \text{ \AA}$ and $c = 4.6843 \text{ \AA}$.^[17] All the calculated lattice parameters in the as-printed and heat-treated samples are lower, because titanium atoms are partially substituted by either aluminum or vanadium atoms in the hexagonal close-packed (HCP) cells. No significant change in lattice parameters was observed after the various heat treatments. Based on the refinement results, the as-printed sample has β phase of less than 2.1 wt%. With increasing of heat treatment temperature, the β phase percentage increases, which indicating a tendency towards equilibrium state.

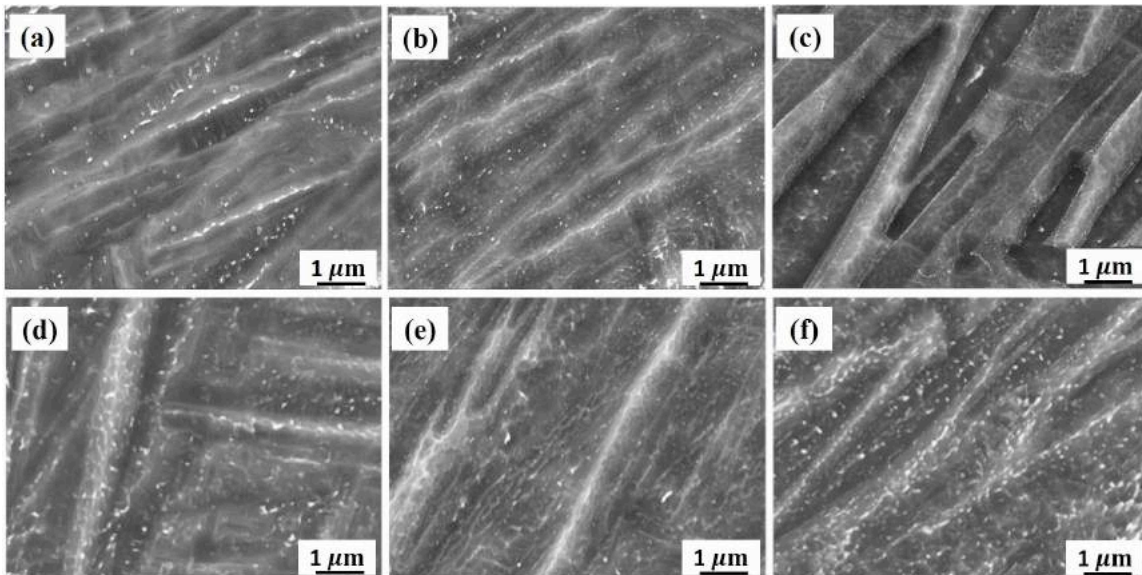


Figure 6: Scanning electron microscopy images of (a) as-printed, (b) 950STA and (c) 1050STA, (d) 450SR, (e) 550SR and (f) 650SR samples at high magnification showing lath microstructure and vanadium rich precipitates.

The residual stress values of the as-printed and various heat-treated samples are listed in Table 3. The as-printed sample possesses residual stress of +198 MPa along X axis and -20 MPa along Y axis, which will be referred to (+198 MPa, -20 MPa) in the further discussion. The high tensile and compressive residual stress in as-printed sample is caused by fast interaction and cooling during DMLS. After solution treatment and aging, the tensile residual stress transformed to compressive stress. The residual stress in 950STA and 1050STA is (-100 MPa, -85 MPa) and (-68 MPa, -50 MPa), respectively. The reduction of residual stress is more obvious after stress relieve treatments. The residual stress values of 450SR and 550SR is (-2 MPa, -41 MPa) and (-18

MPa, +18 MPa), respectively, which still possess some anisotropic behavior. This may relate to the inefficient energy at low stress relieving treatment temperature. A more effective relieve of residual stress was achieved in 650SR sample of (-11 MPa, -13 MPa).

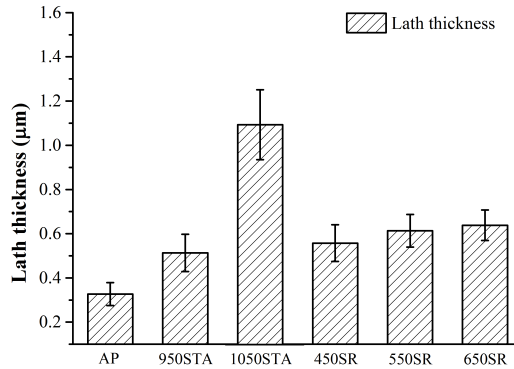


Figure 7: The average lath thickness (with standard deviations) of as-printed and various heat-treated samples.

3.4 Corrosion behavior

The polarization curves of the as-printed and various heat-treated samples are plotted in Figure 8(a) and (b), and the deduced electrochemical parameters based on Tafel plot are listed in Table 4. The corrosion potential E_{corr} refers to an equilibrium state, and the corrosion current density I_{corr} kinetically indicates the rate of the corrosion reaction. Based on the results, 950STA (-174.8 mV) and 1050STA (-110.3 mV) have nobler E_{corr} than the as-printed sample (-209.1 mV). The solution treated aged samples also have a decreased I_{corr} compared to the as-printed sample ($0.384 \mu\text{A cm}^{-2}$), indicating a lower corrosion rate.^[18] In Figure 8(b), 450SR sample has comparable I_{corr} ($0.365 \mu\text{A cm}^{-2}$) with the as-printed sample, whereas, the 550SR and 650SR has slightly improved corrosion resistance with I_{corr} of $0.341 \mu\text{A cm}^{-2}$ and $0.307 \mu\text{A cm}^{-2}$, respectively. Based on the refinement results in Table 2, higher β phase percentage can be observed at elevated heat treatment temperature. It was reported by Yu and co-workers that α and β phase in titanium alloy can form micro-galvanic cell across the grain boundary because of the compositional difference, and the anodic reaction takes place in α phase and form pits.^[19] So, the less quantity of α phase may contribute to the improved corrosion resistance in 950STA, 1050STA and 650SR.

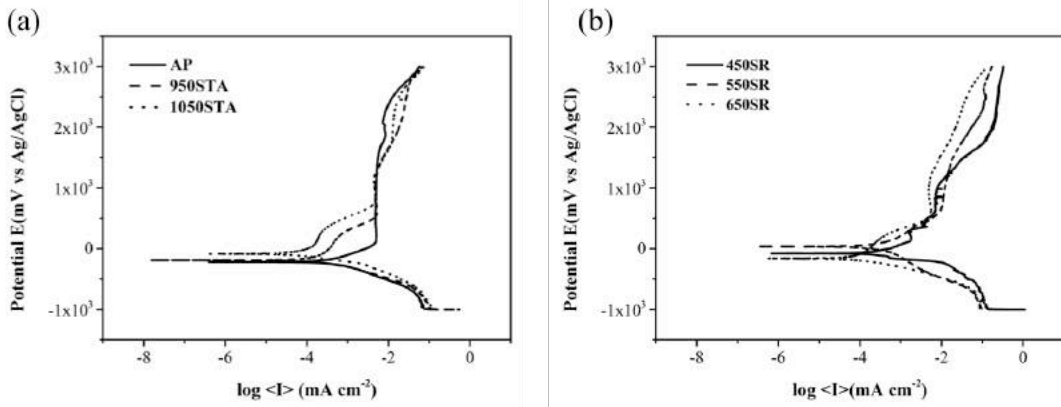


Figure 8: Polarization curves of (a) as-printed and solution treated aged samples; and (b) stress relieved samples.

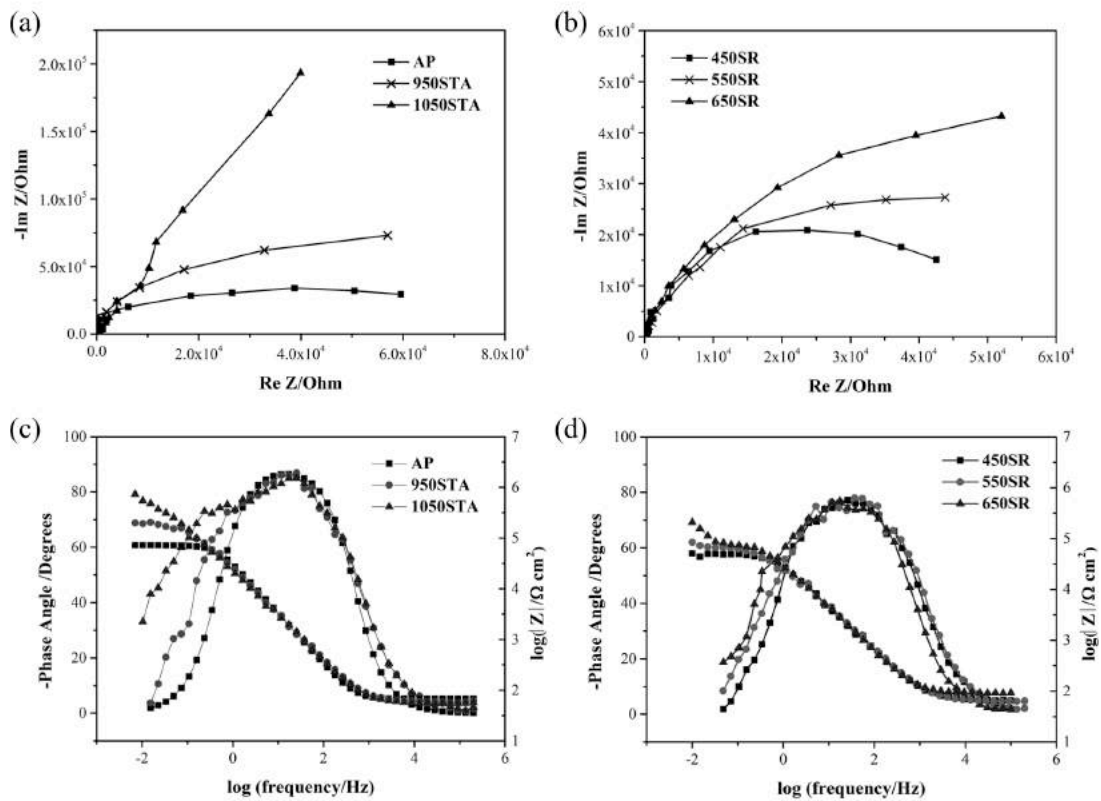


Figure 9: Nyquist plot of (a) as-printed and solution treated aged samples, and (b) stress relieved samples showing the different resistance of the passive layers. The Bode plots of (c) as-printed and solution treated aged samples, and (d) stress relieved samples indicating the existence of more than one passive layers after high temperature heat treatments.

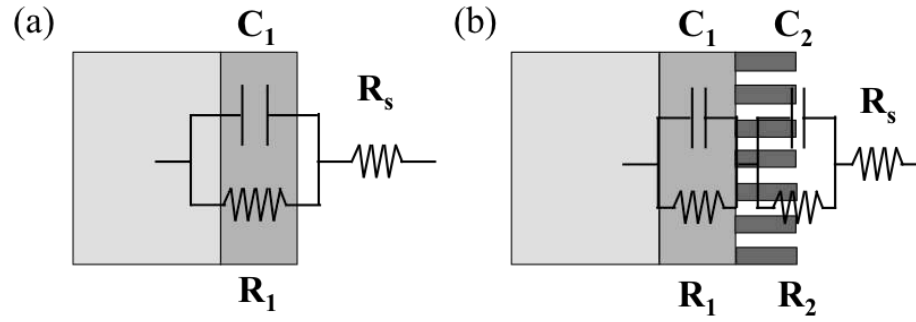


Figure 10: The equivalent circuit used to fit the electrochemical impedance results for (a) single and (b) double passive layers. C_1 and R_1 refers to the capacitance and resistance of the inner passive layer; C_2 and R_2 represents the capacitance and resistance of the outer discontinuous layer, respectively. R_s is the resistance of the electrolyte at test temperature.

Table 4: Electrochemical parameters of the investigated samples.

Sample	E_{corr} (mV)	I_{corr} ($\mu\text{A}/\text{cm}^2$)	R_s ($\Omega \text{ cm}^2$)	C_1 (μF)	R_1 ($\text{k}\Omega \text{ cm}^2$)	C_2 (μF)	R_2 ($\text{k}\Omega \text{ cm}^2$)
as-printed	-209.1	0.384	15.59	4.9	18.0	-	-
950STA	-174.8	0.152	15.40	5.9	32.7	10.1	0.139
1050STA	-110.3	0.064	17.77	8.9	93.5	8.1	0.959
450SR	-134.2	0.365	18.4	3.7	10.7	-	-
550SR	60.7	0.341	15.8	3.5	12.1	-	-
650SR	-213.0	0.307	22.3	5.2	20.5	5.2	0.544

The Nyquist plot and Bode plot for the as-printed, 950STA and 1050STA are shown in Figure 9(a) and (c), respectively. In the Nyquist plot, the diameter of the semi-circle indicates the resistance of the passive oxide layer.^[18] The resistance of the passive layer increases in the order: as-printed < 950STA < 1050STA. It was reported that the oxide layer in titanium alloys can be referred to the n-type semiconductor, and the motion of oxygen anion vacancies leads to the corrosion reaction.^[18] The low corrosion resistance of the as-printed sample is likely due to the unstable α' phase, and higher amount of defects in the passive layer grows on top of it. In Figure 9(c), the Bode plot of the as-printed sample has a symmetry shape, while shoulder peaks can be observed at low frequency side in 950STA and 1050STA, which demonstrates extra passive layer

on the sample surface with lower resistance.^[18] The Nyquist plot and Bode plot for 450SR, 550SR and 650SR samples are shown in Figure 9(b) and (d), respectively. The increased diameter of the semi-circles with increasing stress relieve treatment temperature indicates higher resistance in the 650SR sample. Interestingly, only 650SR shows a tendency to develop a shoulder peak at low frequency range. According to Alves and co-workers, the formation of passive layers on titanium alloys is time and temperature dependent.^[20] The double-passive layers can be developed in titanium alloys at 37°C very quick, while single-passive layer was observed at 25°C after immersion for 1 week in the same simulated body fluid.^[20] It is widely accepted that the protective oxides formed on the surface of titanium alloys can be simulated using either single layer capacitor or double-layer capacitors model.^[21] In the double-layer capacitors model, there are a discontinuous outer layer (aluminum oxide and vanadium oxide in Ti-6Al-4V) and a dense inner layer (mainly titanium oxide). The dense layer mainly contribute to the good corrosion resistance.^[21] The equivalent circuit used to fit the as-printed, 450SR and 550SR sample with single-passive layer is shown in Figure 10(a), where R_s denotes the solution resistance, R_1 and C_1 represent the polarization resistance and capacitance of the inner dense layer. Figure 10(b) shows the equivalent circuit used to fit the double-passive layer structure in 950STA, 1050STA and 650SR, where R_2 and C_2 refers to the resistance and capacitance of the extra passive layer, respectively. The fitting results based on different model are listed in Table 4. It was found that:

- (1) The fitting results of the solution resistance R_s (approximately $18 \Omega \text{ cm}^2$) is comparable in all investigated samples, which indicates a consistency of the electrolyte during measurements.
- (2) The value of dense layer resistance R_1 is always much higher than the porous layer resistance R_2 , which means that the good corrosion resistance of Ti-6Al-4V mainly benefits from the inner layer composed of titanium oxide. It was reported that the solute element aluminum can form a low-resistant aluminum oxide layer on the early stage,^[22] therefore the existence of this aluminum oxide layer is likely to deteriorate the passivity behavior of the alloy.
- (3) The absence of the outer passive layer in the as-printed sample is due to its limited solute element partitioning.^[3] The aluminum and vanadium atoms are trapped in the Ti- α HCP lattices because of the fast interaction during DMLS. Therefore, only single passive layer can be developed on the as-printed sample. Since the solute partitioning is insufficient under low temperature stress relieve treatments in 450SR and 550SR, which is observed from

refinement results with less β phase percentage, single-passive layer structure with low resistance of $10.7 \text{ k } \Omega \text{ cm}^2$ and $12.1 \text{ } \Omega \text{ cm}^2$ was observed.

- (4) Solution treatment at temperature close to the β transus temperature allows the aluminum and vanadium element to distribute in α and β phase, respectively. Therefore, the discontinuous outer layer can be developed. The resistance of the inner layer in 1050STA ($93.5 \text{ k } \Omega \text{ cm}^2$) is higher than 950STA ($32.7 \text{ k } \Omega \text{ cm}^2$), which is likely due to the increased β phase percentage (decreased α phase percentage). The enhanced corrosion resistance in 1050STA is likely due to the reduced percentage of α phase and α/β interface, which can be active during corrosion reaction.

4. Conclusions

The effect of solution treatment aging and stress relieving on the morphology, phase evolution and corrosion behavior of DMLS Ti-6Al-4V samples have been experimentally determined. The decomposition of α' phase to α and β phase took place during various heat treatments, with coarsening of α lath and agglomerate of β precipitates. Different degrees of relieve in residual stress was achieved after post heat treatments. A single passive layer was observed in the as-printed and low temperature stress relieved sample due to limit solute element partitioning. Double passive layer could be developed in 650SR, 950STA and 1050STA with enhanced resistance of the titanium oxide passive layer. The outer discontinuous passive layer (mainly composed on aluminum oxide) contributes less to the corrosion resistance. Furthermore, the reduced α phase percentage and α/β interface in 1050STA was likely to result in superior corrosion behavior.

Reference

- [1] M. Niinomi, *Sci. and Technol. Adv. Mater.* **2003**, 4, 445.
- [2] M. Geetha, UK. Mudali, AK. Gogia, R. Asokamani, B. Raj. *Corr. Sci.* **2004**, 46, 877-892.
- [3] I. Cvijović-Alagić, Z. Cvijović, S. Mitrović, V. Panić, M. Rakin. *Corr. Sci.* **2011**, 53, 796-808.
- [4] RW. Hsu, CC. Yang, CA. Huang, YS. Chen. *Mater. Sci. Eng., A.* **2004**, 380,100-9.
- [5] MA. Khan, RL. Williams, DF. Williams. *Biomaterials*, **1999**, 20, 631-637.
- [6] H. Malchau, P. Herberts, T. Eisler, G. Garellick, and P. Söderman. *J. Bone Joint Surg. Am.* 2002, 84, S2-S20.

- [7] Khaing, M. W., JYH. Fuh, L. Lu. *J. Mater. Process. Technol.* **2001**, 113, 269-272.
- [8] B. Vrancken, L. Thijs, JP. Kruth, J. Van Humbeeck. *J. Alloys Compd.* **2012**, 541, 177-85.
- [9] SL. Lu., HP. Tang, YP. Ning, N. Liu, DH. StJohn, M. Qian. *Metall. Mater. Trans. A*, **2015**, 45, 3824-3834.
- [10] DA. Hollander, M. Von Walter, T. Wirtz, R. Sellei, B. Schmidt-Rohlfing, O. Paar, HJ. Erli. *Biomaterials*. **2006**, 31, 955-63.
- [11] S. Leuders, M. Thöne, A. Riemer, T. Niendorf, T. Tröster, HA. Richard, HJ. Maier, *Int. J. Fatigue*, **2013**, 48, 300-307.
- [12] Handbook, A. S. M. *Heat treating, vol. 4*. ASM International, Materials Park, OH, **1991**.
- [13] HM. Rietveld. *J. Appl. Crystallogr.* **1969**, 2, 65-71.
- [14] HM. Rietveld. *Acta Crystallogr.* **1967**, 22, 151-152.
- [15] ME. Fitzpatrick, AT. Fry, P. Holdway, FA. Kandil, J. Shackleton, L. Suominen. *Determination of residual stresses by X-ray diffraction*. National Physical Laboratory, **2005**.
- [16] L. Thijs, F. Verhaeghe, T. Craeghs, J. Van Humbeeck, JP. Kruth. *Acta Mater.* **2010**, 58, 3303-3312.
- [17] L. Zeng, TR. Bieler. *Mater. Sci. Eng., A*, **2005**, 392, 403-414.
- [18] DA. Jones. *Principles and prevention of corrosion*. Macmillan, **1992**.
- [19] YC. Yu, LX. Yang, CC. Shen, B. Luan, TP. Perng, *Scr. Mater.* **2007**, 56.1019-1022.
- [20] VA. Alves, RQ. Reis, IC. Santos, DG. Souza, TD. Goncalves, MA. Pereira-da-Silva, A. Rossi, LA. Da Silva. *Corr. Sci.* **2009**, 31, 2473-82.
- [21] Sl. Assis, I. Costa. *Mater. Corros*, **2007**, 58, 329-333.
- [22] R. Singh, A. Kurella, NB. Dahotre. *J. Biomater. Appl.* **2006**, 21, 49-73.

CHAPTER 6

PAPER IV: EFFECTS OF HOT ISOSTATIC PRESSING ON THE MICROSTRUCTURE, MECHANICAL PROPERTIES AND CORROSION BEHAVIOR OF Ti-6Al-4V VIA DIRECT METAL LASER SINTERING

Yangzi Xu, Yuan Lu, Jianyu Liang, Richard D. Sisson, Jr.

To be submitted: *Additive Manufacturing* (Manuscript form)

Highlights:

1. The direct metal laser sintered Ti-6Al-4V part is comprised of fine α' martensite phase with nano-scaled β precipitates dispersed in the matrix. Pores with different morphology can be observed in the as-printed parts. HIPing in the $\alpha+\beta$ region can coarse the α lath thickness and increasing β phase fraction, and significantly reduce the porosity.
2. All of the HIPed samples show more passive anodic polarization behavior than the as-printed one, and the corrosion resistance is better under elevated HIPing temperature. The EIS results indicate double passive layer can be developed at the HIPed temperature above 550°C, and the enhanced corrosion resistance under high temperature HIPing is mainly contributed by the inner barrier layer.

Effect of Hot Isostatic Pressing on the Microstructure, Mechanical Properties and Corrosion Behavior of Direct Metal Laser Sintered Ti-6Al-4V

Yangzi Xu^{1*}, Yuan Lu¹, Jianyu Liang¹, Richard D. Sisson¹

¹Department of Materials Science and Engineering, Worcester Polytechnic Institute, 100 Institute Road, Worcester, MA 01609, USA

Abstract

In this paper, the effect of hot isostatic pressing (HIP) on the microstructure, mechanical properties and corrosion behavior of direct metal laser sintered Ti-6Al-4V was investigated experimentally. The as-printed Ti-6Al-4V parts mainly comprised of fine α' martensite phase with a high porosity of 0.29%. HIPing under various temperatures were applied in the $\alpha+\beta$ region on the as-printed Ti-6Al-4V parts aimed to close internal pores. Coarsened microstructures with reduced Vickers hardness were observed under high temperature HIPing. The corrosion behavior of as-printed and HIPed samples were analyzed in Ringers solution at 37°C electrochemically. It was found out that the HIPed samples show more passive anodic polarization behavior than the as-printed one. Double passive layers can be developed under HIPing temperature higher than 550°C, and the enhanced corrosion resistance under high temperature HIPing is mainly contributed by the inner barrier layer.

Key Words:

Ti-6Al-4V; direct metal laser sintering; microstructure; hot isostatic pressing; corrosion behavior

* Corresponding author at: Worcester Polytechnic Institute, Department of Materials Science and Engineering. Tel: +1 508 831 8333

E-mail address: yxu@wpi.edu (Y. Xu)

1. Introduction

The four main types of metallic biomaterials are stainless steel, cobalt alloys, titanium and titanium alloys. Among them, titanium alloys are becoming more and more popular these years on applications of dental and orthopedic implants due to good mechanical properties, biocompatibility, lack of allergic reaction and excellent corrosion resistance [1]. Ti-6Al-4V is used on the tibial component in total knee arthroplasty (TKA) prosthesis, hip cup in total hip replacement and bridge in dental implant [2]. The excellent corrosion resistance benefits from the protective TiO₂ film formed on the surface with a thickness of 1 to 4 nm [3]. However, it was found that Ti-6Al-4V implants failed due to fretting corrosion and wear. Several works reported that the fretting corrosion could be caused by dissolution of V₂O₅ or the formation of chloro-complex in the biological fluid [4][5].

The fast developing of additive manufacturing not only enables the fabrication of intrinsic structures that used to be impossible with conventional casting, but also saves source and improves efficiency compared to subtractive manufacturing [6][7]. Direct metal laser sintering (DMLS) is an additive manufacture technique that uses a solid-state laser to sinter the metallic powder successively based on the pre-designed computer-aided design (CAD) file [8]. The whole sintering process is conducted in a chamber protected by inert gas. Highly customized products could be sintered directly from the CAD file, meanwhile ensure the low cost and high efficiency. However, due to the fast cooling rate in DLMS, the microstructure of the fabricated products are likely to have the non-equilibrium martensite phase, which are different from commercial mill annealed Ti-6Al-4V [9]. It was reported that microstructures have some effect on the corrosion behavior of Ti-6Al-4V through solute partitioning [10]. Furthermore, the direct fabrication with layer-wise shaping will introduce internal stress and porosity, where the influence on the mechanical properties is usually impaired [9]. Therefore, lots of efforts have been placed on applying various post-treatments on the as-printed parts to further improve mechanical properties. Hot isostatic pressing (HIP) is widely used in processing metal and ceramics by applying a high temperature and high gas pressure simultaneously to the parts in order to form solid parts [11]. Lu et al. applied HIPing on the as-printed sample from electron beam melting in the $\alpha+\beta$ region and found out improved density to 4.426 g/cm³, which is close to the commercial mill annealed Grade 5 alloy [12], and they also observed the precipitation of secondary α in the β phase area after HIPing. Based on the results from Al-Bermani et al.,

HIPing at higher temperature (approximately 900°C) in the $\alpha+\beta$ region can enhance the elongation to 14.0%, which is close to the value of Grade 5 Ti-6Al-4V alloy of 16.0% [13]. However, no study addressed the corrosion behavior change during HIPing at different temperature and cooling rate.

In this work, various HIPing temperatures (450°C, 550°C and 799°C) were applied on the as-printed samples. The effects of HIPing temperatures on the morphology and phase analysis were examined by scanning electron microscopy (SEM) and X-ray diffraction (XRD). The corrosion behavior was analyzed by electrochemical impedance and polarization measurements in Ringers solution at 37°C.

2. Materials and methods

2.1 Materials and sample preparation

The Ti-6Al-4V parts were fabricated by EOS e-Manufacturing Solutions (Krailing, Germany) via direct metal laser sintering (DMLS) technique. Samples were printed at a scanning speed of 1250mm/s, a laser power of 340W, a hatch spacing (the distance between two adjacent scan vectors) of 120 μ m and a layer thickness of 60 μ m. Layers were scanned using a zigzag pattern and rotated 90° between each layer. The Ti-6Al-4V parts were printed as tensile bars based on ASTM standard and the building plane is referred to the XY plane, and the building direction is designated as the Z direction.

Table 1: Hot isostatic pressing (HIPing) conditions of the as-printed samples.

Sample designation	Temperature (°C)	Time (hr)	Pressure (bar)	Cooling method*
450AC	450	4	1000	AC
550AC	550	4	1000	AC
799AC	799	4	1000	AC

* AC: air-cooling

The as-printed samples (designated as AP) were then hot isostatic pressed by Quintus Technology LLC (Sweden) in Argon gas. Three different HIPing temperature were selected at 450°C, 550°C and 799°C (in $\alpha+\beta$ region), and held for 4 hours under a pressure of 1000 bar followed by air-cooling. The HIPing conditions are listed in Table 1. Then, the AP and HIPed samples were cut using an abrasive sectioning machine with SiC blade and mounted by epoxy resin. The mounted samples were sequentially ground up to 1200 grit silicon carbide paper,

followed by final finish with colloidal silica suspension on ChemoMet polishing cloth to achieve a mirror surface. To reveal the microstructure, Kroll's reagent (2ml HF, 5ml HNO₃ and 100ml H₂O) was used to etch the as-polished surface for 30 seconds. Because of the layer-wise building process, the building plane and deposition plane (the plane perpendicular to the building direction) are considered during metallographic investigation. In this study, the investigated planes for each sample are the deposition planes (XY plane).

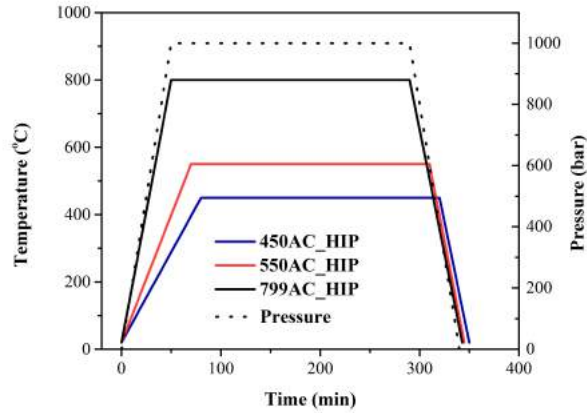


Figure 1: The variation of temperature over time during the HIP procedures under 450°C, 550°C and 799°C for 4 hours and followed by air-cooling.

2.2 Characterization techniques

The microstructure analysis was conducted on a JEOL JSM-7000F scanning electron microscope (SEM) was used to evaluate the microstructure. Phase identifications were conducted by a PANalytical Empyrean 2 X-ray diffractometer (XRD) with Cu-K_α. Rietveld refinement was used to reveal the phase fraction and lattice parameters of the investigated samples [15][16]. The Vickers hardness measurements were conducted on the as-polished sample surface, and measured with a Microhardness tester at a force of 200 gf. The hardness measurements were duplicated for ten measurements on each sample. The average lath thickness values were estimated using ImageJ from ten randomly picked area.

2.3 Electrochemical tests

The electrochemical investigations of the as-printed and HIPed samples were performed in a three-electrode cell, in which an Ag/AgCl (3M NaCl) and a Platinum wire (surface area: 3.6 cm²) were served as the reference and counter electrode, respectively. The tested metallic parts were

served as working electrode. In order to ensure better conductivity, a copper wire was attached to the test sample by conductive tape and mounted using epoxy resin as the working electrode. The surface area exposed to the electrolyte is 0.25 cm^2 . The working electrode was prepared by the same manner as the metallography analysis. Naturally aerated Ringer's solution (6.5g/l NaCl, 0.14g/l KCl, 0.2g/l NaHCO_3 , 0.12 CaCl_2 and 0.4g/l glucose) was used as the electrolyte at 37°C . A Potentiostat (Bio-Logic, Inc.) was used to measure the open circuit potential after immersion the working electrode into the electrolyte. Electrochemical impedance spectra (EIS) were measured at a frequency range of 100 kHz to 10 mHz with the perturbation amplitude of 10 mV after the open circuit potential reached a plateau value. Subsequently, polarization curves were obtained at a scanning rate of 1 mV/s from -1000 mV to +2000 mV. The Bio-Logic software was used to analyze the electrochemical parameters. All reported electrode potentials were referred to the Ag/AgCl reference electrode.

3. Results and discussion

3.1 As-printed samples

The optical metallography of AP sample in the plane perpendicular and parallel to the building Z direction is shown in Figure 2(a) and (b), respectively. Due to the layer wise processing method, the microstructure of the deposition and building planes are different. The grid pattern in the deposition plane was caused by the zigzag-scanning pattern during DMLS, which is usually used to reduce porosity. Elongated prior β grains can be seen on the building plane in Figure 2(b), since the heat transfer direction during DMLS was along the Z direction. Same observations on the difference of microstructure in the as-printed samples are reported in the reference [9]. As pointed out by arrows in Figure 2(c) and (d), pores can be seen near the sample surface with different shapes. Spherical and elongated pores are likely caused by entrapped gas bubbles and lack of fusion, respectively [12][13]. The porosity of the AP sample was estimated as 0.29% from image analysis. It was reported by Leuders et al. that micron sized pores in the AP sample can affect the fatigue strength, since the pores act as crack nucleation sites during fatigue testing [17]. Poor elongation and tensile properties were observed in the AP samples [12][13].

The high magnification SEM image of the AP sample is shown in Figure 3(a) indicating the acicular α' martensite microstructure, with the bright nano-scaled β phase dispersed in the α' matrix. This fine microstructure was caused by the fast cooling rate during DMLS [9]. The XRD pattern of the AP sample is shown in Figure 3(b). The characteristic peaks shifted to higher angle

and peaks are broadened compared to Ti- α phase, which indicates the existence of the martensite α' phase [17]. The fast sintering and quick cooling rate during DMLS leads to the acicular α' phase in the AP sample.

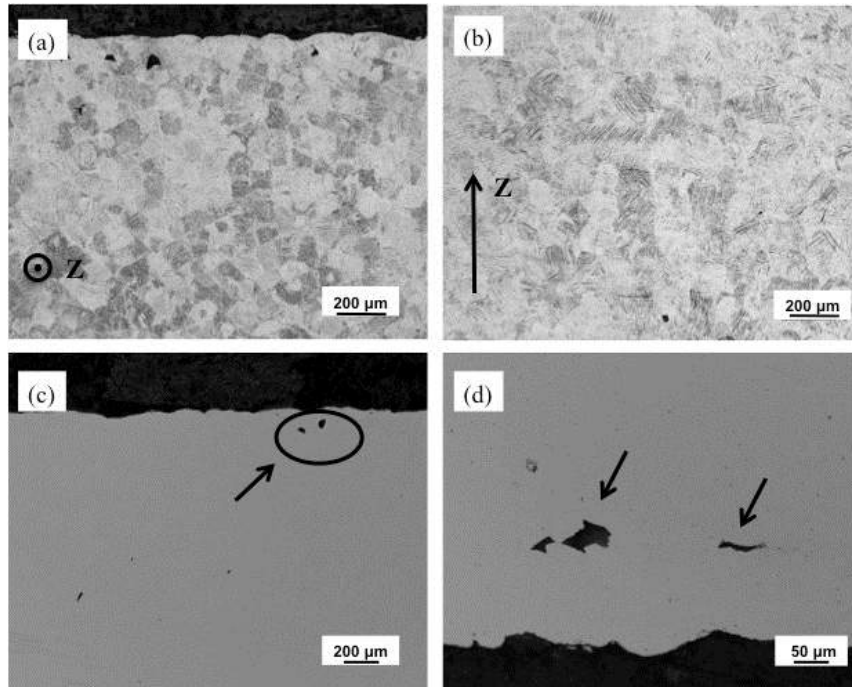


Figure 2: Optical metallography of the as-printed sample (a) perpendicular and (b) parallel to the building direction Z-axis. (c) Pores near the sample surface and (d) pores with elongated shape and caused by lack of fusion.

3.2 Microstructure of the HIPed samples

The SEM images of 450AC, 550AC and 799AC are shown in Figure 4(a), (b) and (c), respectively. Similar to the as-printed sample, the HIPed samples have lath microstructure, and the lath thickness coarsened with increasing HIPing temperature. As shown in Figure 4(a) and (b) for 450AC and 550AC, fine lath microstructure with dispersed Ti- β precipitates can be observed (the bright region in SEM), while in the 799AC sample shown in figure 4(c), the β phase precipitates along the lath boundaries.

The XRD spectra of the 450AC, 550AC and 799AC samples are shown in Figure 4(d), (e) and (f), respectively. With increasing of HIPing temperature from 450°C to 799°C, intensity of the characteristic peak of Ti- β (011) (marked in solid circle) at 2θ angle equals 39.6° increases, indicating increased β phase fraction.

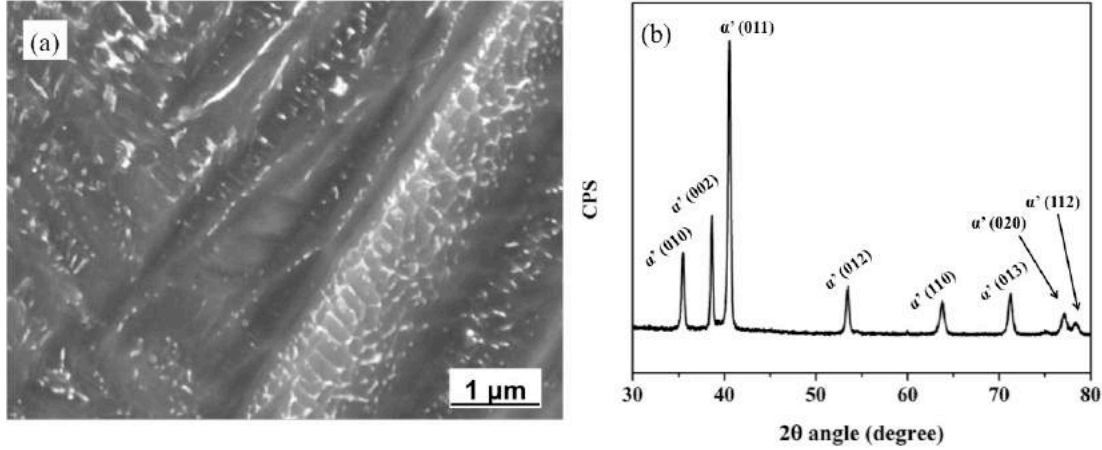


Figure 3: High magnification SEM image (a) and XRD pattern in the 2θ angle: 30° to 80° (b) of the as-printed sample.

3.3 Phase analysis and Rietveld refinement

The XRD patterns of the AP, 450°C , 550°C and 799°C HIPed samples show very different relative intensity of the α characteristic peaks from those of the standard pattern, which indicating a strong texture [18]. The Rietveld refinement results of XRD patterns are listed in Table 2. It was reported that the lattice parameters in high purity Ti- α is $a = 2.9511 \text{ \AA}$ and $c = 4.6843 \text{ \AA}$. The refinement results of AP and HIPed samples have the lattice parameters smaller than those values. In the AP sample, the fast cooling limited alloying element partitioning, so the hexagonal close packed (HCP) cells are distorted by the aluminum and vanadium atoms. HIPing process allows partitioning of vanadium atoms to stabilize the β phase, and the β phase fraction increased with increasing HIPing temperature.

Table 2: Rietveld refinement results deduced from XRD patterns of the investigated samples.

Sample	α' , α phase analysis			β phase analysis	
	a (\AA)	c (\AA)	FWHM*	phase percentage (%)	a (\AA) phase percentage (%)
AP	2.92292(2)	4.6615(2)	0.3066	> 97.9	NA < 2.1
450AC	2.92138(8)	4.6624(1)	0.2444	97.7	3.20(4) 2.3
550AC	2.92176(9)	4.6596(2)	0.3017	96.5	3.1492(9) 3.5
799AC	2.92436(7)	4.6668(1)	0.2444	95.6	3.2121(5) 4.4

* FWHM results are based on the Ti- α peaks at 2θ equals 40.50° with khl of (101).

This process also allows some relieve of the microstrain in the distorted HCP α lattices. With increasing of HIPing temperature from 450°C to 799°C, the lattice parameters for Ti- α phase increased from $a = 2.9214 \text{ \AA}$, $c = 4.6624 \text{ \AA}$ to $a = 2.9244 \text{ \AA}$, $c = 4.6668 \text{ \AA}$, which are closer to the real HCP α phase lattice parameters. Spreadborough et al. reported the Ti- β phase has a face center cubic (FCC) crystallography with a lattice parameter of $a=3.311 \text{ \AA}$ [18], and its' characteristic peak with 100% intensity appears at 2θ angle equals 38.2° . However, a shift of the β phase peaks to a higher 2θ angle of 38.9° was observed in all HIPed samples, which indicating the existence of a high internal stress [18].

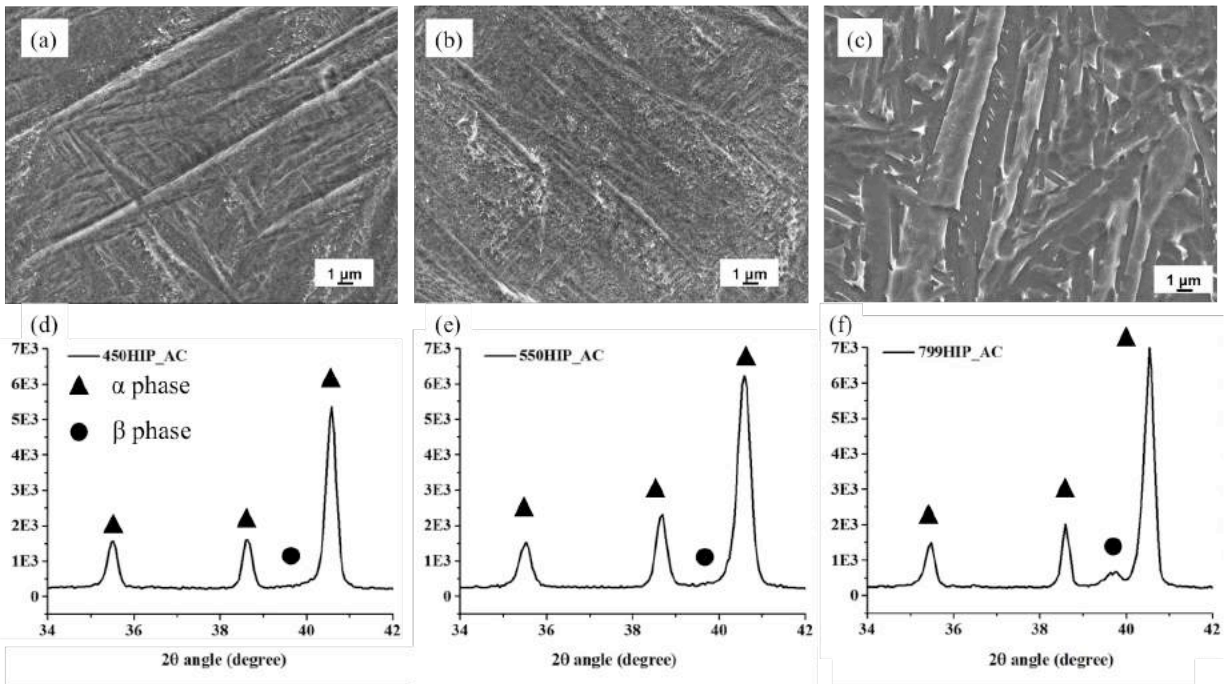


Figure 4: SEM images of (a) 450AC, (b) 550AC and (c) 799AC. XRD patterns of (d) 450AC, (e) 550AC and (f) 799AC with highlighted region of 2θ angle equals 34° to 42° .

Based on the Rietveld refinement in Table 2, the fraction of β phase in the AP sample is less than 2.1% because the nano-scaled β phase is hard to refine via XRD. The β phase percentage increased to 2.3%, 3.5% and 4.4% in 450AC, 550AC and 799AC, respectively. Since HIPing in the $\alpha + \beta$ region allows partitioning of aluminum and vanadium to respectively stabilize α and β phase, the β phase starting to develop during this process.

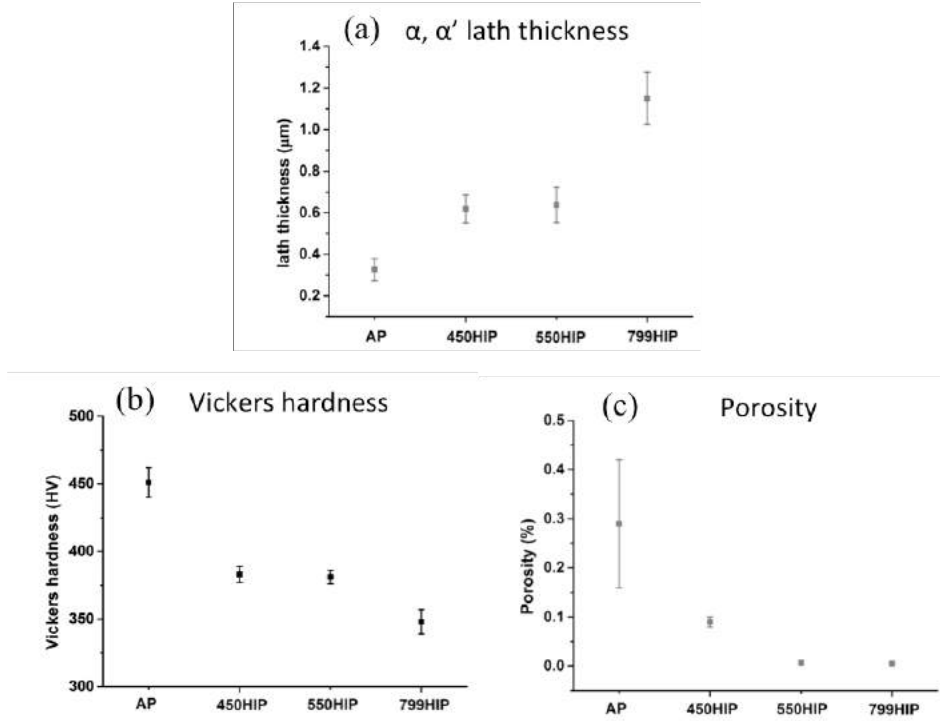


Figure 5: (a) The average lath thickness, (b) Vickers hardness values and (c) porosity (with standard deviations) of the as-printed and hot isotatic pressed samples.

3.4 Lath thickness, Vickers hardness and porosity

The measured lath thickness of AP and HIPed samples are plotted in Figure 5(a). AP sample has fine acicular α' with average lath thickness of $0.327 \pm 0.53\mu\text{m}$. HIPing in the $\alpha+\beta$ field allows the coarsening of acicular lath, and its thickness increased to $0.620 \pm 0.68\mu\text{m}$ and $0.638 \pm 0.86\mu\text{m}$ after 450°C and 550°C hot isostatic pressing, respectively. With elevated HIPing temperature of 799°C followed by air-cooling, the lath thickness increased to $1.15 \pm 0.13\mu\text{m}$, and some transformed β precipitates can be seen along the lath edge in Figure 4(c).

The measured average Vickers hardness with standard deviations of AP and HIPed samples are plotted in Figure 5(b). The microhardness of AP has the highest value of 451 ± 11 due to the fine martensite microstructure. After HIPing at 450°C and 550°C for 4 hours, the microhardness decreased to 383 ± 6.3 and 381 ± 5 , respectively. At elevated HIPing temperature of 799°C in the $\alpha + \beta$ region, the microhardness values further decreased to 348 ± 9 which is related to the coarsened lath microstructure. Larger lath thickness and lower microhardness have been seen in the 799°C HIPed samples. Therefore, the HIPing temperature has a profound influence on lath thickness and Vickers microhardness.

The porosity measured based on image analysis of the AP and HIPed samples are shown in Figure 5(c). The AP sample has high porosity of $0.29 \pm 0.15\%$, and the big variation is due to the non-uniformed distribution of internal pores. The porosity value decreased to 0.009% after HIPing at relative low temperature of 450°C . When the HIPing temperature increased to 799°C , the porosity has a significant decrease to 0.003%, indicating HIPing at high temperature in the $\alpha + \beta$ region is more effective in reducing porosity.

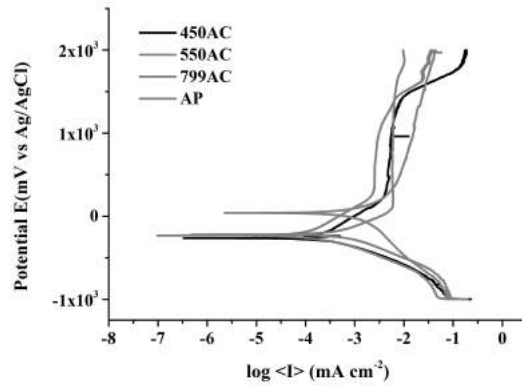


Figure 6: Polarization curves of as-printed and hot isostatic pressed sampels.

3.5 Corrosion behavior

Typical polarization curves obtained in Ringers solution for HIPed samples at 450°C , 550°C and 799°C followed by air-cooling are shown in Figure 6. The electrochemical parameters deduced from polarization curves using Tafel plots have been summarized in Table 3. The polarization curves show that all the samples passivated in Ringers solution at 37°C . In Figure 6, the anodic polarization curves of the AP sample shows no significant change of current density with increasing of potential up to 1.9 V. For the 450°C HIPed sample, the anodic polarization curves have a transition behavior in the potential of 1.5 to 1.7 V, which is a rapid increase of the current density at a specific potential. It was proved by previous studies that the transition in the potential range of 1.15 to 2.0 V (SCE) is caused by the crystallization and/or the formation of new phases from amorphous TiO_2 , and the sudden increasing of the current density is due to an enhanced conductivity of the oxide film formed under higher potential [23]. In Figure 6, the 799AC sample always has a lower current density than AP, 450AC and 550AC, indicating an improved corrosion behavior under high temperature HIPing.

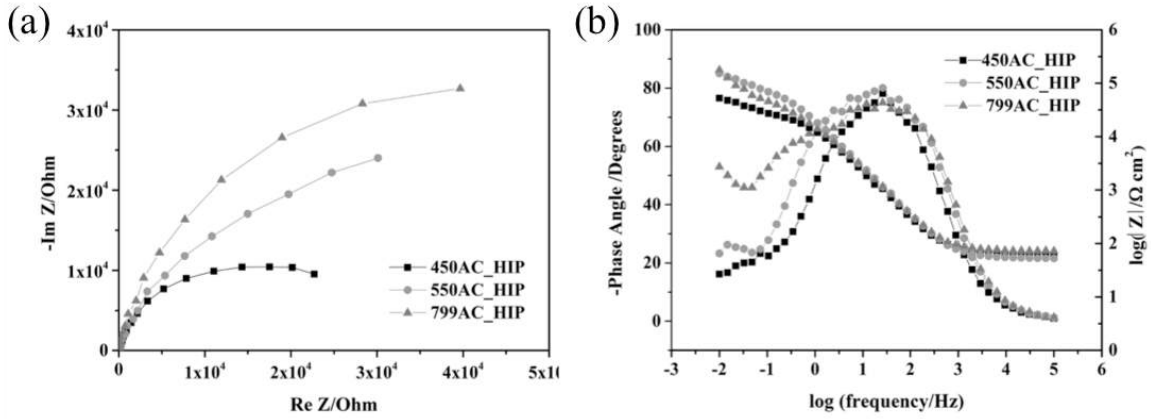


Figure 7: (a) Nyquist plot and (b) Bode plot of the hot isostatically pressed samples. The inset in (a) shows the equivalent circuit used to fit the electrochemical results.

The corrosion potential (E_{corr}) and corrosion current density (I_{corr}) deduced using Tafel plots are shown in Table 3. E_{corr} is an indicator of the stability of the surface condition, and I_{corr} illustrates the amount of material that will be lost during corrosion reaction [21]. The minor variation of corrosion potential indicates a consistent surface condition of the investigated samples. The AP sample has the highest corrosion current density of $0.34 \mu\text{A}/\text{cm}^2$, whereas all of the HIPed samples have lower corrosion current density values. The I_{corr} value for 450AC, 550AC and 799AC sample is 0.28, 0.152 and $0.062 \mu\text{A}/\text{cm}^2$, respectively, indicating that HIPing at high temperature can further improve the corrosion behavior.

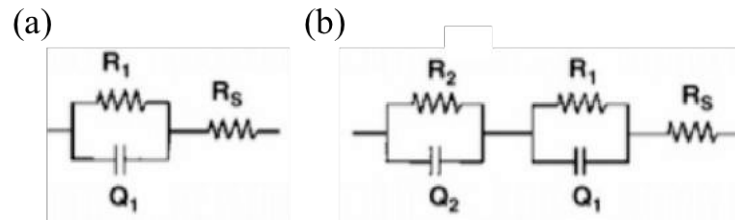


Figure 8: The equivalent circuit used to fit the electrochemical results for (a) single passive layer (AP and 450AC) and (b) double passive layer (550AC and 799AC).

To further characterize the passive layers of samples with various HIPing treatments, electrochemical impedance spectroscopy (EIS) measurements were performed. The Nyquist plot and Bode plot of HIPed sample under 450°C , 550°C and 799°C is shown in Figure 7(a) and (b), respectively. In Figure 7(b), the EIS result for 550AC and 799AC exhibits double time constant behavior, whereas, the Bode plots of AP and 450AC sample shows single passive layer.

According to previous works, the behavior of the passive layers in titanium alloys can be simulate using the equivalent circuit shown in Figure 8(a) and (b) for single and double passive layer, respectively. The solution resistance refers to R_s , and the double passive layers have close behavior as capacitor, so a resistance (R_1 and R_2) and capacitance (C_1 and C_2) in parallel combination is used to represent each layer [22].

Table 3: Electrochemical parameters of the investigated samples.

Sample	E_{corr} (mV)	I_{corr} ($\mu\text{A}/\text{cm}^2$)	R_s ($\Omega \text{ cm}^2$)	C_1 (μF)	R_1 ($\text{k}\Omega \text{ cm}^2$)	C_2 (μF)	R_2 ($\text{k}\Omega \text{ cm}^2$)
AP	-197.4	0.344	15.59	4.9	18.0	-	-
450AC	-240.5	0.280	20.6	8.0	12.9	-	-
550AC	33.3	0.152	19.5	6.0	20.4	11.3	0.348
799AC	-210.4	0.062	22.3	9.1	50.6	6.9	0.641

The double layers refer to an inner barrier layer (mainly comprised by TiO_2), and an outer porous layer (Al_2O_3 and V_2O_5) [22][23]. The deduced EIS results are summarized in Table 3. The resistance for the barrier layer increases with increasing of the HIPing temperature, as the value for AP is $18.0 \text{ k}\Omega \text{ cm}^2$, which increased to $50.6 \text{ k}\Omega \text{ cm}^2$ after high temperature HIPing. The improved corrosion resistance after high temperature HIPing in the $\alpha+\beta$ region is likely due to the increased β phase fraction. It was reported by Yu et al. that the vanadium rich β phase is less susceptible to corrosion reaction compared to α phase [18]. Therefore, the electrochemical measurement results are consistent with the XRD data that increasing of β phase fraction can decrease the corrosion current density.

4. Conclusions

The effect of hot isostatic pressing temperature on the microstructure, mechanical properties and corrosion behavior of direct metal laser sintered Ti-6Al-4V was investigated experimentally. Three different HIPing temperatures were selected at 450°C , 550°C and 799°C for 4 hours and followed by air-cooling. The following conclusions can be addressed:

- (1) The direct metal laser sintered samples comprised of fine α' martensite phase. The different morphology on the deposition and building planes is due to the layer wise building strategy.
- (2) HIPing in the $\alpha+\beta$ region can coarse the α lath thickness and increasing β phase fraction. This effect is increasing with increased HIPing temperature: the 799AC sample has greater α lath

thickness and β phase percentage. HIPing can significantly reduce the internal porosity from 0.29% in the as-printed sample to 0.003% in the 799°C HIPed part.

- (3) All of the HIPed samples show more passive anodic polarization behavior than the as-printed one, and the corrosion resistance is better under elevated HIPing temperature. The electrochemical results indicate the HIPed samples have double passive layers, and the enhanced corrosion resistance under high temperature HIPing is mainly contributed by the inner barrier layer.

Reference

- [1] Niinomi, M. (2003). Recent research and development in titanium alloys for biomedical applications and healthcare goods. *Science and technology of advanced Materials*, 4(5), 445-454.
- [2] Hsu, R. W. W., Yang, C. C., Huang, C. A., & Chen, Y. S. (2004). Electrochemical corrosion properties of Ti–6Al–4V implant alloy in the biological environment. *Materials Science and Engineering: A*, 380(1), 100-109.
- [3] Marino, C. E., de Oliveira, E. M., Rocha-Filho, R. C., & Biaggio, S. R. (2001). On the stability of thin-anodic-oxide films of titanium in acid phosphoric media. *Corrosion Science*, 43(8), 1465-1476.
- [4] Cvijović-Alagić, I., Cvijović, Z., Mitrović, S., Panić, V., & Rakin, M. (2011). Wear and corrosion behaviour of Ti–13Nb–13Zr and Ti–6Al–4V alloys in simulated physiological solution. *Corrosion Science*, 53(2), 796-808.
- [5] Alves, V. A., Reis, R. Q., Santos, I. C. B., Souza, D. G., Gonçalves, T. D. F., Pereira-da-Silva, M. A., ... & Da Silva, L. A. (2009). In situ impedance spectroscopy study of the electrochemical corrosion of Ti and Ti–6Al–4V in simulated body fluid at 25 C and 37 C. *Corrosion Science*, 51(10), 2473-2482.
- [6] Webb, P. A. (2000). A review of rapid prototyping (RP) techniques in the medical and biomedical sector. *Journal of Medical Engineering & Technology*, 24(4), 149-153.
- [7] Mazzoli, A. (2013). Selective laser sintering in biomedical engineering. *Medical & biological engineering & computing*, 51(3), 245-256.
- [8] Barucca, G., Santecchia, E., Majni, G., Girardin, E., Bassoli, E., Denti, L., ... & Mengucci, P. (2015). Structural characterization of biomedical Co–Cr–Mo components produced by direct metal laser sintering. *Materials Science and Engineering: C*, 48, 263-269.

- [9] Vrancken, B., Thijs, L., Kruth, J. P., & Van Humbeeck, J. (2012). Heat treatment of Ti6Al4V produced by Selective Laser Melting: Microstructure and mechanical properties. *Journal of Alloys and Compounds*, 541, 177-185.
- [10] Geetha, M., Mudali, U. K., Gogia, A. K., Asokamani, R., & Raj, B. (2004). Influence of microstructure and alloying elements on corrosion behavior of Ti-13Nb-13Zr alloy. *Corrosion Science*, 46(4), 877-892.
- [11] Bocanegra-Bernal, M. H. "Hot isostatic pressing (HIP) technology and its applications to metals and ceramics." *Journal of Materials Science* 39.21 (2004): 6399-6420.
- [12] Lu, S. L., et al. "Microstructure and mechanical properties of long Ti-6Al-4V rods additively manufactured by selective electron beam melting out of a deep powder bed and the effect of subsequent hot isostatic pressing." *Metallurgical and Materials Transactions A* 46.9 (2015): 3824-3834.
- [13] Al-Bermani, S. S., et al. "The origin of microstructural diversity, texture, and mechanical properties in electron beam melted Ti-6Al-4V." *Metallurgical and materials transactions A* 41.13 (2010): 3422-3434.
- [14] Zeng, L., and T. R. Bieler. "Effects of working, heat treatment, and aging on microstructural evolution and crystallographic texture of α , α' , α "and β phases in Ti-6Al-4V wire." *Materials Science and Engineering, A*, 392(1) (2005), 403-414.
- [15] Rietveld H. M. (1969). A profile refinement method for nuclear and magnetic structures. *Journal of applied Crystallography*, 2(2), 65-71.
- [16] Rietveld H. M. (1967). Line profiles of neutron powder-diffraction peaks for structure refinement. *Acta Crystallographica*, 22(1) (1967), 151-152.
- [17] Leuders, S., Thöne, M., Riemer, A., Niendorf, T., Tröster, T., Richard, H.A. and Maier, H.J., (2013). On the mechanical behavior of titanium alloy TiAl6V4 manufactured by selective laser melting: Fatigue resistance and crack growth performance. *International Journal of Fatigue*, 48, pp.300-307.
- [18] Spreadborough, J., and J. W. Christian. "The measurement of the lattice expansions and debye temperatures of titanium and silver by X-ray methods." *Proceedings of the Physical Society* 74.5 (1959): 609.
- [19] Yu, C. Y., et al. "Corrosion behavior of thermohydrogen processed Ti6Al4V." *Scripta materialia* 56.12 (2007): 1019-1022.

- [20] Wood, R. M. "The lattice constants of high purity alpha titanium." *Proceedings of the Physical Society*, 80(3) (1962), 783.
- [21] Assis, S. L., and I. Costa. "Electrochemical evaluation of Ti-13Nb-13Zr, Ti-6Al-4V and Ti-6Al-7Nb alloys for biomedical application by long-term immersion tests." *Materials and Corrosion*, 58(5) (2007), 329-333.
- [22] Kolman, D. G., and J. R. Scully. "Electrochemistry and Passivity of Ti-15 V-3 Cr-3 Al-3 Sn β -Titanium Alloy in Ambient Temperature Aqueous Chloride Solutions." *Journal of the Electrochemical Society* 141.10 (1994): 2633-2641.
- [23] Singh, Raghuvir, A. Kurella, and Narendra B. Dahotre. "Laser Surface Modification of Ti-6Al-4V: Wear and Corrosion Characterization in Simulated Biofluid." *Journal of biomaterials applications* 21.1 (2006): 49-73.
- [24] Cisse, O., et al. "Effect of surface treatment of NiTi alloy on its corrosion behavior in Hanks' solution." *Journal of biomedical materials research* 61.3 (2002): 339-345.

CHAPTER 7

RESEARCH CONCLUSIONS

This thesis presents the results of corrosion behavior study as affected by post-treatments on Ti-6Al-4V alloy via direct metal laser sintering (DMLS). Various post-treatments, including heat treatments in the $\alpha+\beta/\beta$ regions and hot isostatic pressing in the $\alpha+\beta$ region at different temperatures, have been studied.

The influencing factors on the corrosion behavior of DMLS Ti-6Al-4V parts have been studied through electrochemical methods. (Paper I)

- The DMLS Ti-6Al-4V parts with acicular microstructure have higher corrosion rate than the Grade 5 alloy with equiaxed microstructure under smooth finish, because of the unstable α' phase and surface defects produced during printing.
- Surface roughness has positive correlation on the calculated corrosion rate. Rough surface has higher corrosion rate than smooth surface, and this effect is more significant in the Grade 5 alloy with equiaxed microstructure.
- The existence of surface pores can impair the pitting corrosion resistance of the parts.

In order to obtain an optimum combination of ductility and fracture toughness, annealing treatment in the $\alpha+\beta$ region is a commonly recommended. The effects of post-annealing treatments on the tensile properties and corrosion behavior of DMLS Ti-6Al-4V are studied. (Paper II)

- Post-annealing treatments coarsened the acicular microstructure and reduced internal porosity in the as-printed parts. By closing the pores as crack nucleation sites, the ductility after annealing treatments have two-fold enhancement.
- The electrochemical measurements indicate that the as-printed parts with acicular microstructure possess a thicker and more stable oxide film than equiaxed Grade 5 Ti-6Al-4V alloy. The high temperature annealed parts have lower corrosion current density than as-printed parts, and passives up to 2.6 V (vs. Ag/AgCl).

Apart from annealing treatment, solution treatment and age and stress relieve treatment are commonly applied to titanium alloys to increase strength and reduce residual stress, respectively. The variations of corrosion behavior during these treatments have been studied. (Paper III)

- The as-printed Ti-6Al-4V via direct metal laser sintering has α' martensite phase with small amount of nano-scaled β precipitates dispersed in the α' matrix. Post-heat

treatments at elevated temperatures coarsened the lath microstructure and allowed further development of β phase.

- Based on electrochemical impedance spectra results, a single passive layer was observed in the as-printed and low temperature stress relieved sample due to limit solute element partitioning. Double passive layer could be developed in 650SR, 950STA and 1050STA with enhanced resistance of the titanium oxide passive layer. The reduced α phase percentage and α/β interface in 1050STA, 950STA and 650SR was likely to result in superior corrosion behavior.

Hot isostatic pressing (HIPing) is widely used in metal and ceramic processing to reduce internal porosity. Since the existing porosity can be the crack nucleation sites during tensile and fatigue testing, as well as reducing the pitting corrosion resistance of the as-printed parts, HIPing under various temperatures were studied. (Paper IV)

- HIPing in the $\alpha+\beta$ region can coarsen the α lath thickness and increasing β phase fraction. This effect increases with increased HIPing temperature. All of the HIPed samples show more passive anodic polarization behavior than the as-printed one, and the corrosion resistance is better under elevated HIPing temperature.

In sum, this thesis focused on the corrosion behavior change and surface passive film analysis of the DMLS Ti-6Al-4V parts after various post-treatments. Based on the experimental results, annealing treatment in the $\alpha+\beta$ region (close to β transus) is recommended to obtain a good corrosion resistance with enhanced ductility. Most of the post-treatments are aimed to improve mechanical properties, which have been widely studied, and this thesis fills the gaps of the corrosion behavior change via those treatments. By combining optimized mechanical properties and improved corrosion behavior, the additively manufactured Ti-6Al-4V alloy can meet the demands for aerospace and biomedical applications.

CHAPTER 8

RECOMMENDATIONS FOR FUTURE WORK

This thesis studied the corrosion behavior of direct metal laser sintered Ti-6Al-4V alloys as affected by various post-treatments. The electrolyte used in this study was the Ringers solution aimed to simulate the body fluid, since Ti-6Al-4V alloys are widely used as orthopedic implants. For these specific applications, the load bearing implants need to have a combination of high fatigue strength, good wear and corrosion resistance. Poor fatigue properties can lead to catastrophic failure, and wear of the implants will cause the release of metal debris into the surrounding tissue. Post-treatments can vary the microstructure and strength, and therefore change the fatigue and wear properties. In order to design a proper post-treatment procedure for DMLS Ti-6Al-4V alloy for orthopedic application, the variation of fatigue and wear properties need to be fully understood.

CHAPTER 9

PUBLICATIONS, POSTERS AND PRESENTATIONS

9.1 Publication

- [1] Yangzi Xu, Yuan Lu, Kristin Sundberg, Jianyu Liang, Richard D Sisson, Effect of Annealing Treatment on the Microstructure, Mechanical Properties and Corrosion Resistance of Direct Metal Laser Sintered Ti-6Al-4V. *Journal of Materials Engineering and Performance*. DOI: 10.1007/s11665-017-2710-y.

9.2 Conference Proceedings

- [1] Yangzi Xu, Yuan Lu, Richard D Sisson, Effect of Heat Treatment on the Microstructure, Mechanical Properties and Corrosion Behavior of Ti-6Al-4V via Direct metal Laser Sintering. ASM Heat Treat Society 28th Conference and Exposition October 20th – 22th, 2015 (Detroit, MI). Asm.
- [2] Yangzi Xu, Yuan Lu, Kristin L Sundberg, Richard D Sisson, The Effect of Annealing on the Microstructure, Mechanical Properties and Corrosion Behavior of Ti-6Al-4V via Direct Metal Laser Sintering, Materials Science & Technology 2015 (Columbus, OH).
- [3] Yangzi Xu, Yuan Lu, Yiming Rong, Richard D Sisson, Effect of Heat Treatment on the Microstructure and Corrosion Behavior of Ti-6Al-4V via Direct Metal Laser Sintering, Materials Science & Technology 2015 (Columbus, OH).
- [4] Yangzi Xu, Yuan Lu, Jianyu Liang, Richard D Sisson, Effect of Surface Morphology and Surface Finish on the Corrosion Resistance of Heat Treated Ti-6Al-4V via Direct Metal Laser Sintering, 23rd IFHTSE Congress. Asm, 2016 (Savannah, GA).

9.3 On-Topic Conference Posters and Presentations

- [1] Yangzi Xu, Yuan Lu, Kristin L Sundberg, Jianyu Liang, Richard D Sisson, The Effect of Post-Heat Treatments in Direct Metal Laser Sintered (DMLS) Ti-6Al-4V, GE Global Research – Student Research Summit August 14th, 2015 (Niskayuna, NY).
- [2] Yangzi Xu, Yuan Lu, Richard D Sisson, Effect of Heat Treatment on the Microstructure, Mechanical Properties and Corrosion Behavior of Ti-6Al-4V via Direct metal Laser Sintering. In ASM Heat Treat Society 28th Conference and Exposition October 20th – 22th, 2015. (Detroit, MI).
- [3] Yangzi Xu, Yuan Lu, Kristin L Sundberg, Richard D Sisson, The Effect of Annealing on the Microstructure, Mechanical Properties and Corrosion Behavior of Ti-6Al-4V via Direct Metal Laser Sintering, Materials Science & Technology 2015 (Columbus, OH).
- [4] Yangzi Xu, Yuan Lu, Yiming Rong, Richard D Sisson, Effect of Heat Treatment on the Microstructure and Corrosion Behavior of Ti-6Al-4V via Direct Metal Laser Sintering,

Materials Science & Technology 2015 (Columbus, OH).

- [5] Yangzi Xu, Yuan Lu, Jiangu Liang, Richard D Sisson, Effect of Surface Morphology and Surface Finish on the Corrosion Resistance of Heat Treated Ti-6Al-4V via Direct Metal Laser Sintering, 23rd IFHTSE Congress. Asm, 2016 (Savannah, GA).
- [6] Yangzi Xu, Richard D. Sisson, Jr., Processing – Microstructure – Property Relationships in Additively Manufactured Metallic Alloys, Forging Industry Technical Conference, 2016 (Columbus, OH).
- [7] Yangzi Xu, Yuan Lu, Jiangu Liang, Richard D. Sisson, Jr., Comparison of Annealing and Hot Isostatic Pressing on Microstructure, Mechanical Properties and Corrosion Behavior of Direct Metal Laser Sintered Ti-6Al-4V, Materials Science & Technology 2016 (Salt Lake City, UT).

9.4 Anticipated Publications

- [1] Factors Influencing the Corrosion Behavior of Ti-6Al-4V via Direct Metal Laser Sintering (Submitted to *Journal of Biomedical Materials Research Part A*)
- [2] Effect of Post-Heat Treatment Processing on the Microstructure and Corrosion Behavior of Direct Metal Laser Sintered Ti-6Al-4V. (Submitted to *Materials and Corrosion*)
- [3] The Effects of Hot Isostatic Pressing on the Microstructure, Mechanical Properties and Corrosion Behavior of Direct Metal Laser Sintered Ti-6Al-4V for Orthopedic Applications. (To be submitted to *Additive Manufacturing*).